ToF-SIMS characterisation of fragile materials used in microelectronic and microsystem devices : validation and enhancement of the chemical information

Riccardo Scarazzini

Communauté
UNIVERSITÉ Grenoble Alpes

THÈSE

Pour obtenir le grade de

DOCTEUR DE LA COMMUNAUTE UNIVERSITE GRENOBLE ALPES

Spécialité : **Matériaux, Mécanique, Génie civil, Electrochimie**

Arrêté ministériel : 7 août 2006

Présentée par

Riccardo SCARAZZINI

Thèse dirigée par **Vincent JOUSSEAUME**
et encadrée par **Marc VEILLEROT**

préparée au sein du **Service de caractérisation des matériaux & composantes du CEA-LETI à Grenoble**
dans **l'École Doctorale I-MEP2 de l'INP Grenoble**

ToF-SIMS characterisation of fragile materials used in microelectronic and microsystem devices: validation and enhancement of the chemical information

Thèse soutenue publiquement le **04-juillet-2016**,
devant le jury composé de :

Pr. Antonino LICCIARDELLO
Prof. à l'Université de Catane, Rapporteur
Pr. Laurent VENTURA
Prof. à l'Université de Tours et CEO SiLiMiXT, Rapporteur
M. Damien COSSEMENT
Chercheur Materia Nova Mons, Examinateur
Pr. André AYRAL
Institut Européen des Membranes, Président du jury
Dr. Vincent JOUSSEAUME
Chercheur HDR CEA, Directeur de thèse
Dr. Marc VEILLEROT
Chercheur CEA, encadrant de thèse

A nonna Ortensia e zio Rino

DECLARATION

I hereby declare that except where specific reference is made to the work of others, the contents of this dissertation are original and have not been submitted in whole or in part for consideration for any other degree or qualification in this, or any other university. This dissertation is my own work and contains nothing which is the outcome of work done in collaboration with others, except as specified in the text and Acknowledgements.

Riccardo SCARAZZINI

July - 2016

ACKNOWLEDGEMENTS

First I would like to acknowledge Antonino Licciardello and Laurent Ventura, who have kindly accepted to evaluate this thesis work and secondly Damien Cossement and André Ayral, who have accepted to be members of the jury.

I also acknowledge the financial support of the CEA, which allowed me to pursue this Ph.D. research. My gratitude goes to Vincent Jousseaume for its help and guidance over the past three years, without him and all the constructive discussions none of this would have been possible, I would also thank Jean-Claude Royer, Narciso Gambacorti, François Bertin and Jean-Paul Barnes for the precious advices and the support provided. I extend also my gratitude to the whole CEA/SCMC group. A special mention goes to Marc Veillerot, who "adopted" me in his group and was a constant friend over these years sharing experiences time and stress (and good wine). I am also very grateful to all the collaborators and staff of the CEA and STMicroelectronics (Lucile Broussous and Matthieu Lépinay). A thanks to all the CEA/SDEP group especially to Laetitia Bonnet et Julien El Babahy for their precious help. My gratitude goes to all the people of the lab and towards the group of "colleagues" or should I say friends, that I had the opportunity to meet during this experience: Robert, Tanguy, Victoria, Tristan, Remi, Tariq, Mélanie, Matthieu, Marin, Nico, Florentin and many many others, my great thanks.

A special thanks to my extremely super friends Fil, Pank and Giulietto for everything they represent and have meant during these years and I hope we can meet each other as soon as possible. I would also thank Javier, Teresa, Fouad and Zak for the moment we spent together and for the great friendship though we are far from each other.

And the last but not the least, I would like to thank Emma-Sophie, her presence, love and patience helped me to arrive till the end of this work and I hope to be able one day to do the same for her.

Finally, I want to thank my Dad and my Mum for all their support and comprehension and their patience in watching me growing.

You are all the best people I could have ever met.

Un grazie infinito a tutti voi, vi porto sempre nel cuore

Table of Contents

List of Figures

List of Abbreviations and Acronyms

3D	three dimensions
AFM	atomic force microscopy
BDII	black diamond II
BEOL	beck end of line
COCOS	Corona Oxide Characterisation of Semiconductor
CVD	chemical vapour deposition
DC	direct current
EI	electron impact
EP	ellipsoporosimetry
FEOL	front end of line
FT-IR	Fourier transformed infrared spectroscopy
GCIB	gas cluster ion beam
ICs	integrated circuits
i-CVD	initiated chemical vapour deposition
IR	infrared
LMIG	liquid metal ion gun
Low-*k*	low dielectric constant materials
MD	molecular dynamics
MEMS	- micro electro mechanical systems
MVA	- multivariate analysis
M_w	molecular weight
NEMS	nano electro mechanical systems
NPS	nonporous silica
OSG	organosilicate glass
PCA	principal component analysis
PECVD	plasma enhanced chemical vapour deposition
PS	photoluminescence spectroscopy
p-SI	porous silicon
QCM	quartz crystal microbalance
RC	signal delay

SE	secondary electrons
SEC	size-exclusion chromatography
SEM	scanning electron microscopy
SIMS	secondary ion mass spectrometry
SRIM	stopping and range of ions in matter
TEM	transmission electron microscopy
TRIM	transport of ions in matter
ToF	time of flight
UHV	ultra high vacuum
UV	ultra-violets
VPP	vapour phase polymerisation
XPS	X-ray photoelectron spectroscopy

List of Appendices

INTRODUCTION

It was J.J. Thomson who, while speaking during a conference, put forward his prophetic statement about the features of mass spectrometry:

> *"I feel sure that there are many problems in chemistry which could be solved with far greater ease by this than any other method. The method is surprisingly sensitive-more so even than that of Spectrum Analysis, requires an infinitesimal amount of material and does not require this to be specially purified: […] the method may disclose the existence of intermediate forms which have only transient existence, as well as that of the final product, and may thus enable us to get a clearer insight into the processes of chemical combination."*
>
> *[J.J. Thomson, Rays of positive electricity and their application to chemical analysis. Longmans London, 1913]*

Indeed, many different techniques based on the detection of charged particles have been developed till now. Among them, Time of Flight Secondary Ion Mass Spectrometry ToF-SIMS is an advanced technique for the chemical characterisation of surfaces of a large variety of inorganic and organic materials and structures such as the ones used in micro and nanotechnologies, biosciences or astrophysics. The range of materials able to be characterised is still getting larger in parallel with the on-going development of new primary ion sources. Nowadays, the micro and nanotechnology domain integrates a wide range of structures characterised by low densities and soft materials. In particular, these matter states are achieved by the particular given design such as three-dimensional meso-structuration or by the nature of the chemical bounds such as for polymers of organic cross-linked materials. The behaviour of these innovative materials under specific ion bombardment conditions often differs from the one of classical dense material especially in terms of ion/matter interaction and secondary ion generation. The particular interaction

that could take place is characterised in this work as “fragile” behaviour. The intrinsic (chemical bonds) and extrinsic (3D structure) fragility characterise the three material categories, at different degree of integration in the nanotechnology industry, chosen for this study.

The objective is to verify and validate the ToF-SIMS as a reliable technique for answering the chemical characterisation needs met by these materials and assess the consistency of their chemical information through the interpretation of ion/matter interactions.

The first category of fragile materials analysed (1) is porous silicon (p-Si), a form of silicon with generated porosity in its microstructure inducing a large surface/volume ratio around $\sim 500\ m^2/cm^3$. The industrial interest for this material is potentially wide due to the excellent control of porous properties (shape and rate) and to the possibility to vary surface properties in order to improve for example cell adhesion or optical properties. Most promising applications of porous silicon are in the field of bio-inert or bioactive materials, energy storage, optics and insulators. In this kind of material the definition of “fragility” involves principally the complex 3D structure and its interaction with energetic primary ions; p-Si chemical or morphological alterations can occur during analysis as clearly observed for electron microscopy or photoluminescence spectroscopy [1] and characterisation techniques using high energetic ions [2, 3]. The presence of voids can be an obstacle to the heat transfer induced by ion irradiation that, coupled to the nanometric dimensions, can induce a melting at lower temperatures compared to bulk dense silicon. The chemical composition of the sample is also a key process regarding heat transfer as shown for nanoparticles systems exposed to energetic ion beams [4].

In this work, in order to evidence and understand these phenomena, a methodical analysis consisting in the observation of data variations is carried out on mesoporous silicon samples sputtered by energetic primary ions.

The second category of materials is composed of polymers (chapter 3). In this case, the “fragility” is defined by the nature of chemical bounds and their behaviour under primary energetic ions. In general, polymers used in microelectronics need characterisation techniques sensitive to extremely thin films. Ideally, these techniques have to be able to give fine chemical information about composition while keeping an ideal depth resolution in order to correctly determine interfaces in the case of stack

samples [5]. In particular, the analysis of the chemical composition is essential to the comprehension of many phenomena such as the control of deposition processes as well as material contamination, degradation or fine chemical variations. The introduction of polyatomic primary ion sources is characterised by an ion/matter interaction more localised on the surface and with a reduced fragmented secondary ion information. The ToF-SIMS has become a well-adapted technique able to answer the characterisation needs for integrated polymers in micro and nanotechnologies.

In the last ten years, a new deposition technique called initiated chemical vapour deposition (i-CVD) [6] has shown promising results in terms of range of deposited materials and solvent free polymerisatio. At present, one of the challenges of this deposition technique is to obtain a good control of the film molecular weights also for nanometer thick films. At these dimensions, intrinsic properties such as degree of polymerisation and copolymer quantification in the case of mixture become fundamental. In the wide panorama of characterisation techniques, time of flight secondary ion mass spectrometry is one of the most promising. This statement finds its explanation thanks to the high mass resolution coupled with an outstanding mass detection range of this technique.

In this work, the ability of ToF-SIMS to successfully profile polymers stacks by using large gas cluster ion beams is stated and explored, taking into account material parameters such as molecular weight (M_w). The high mass secondary ion information produced while analysing samples with different average M_w is thought to be dependent from the degree of polymerisation as observed in previous works [7, 8] but not achieved for high polymerisation degrees. To verify this theory low damaging analysis conditions will be used coupling the detected secondary ion information with statistical tools for the interpretation of the complex multivariate data system.

The third category of fragile materials (chapter 4) concerns low dielectric constant insulators (low-*k*). These materials are successfully used as insulators between interconnection lines of integrated circuits. In this case the fragility is induced by their cross-linked network and porous nature that impacts mechanical properties and at the same time makes it is prone to chemical modifications while integrated in circuits.

In this work, the variation of dielectric constant due to integration processes is chemically interpreted by using the advantageous characteristics of ToF-SIMS technique such as high mass resolution and the possibility to analyse thin films with improved depth

resolution using a low energy sputtering gun or large cluster ion gun. However, low-*k* dielectric materials introduce new issues for SIMS depth profiling. The unique insulation properties make SIMS analysis very challenging since the analysis itself can degrade the material such as for nanoparticles, porous materials or polymeric samples. The impact of sputtering sources on this kind of cross-linked hybrid porous materials is explored in order to determine the appropriate analysis conditions capable to couple a fine chemical information and its appropriate localisation in depth.

Once achieved a solid knowledge on how to analyse low-*k* porous samples, the study is extended to samples exposed to industrial integrating processes for the production of insulating on-chip layers to achieve information about the chemical modifications induced by implementation treatments and couple them to the dielectric constant variations.

1 INTRODUCTION TO TOF-SIMS AND STATE OF ART OF FRAGILE MATERIAL CHARACTERISATION

This first chapter describes the Secondary Ion Mass Spectrometry (SIMS), concept and applications, with a particular attention to Time of Flight ToF-SIMS technique. The continuous ameliorations of this technique during the years are described and correlated to the enlargement of applications starting from classical solid inorganic materials reaching the state of art of fragile materials characterised by 3D low density nanometric structures, organic and hybrid materials with integrated porosities.

1.1 INTRODUCTION TO SECONDARY ION MASS SPECTROMETRY (SIMS) AND A BRIEF HISTORY OF TIME OF FLIGHT TOF-SIMS DEVELOPMENTS

SIMS as material characterisation technique is based on the information brought by the atomic or molecular secondary ions ejected from any surface under a primary ion bombardment. With ToF-SIMS in particular, depth profiling with good in-depth resolution coupled with the possibility to detect dopant traces and impurities can be achieved. In addition, it has a high potential to obtain information about the molecular, elemental, and isotopic constituents on surfaces.

John Thomson in 1910 was the first to observe positive secondary ions generated while bombarding a metal surface with primary ions. Fifty years later, the significant advances made in optical ion design resulted in the development of three basic types of SIMS instruments [9]: ion microprobe, ion microscope (high lateral resolution) and mass analyser with moderate lateral resolution. Originally, SIMS instruments, because of their limited sensitivity, had to operate at high primary ion current with critical erosion rates in the order of hundreds of monolayers per second. The term “dynamic” SIMS” was coined, its working mode was applied only to the characterisation of bulk solids, as the surface analysis was impossible in such a sputtering regime.

Specific SIMS technology oriented to the monitoring of secondary ions emission from solid surfaces was first developed in Munster at the end of the 1960s by Alfred Benninghoven and his research group [10]. The first interest was focussed on the sputtering process and in particular on the energy distribution of the emitted ions. A single ion counting technique for mass spectrometry was then developed and they gave to it the name of "static SIMS" with primary ion fluence much lower than the reciprocal of the damage cross section ($F << 1/\sigma$). Since for many materials σ is in the range of $10^{-14} - 10^{-13}\ cm^2$, the static SIMS limit can be reasonably located below $10^{12}\ ions/cm^2$. The application of this technology for the analysis of surface was revealed as well its potentiality in the analysis of organic systems. Years of improvement made SIMS a powerful technique for chemical analysis. Now, SIMS is able to give an extremely sensitive elemental as well as molecular information.

Remarkable progress in instrumentation opened to SIMS new fields of application. The simultaneous development of magnetic and quadrupole based spectrometers lead to the investigation of a large variety of surface reactions such as proton, oxygen and small organic molecules on various metal surfaces. Later, it was discovered that the primary ion bombardment was able to produce characteristic high mass fragments not detectable by quadrupole instruments. This precious low fragmented high mass chemical information became detectable after the development of a high-performance Time-of-Flight spectrometer.

The Time-of-Flight mass analyser separates the ions in a field-free drift path according to their velocity. Since all ions possess the same kinetic energy, their velocity and, therefore, time of flight varies according to their mass. It requires pulsed secondary ion generation using either a pulsed primary ion gun or a pulsed secondary ion extraction. It is the only type of analyser able to detect all generated secondary ions simultaneously and is now a standard analyser for static SIMS instruments.

The higher mass range detection accessible after the introduction of the Time of Flight (ToF) analyser opened the way for oligomer and large molecule (polymers and bio-samples) analysis. In addition, the introduction of a pulsed low energy electron injector for charge compensation opened the access to insulating materials. High mass polymers biomolecules and peptides were now able to be characterised obtaining mass detection ranges up to 10000 amu (atomic mass unit). The introduction of a static reflectron increased mass resolution and reduced the instrument size. Only after the integration of a

focused liquid metal ion sources and secondary electrons (SE) detectors, a commercial version of the ToF-SIMS was developed in 1989.

The rapid evolution of this technology was first linked to the utilisation of innovating primary ion sources such as caesium (Cs^+ [11]) and oxygen (O_2^+ [12]) used for sputtering. On the other hand, big advantages in terms of chemical information detected and lateral resolution (around 80 nm) were achieved by the use of polyatomic primary ion sources such as metal ion guns (at first gallium follower by bismuth [13] and gold [14]) as analysis guns, lately followed by polyatomic ion sources such as fullerene (C_{60}^+ [15]) and argon clusters (Ar_n^+ [16]) and maybe water in future [17] for sputtering.

Time-of-flight secondary ion mass spectrometry is at present able to probe 1-2 nanometres of a sample surface of a large variety of inorganic et organic materials [18]. This technique also offers an advanced mass resolution and sensitivity making it an excellent candidate for the chemical characterisation of materials applied in micro and nanotechnologies.

1.1.1 ToF-SIMS working principle and instrumental configuration

1.1.1.1 Working principle

The working principles of ToF-SIMS are briefly discussed in this section, a complete overview of this technique can be found in the works of Vickerman *et al.* [19, 20]. The description will be adapted to the kind of ToF-SIMS used in this work. As a consequence, magnetic and quadrupole SIMS principles are not going to be described though the ion-solid interaction processes are the same (see Appendix1: SIMS theory).

A primary ion is accelerated toward the sample surface and the impact generates a large number of ejected particles. These particles (neutral atoms, molecules, electrons and ions) are emitted into the vacuum chamber. Generated ions are then accelerated by an applied potential between the sample surface and the analyser. Then, time of flight analyser collects the ions and separates them depending on their flight time in the spectrometer. The collected information is a representation of the surface chemistry composing the sample surface. Good mass resolutions are attainable with modern liquid metal ion guns (LMIG), while secondary ion yields have been enhanced by the introduction of polyatomic ion sources [21, 22]. In many cases, the interest to know the chemical composition is not limited to the surface. Sputtering is then needed to renew the

sample surface for a subsequent characterisation. To achieve this need, a second ion gun is added to sputter the surface. This setting is known as “dual beam” ToF-SIMS and the working principle is described.

1.1.1.2 Time of Flight SIMS and Dual beam mode

Free flight time can be directly measured since secondary ions come from a single short primary ion pulse. The resulting mass spectrum is then an extrapolation of a secondary intensity ion diagram plotted as a function of time. To switch from time function plot to the one with masses (m/z) in abscissa, equation Eq.1.1 is used. In this equation the flight chamber length (L), the acceleration potential (U) and the electron charge (e^-) are known parameters, while E_0 corresponds to the initial energy of the ion before acceleration.

$$t_{flight} = L\sqrt{\frac{m/z}{2e^-(E_0 + U)}} \qquad Eq.1.1$$

In Figure 1.1a-b, the principle describing the generation of secondary ions by primary ions bombardment and the resulting spectra is shown.

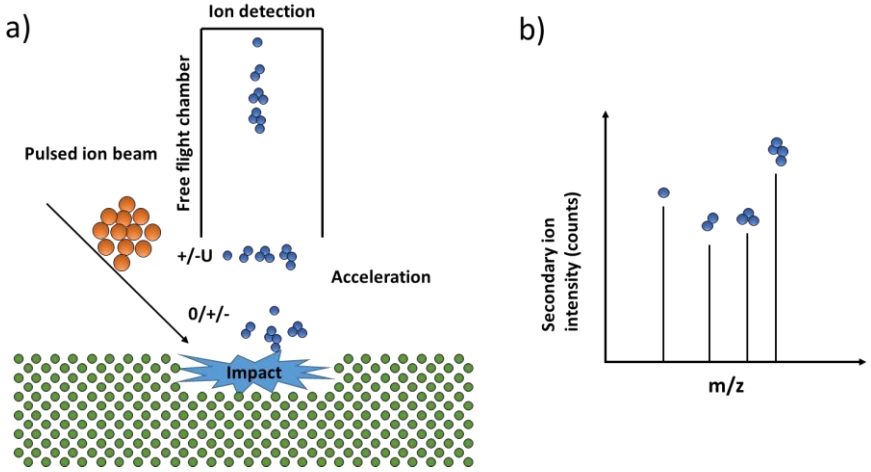

Figure 1.1: a) Schematics of a ToF-SIMS complete scan: primary ions are bunched and accelerated toward the target where the collision induces the emission of neutrals atoms, electrons, ions, light… At this point, the detection starts accelerating secondary ions with a potential $^{+/-}U$. Accelerated ions enter in the flight chamber where the separation takes place before the ion counting. b) Mass spectrum generated by the single pulsed primary ion. The different free flight durations (t_{flight}) are transformed in mass on charge (m/z) scale through Eq.1.1.

The initial energy distribution ΔE_0 of generated ions has a range of few eV. This energy scattering has an impact on the flight time distribution Δt_{flight}, which is also

influenced by the width of the primary ion pulse and by the precision of the secondary ion detector. It is then possible to calculate the mass resolution $\left(\frac{m}{\Delta m}\right)$ of the spectrum Eq.1.2, normally in the order of a few thousands.

$$\frac{m}{\Delta m} = \frac{t_{flight}}{2\Delta t_{flight}} \qquad Eq.1.2$$

Coupled with the primary analysis gun, dual beam mode uses a second primary ion gun that bombards surface samples (sputtering). While quite energetic ions ($10 - 30\ keV$) are used for the analysis beam (typically used with low currents, so giving negligible erosion rate), in the case of the sputtering gun lower accelerations energies are used (from a few hundred eV to a few keV)

This kind of configuration has several advantages. Among others:

- high secondary ion yield thanks to energetic analysis beams,
- reduced damage in depth when low sputtering energies are used,
- better depth-resolved profiles,

these advantages arise from the possibility of decoupling the erosion from analysis, at variance of other SIMS technologies where analysis and sputtering are accomplished with the same beam [20].

The cycle time working principle of "dual beam" mode is given in Figure 1.2. While the pulsed analysis beam is accelerated through the target, extraction and time counting are activated. Extraction potential last in a few microseconds ($10\ \mu s$) and just after sputtering is activated while extracted ions are analysed in the time of flight chamber. This particular working mode is called "interlaced mode" and it is used for materials capable of driving accumulated charges far from the impact zone (electrically conductive materials). On the other hand, principally for insulating layers, charge compensation is needed. It consists in a low energy electron flooding between sputtering and pulsed analysis with the intention to establish a neutral surface charge after sputter beam is applied. This mode opens the possibility to longer sputter cycles and it is called "non-interlaced mode".

The analysis chamber consists of a UHV chamber allowing the introduction of the sample holder by a pre-stage chamber called load-lock. Atmosphere control (vacuum level, oxygen flooding), temperature control (cooling or heating) and sample charge control (electron flooding) can be modified by the user. Specifically to IONTOF instruments, all the primary ion beams are 45° tilted from the sample normal (Figure 1.2).

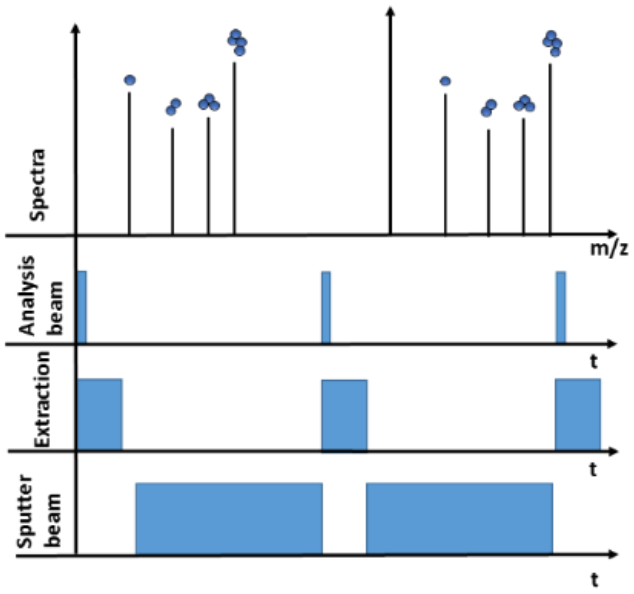

Figure 1.2 "Dual beam" data acquisition scheme.

This configuration is in many cases a good compromise regarding sputtering [23] and analysis properties. Moreover, it is a very practical solution to accommodate all the ion sources and the ToF analyser chamber placed in the direction orthogonal to the sample.

The dual beam setting gives to ToF-SIMS an advantaging versatility:

- Static SIMS: for extreme surface analysis. In this acquisition mode, only the analysis gun is used. The interest is to obtain a high mass resolved spectrum. To achieve this objective, normally, very short pulses at relatively high current densities are preferred. In the last years, new concepts of analysis guns are used, their particularity is to produce primary ion clusters (Bi_{3-7}^{+}) with the purpose of an increased ion yield and a more superficial interaction with target corresponding to a reduced in-depth damaged zone as simulations show [24].
- Depth profiling for bulk analysis: in this case the sputter and analysis beams are turned on alternatively, giving in result a series of spectra acquired at different depth points. Mass peaks are selected and their intensity are plotted as a function of sputter time forming the in-depth profile. In this mode, the characteristics of static mode are maintained and in some cases even enhanced, in particular, when the used sputtering source plays an active role in secondary ion generation such as caesium or oxygen source.
- Imaging mode: the surface sample is rastered by the primary ions and spectra are collected for each pixel. The intensity maps can be reconstructed for each

peak in the spectrum. These maps present a "chemical image" of the sample surface.

- Tomographic mode: coupling imaging mode with depth profiling, 3D reconstructions can be obtained.

ToF-SIMS is a very powerful technique for chemical characterisation. For this purpose, fundamentals of secondary ion generation have to be explored. The secondary ions generated by primary ion impact on a surface is mainly based on two different interactions: sputtering and ionisation. These two phenomena are briefly described in the next session.

1.1.2 SPUTTERING MECHANISMS

Sputtering mechanisms are different between inorganic and organic materials due to the atomic densities and chemical bonds composing them. As a consequence, these arguments are described separately.

1.1.2.1 INORGANIC MATERIALS

When an energetic primary ion impacts an inorganic target, a part of its energy is transferred to the surface region causing an ejection of the collided particles. Moreover, mechanisms are different whether the source is a monoatomic or a cluster one.

MONOATOMIC SOURCES

SIMS instruments can use primary ions like Ga^+, Ar^+, Cs^+, Xe^+, Au^+ etc.. with varying acceleration energies, around 0.5-30 keV. The collision with the target activates sputtering events than can be described by the linear cascade theory of Sigmund [25-27] (Eq.1.3). The term 'cascade' refers to multiple quasi-elastic collisions in the target sample induced by the bombarding ions (Figure 1.3). In a simple collision cascade, if the energy exchanged between the ions and target atoms exceeds the surface binding energy of the material, the collided atoms can be ejected from the surface, i.e. sputtered. The number of sputtered ions per incident ions $Y_{(E)}$ is defined as "sputtering yield" and is function of the target binding energy (normally sublimation energy is used E_s), the nuclear energy loss function at the surface $S_n(E)$ and a dimensionless coefficient $\alpha(M_t/M_i)$ function of the involved atomic masses (M) (target t and primary ion i).

$$Y_{(E_0)} = \frac{0.04}{E_s}\alpha(M_t/M_i)S_n(E) \qquad Eq.1.3$$

$S_n(E)$ is the same for all ion-target combinations and involves the nuclear charges.

It can be calculated using the total energy deposited near the surface, the number of low-energy recoil atoms in the target, the fraction of these recoil atoms that come to the surface, and the fraction that have sufficient energy to overcome surface binding forces. Factors important to be considered are also the angle of incidence of primary ions and the chemical nature of primary ions and target. As far as only the atoms nearest to the surface can escape the bulk, sputtering in the linear cascade regime results in the ultrahigh surface sensitivity. As the sputtering phenomena are not completely understood, models have been developed by fitting experimental data for many ion-target combinations (Matsunami *et al.* [28])

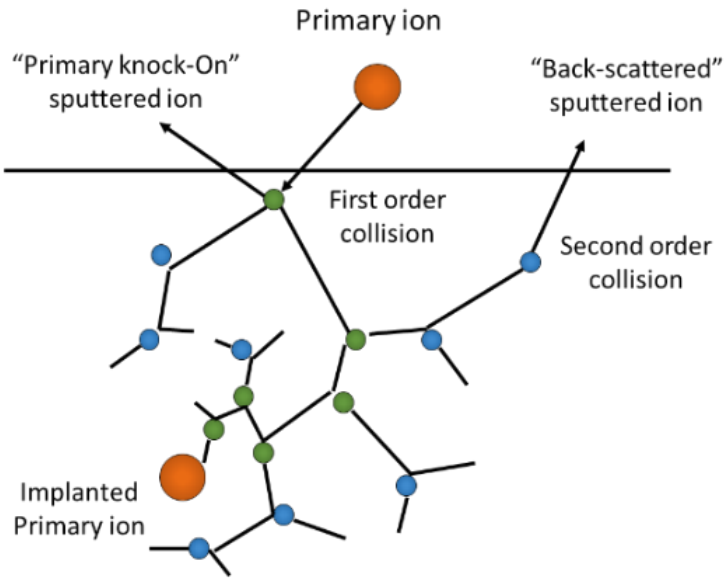

Figure 1.3: Schematic diagram of a linear collision cascade. The path of collided ions is indicated by black lines.

CLUSTER SOURCES

In the last few decades, a significant move towards new cluster ions sources took place. Sources like Bi_n^+, Au_n^+, SF_5^+, C_{60n}^+ and Ar_n^+ as primary projectiles in SIMS have been developed, characterized by massive enhancements in the sputter yield surprisingly higher than the ones expected from Sigmund's theory.

This sputtering phenomenon was defined as a "non-linear" collision cascade, because, in this case, simultaneous parallel collisions take place with a behaviour similar to the thermal excitation of a gas [29, 30].

In other words, for a cluster source of $(X_n)_E$ ions where n is the number of atoms impacting a target with a known energy (E), the resulting sputter yield will be higher than the singular sputter of X species at E/n energy multiplied by n. This phenomenon is explained by the higher energy densities deposited on near surface region joined with the accumulation of collision cascades generated by individual primary ions composing the cluster. The obtained sputter yield can reach values two orders of magnitude higher compared to monoatomic linear cascade values [15, 31-33]. This phenomenon is true and verified for reduced size clusters composed by decades of atoms. If the cluster size starts to reach hundreds of atoms, the inorganic sputtering rate rapidly decreases as shown in the studies of Seah and pointed out by his universal sputtering equation [34]. In this case the measured energy per atom is the fundamental parameter to determine sputtering yield of the material. This aspect will be explained in detail in the next session as high sputtering yields are obtained while bombarding organic materials with large clusters sources.

As far as cluster ion sputter mechanisms are not precisely understood, it is accepted that monoatomic primary ions implant deeper in the target causing a significant sub-surface damage, but only a small fraction of material is sputtered. Instead, cluster primary ions localise their deposition of energy on the extreme surface of the target creating a large impact crater that sputters a significant fraction of the material involved in the impacted volume. The most influencing parameters are the impact energy of clusters as well as the target/ion mass ratio and the bounding energy of atoms composing the target. Other important factors are the material density, its temperature, surface roughness and crystallinity [35-37].

1.1.2.2 Organic materials

While the bombardment of solid inorganic material is relatively known, many questions are still not answered for the organic sputtering principles. In this case, the involved mechanisms are hardly explicable by classical theories. As a consequence, many models have been developed involving molecular dynamics (MD) approach (Garrison *et al.* [38] and Delcorte *et al.* [24, 39]) as shown in Figure 1.4.

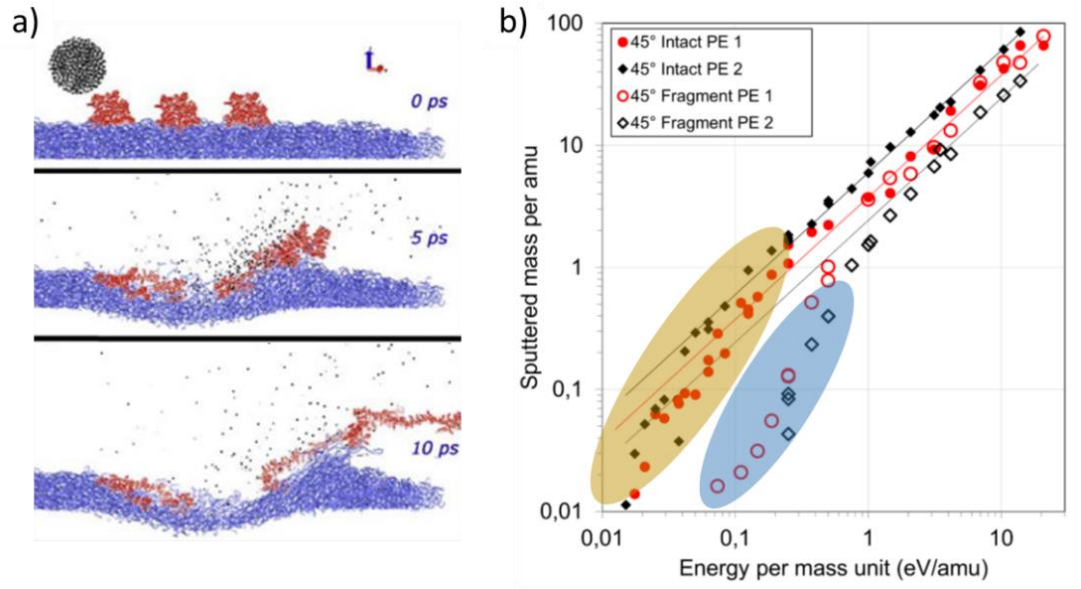

Figure 1.4: a) Time evolution of the molecular dynamics simulation during the impact of 10 keV Ar_{1000} cluster (10 eV/amu) on polyethylene sample: molecules and fragments are ejected thanks to the impacting cluster tilt. b) Sputtered mass of intact polyethylene molecules or fragments at different polymerisation degree vs. energy per atom [40].

Molecular dynamics and experimental data have shown that the secondary ion emission is composed of low and high mass molecules [40] (Figure 1.4-a). As shown in Figure 1.4-b for polyethylene samples (PE), the ratio of emission between entire molecules and fragments is different for low energy per atom ratios (eV/amu) where the emission of not fragmented species is favoured. For higher energy per atom ratios (>0.1 eV/amu) the emission of fragments become more intense indicating that not only entire molecules are ejected from the sample surface but a fragmentation of some of them takes place. This phenomenon was originally theorised by Benninghoven *et al.* [20] in description of organic molecules sputtered on a metal surface but it can be applied to thicker organic systems too [41, 42]. This model (Figure 1.5) describes the energy distribution of an energetic ion bombarding a target and its relation with the ejection of intact and fragmented molecules.

The energy profile of a monatomic or small cluster ion has a maximum and quickly decrease. In contrast, polyatomic sources produce an energy profile lower in maximum decaying less rapidly with a larger distribution of the impacting energy.

In the region close to the point of impact (red region), “impact region”, high energy events lead to the emission of atomic species and small organic fragments prevail. Usually, elementary information about the chemical structure of the components of the

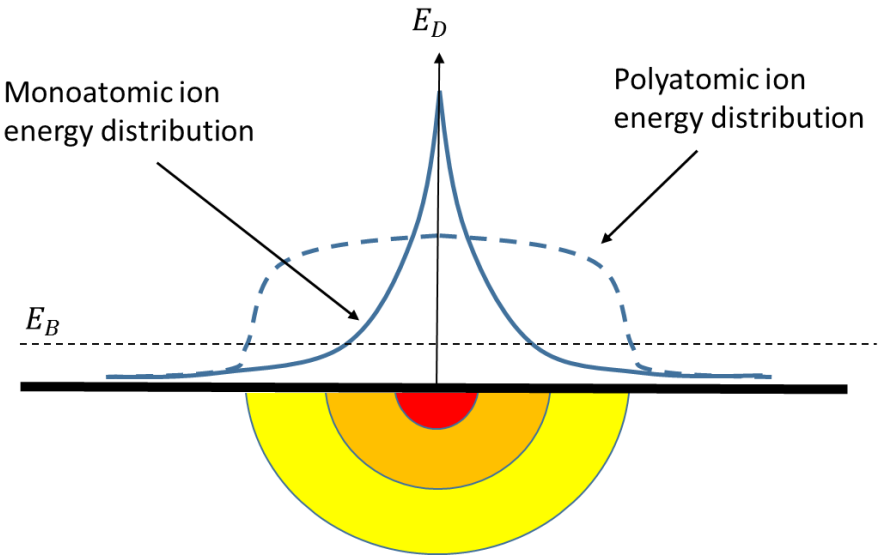

Figure 1.5: Schematic plot of the energy distribution in the surface during primary ion bombardment. The energy distribution plot differs if the primary ion source is a monoatomic one (continuous line) or polyatomic (discontinued line). E_B is the minimum energy needed for an intact molecule to be ejected. Scheme adapted from [43]

organic material such as polymers or third part contaminations is provided. Surrounding that area, a less damaging zone (orange zone), "fingerprint region" appears. It is a region with a decreased energy density where structural rearrangements may take place, such as characteristic monomer fragments. Formed by fragments generated after bonding events between two or more repeating units. This region may potentially contain information about the macromolecular structure (co-polymers distribution). There is also evidence that branching and/or cross-linking of polymers can be followed by changes in polymer fragment intensities [44]. Coupling this "intermediate" chemical information with statistical methods (such as multivariate analysis) opens the possibility to a more quantitative approach [45].

Farther away from the impact point, in the "oligomer mass region" (yellow zone), ejection of pattern-like species prevails as the energy available for rearrangements is low. Ejected species rise to larger but structurally most informative fragments [46, 47]. The "oligomer mass region" is usually favoured by metal cationization. To generate spectra comprising the oligomer distribution information the sample preparation is crucial. The metal cationisation is obtained depositing films on metal substrates such as aluminium or silver. The best results have been obtained when the polymer is deposited by evaporation or spin-casting to give a very thin layer on a specially prepared silver substrate [48-50]. During ion bombardment, the sputtered metal ions of the substrate are recombined with

organic chains ionising the entire molecule. In principle, this region permits an estimation of the average molecular weight distribution.

The emission of high mass fragments involves collective atoms movements on the surface near the impact region [41, 51] and in the extreme case, entire molecules are emitted. The interest of low energy monoatomic sources and polyatomic clusters is to produce a high mass molecular information as intact as possible without generating induced damage. Ion cluster sources such as $C_{60\,n}^{+}$ or Ar_n^+ enable the sputter removal of target material layer-by-layer with a reduced induced damage, therefore they are a real good solution for the characterisation of organic materials such as polymers [52, 53]. Before the introduction of polyatomic cluster sources, SF_5^+ ion source ability to depth profile organic materials was explored. The use of SF_5^+ was successful but a strong dependence between the quality of the depth profile and the sample cooling during analysis was observed. Figure 1.6 shows the depth profile of a poly(methyl methacrylate) pmMa sample at temperatures under glass transition (-75 $°C$), around the glass transition temperature (25 $°C$) and above (125 $°C$). The most successful depth profile was obtained at -75 °C for pmMa, which exhibited increased secondary ion stability, sharper interface widths and higher average signal intensities throughout the depth profiles [54].

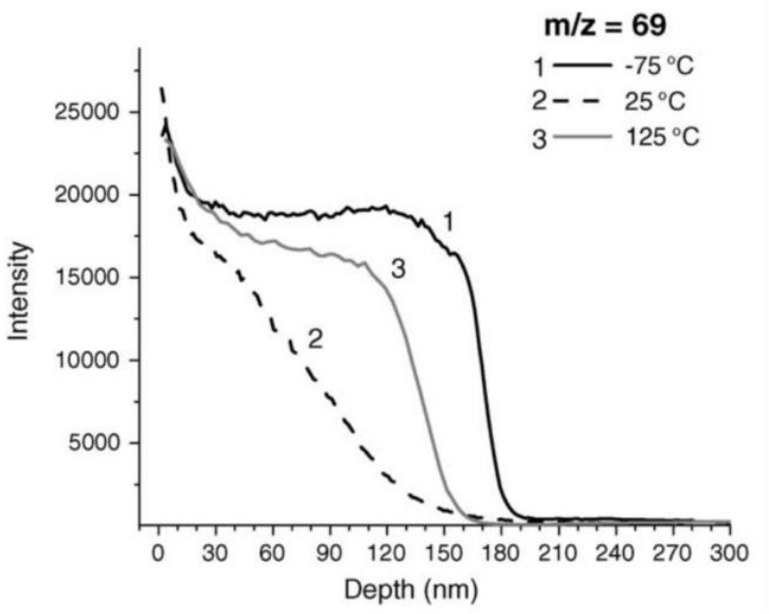

Figure 1.6: Positive secondary ion intensities of m/z = 69 ($C_4H_5O^+$, a fragment characteristic of pmMa) plotted as a function of depth for a pmMa film (160 nm) on Si substrate measured at: (1) -75 °C, (2) 25 °C and (3) 125 °C. All depth profiles were acquired using dual beam depth profiling (Ar^+ analysis source and SF_5^+ sputter source) [54].

CLUSTER SOURCES

The premise behind the success of cluster SIMS is that, compared to atomic beams, polyatomic beams tend to cause surface-localized damage with rapid sputter removal rates, resulting in a system at equilibrium, where the damage created is rapidly removed before it can accumulate. Though this may be partly true, there are much more complex chemistries occurring under polyatomic bombardment of organic and polymeric materials. All the polymers do not have the same behaviour under monoatomic or cluster bombardment. Typically polymers, when irradiated, can cross-link or degrade through a random chain scission process as reviewed by Mahoney [55]. Both types of degradation are complex systems known to involve free radical intermediates. The first "molecular depth profile" of a polymeric sample was demonstrated by Gillen and Roberson (1998) using an SF_5^+ cluster source [55]. The results from this work are shown in Figure 1.7, which compares depth profiles of a pmMa sample casted onto a silicon substrate. Here, the signal intensity of m/z=69 amu, a fragment characteristic of pmMa, was plotted as a function of increasing sputter time with both Ar^+ (left image) and SF_5^+ (right image). While there was rapid signal degradation when using Ar^+, the signal remained relatively constant with increasing sputter time when using SF_5^+ clusters. The substrate was reached after only 200 sec of sputtering with the SF_5^+ source, while the polymer/Si interface could only be reached after prolonged sputtering of the film at higher primary ion currents when using the Ar^+ source. The success of the polymeric depth profile was attributed to both surface-localized damage and increased sputter rates [55].

In general, it is assumed that polymers with high concentrations of quaternary carbon (carbon with four carbon neighbours) atoms along the chain (e.g. $CH_2 - CR_3$) undergo scission such as methacrylates, while those with a structure such as $-CH_2 - CH_2 -$ or $-CH_2 - CHR -$ (secondary or tertiary carbon) tend to cross-link such as polyethylene. It also appears that the most radiation-resistant (cross-linking) polymers contain aromatic substituents. This effect is said to be related to the "protection" (deactivation) produced by aromatic compounds.

The continuous amelioration of primary sources is already proposing new cluster sputtering compounds, such as cluster ion oxygen sources $(O_2)_n^+$ [56] and water clusters $(H_2O)_n^+$ [57].

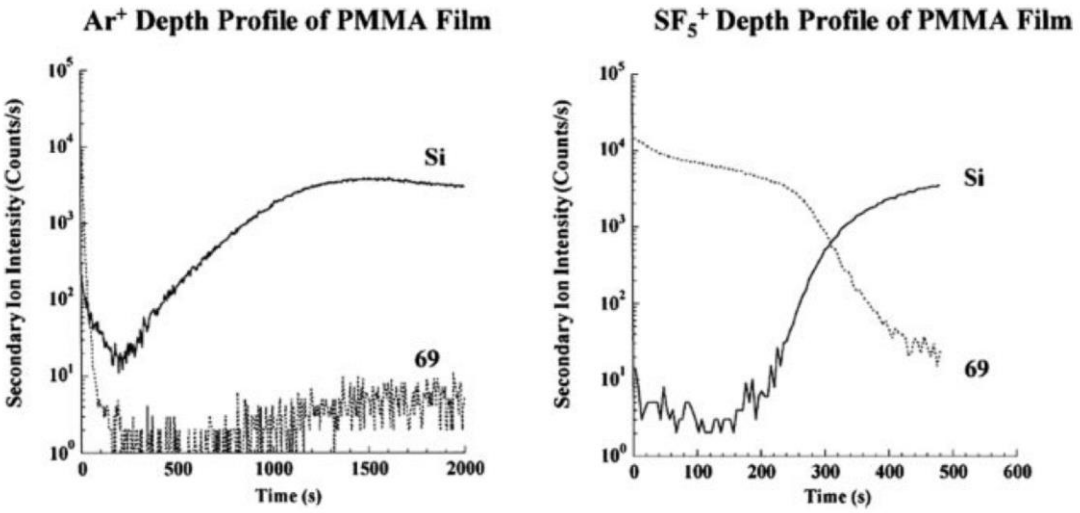

Figure 1.7: Comparison of depth profiles obtained from a 50 nm thick, spun-cast film of PMMA using Ar^+ and SF_5^+ primary ion bombardment under dynamic SIMS conditions [55].

MONOATOMIC SOURCES

Low energy monoatomic sources such as caesium or xenon are also used for organic depth profiling. In this case too, two types of degradation are observed. Normally, polymers such as polystyrene or polycarbonate cross-link due to the formation of free-radicals under primary ion bombardment. When using Xe^+, the free radicals react with each other and the polymer degrades rapidly into a heavily cross-linked, graphite-like structure with no memory of the initial polymer's chemical structure. No molecular information is kept and the sputtering yield is dramatically decreased. When using Cs^+, the free radicals react with the implanted Cs^+, which prevents cross-linking but also helps the emission of negative molecular fragments from the polymer [58]. The pmMa instead, behaves differently and very high sputtering yields are measured with both Cs^+ and Xe^+ ions. This probably indicates ion-induced de-polymerization of the polymer or at least a strong fragmentation into low molecular mass species. Though depth profiling is possible for this material. In Figure 1.8, intensities of high mass fragments are more intense using Cs^+ sputtering indicating that this element plays a key role in ionization processes too (described in next sessions).

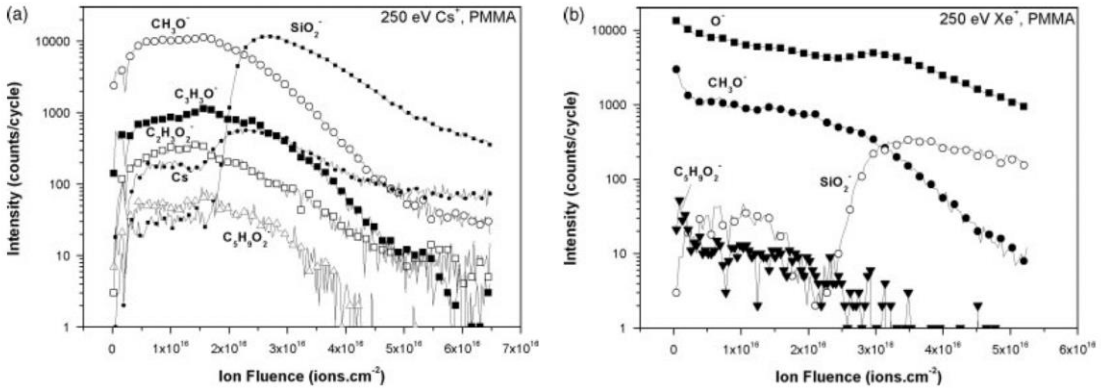

Figure 1.8: Negative ion ToF-SIMS depth profile obtained with 250 eV Cs^+ ion sputtering (a) and 250 eV Xe^+ ion sputtering (b) of a 50 nm pmMa layer deposited on a silicon substrate [58].

1.1.3 IONISATION MECHANISMS

Particles created during the sputtering process are composed of a large fraction of neutral chemical species and less than 1% is ionised (negatively or positively). This small portion corresponds to the chemical information collected by SIMS; it is then important to comprehend the ionisation mechanisms to understand the impact of the analysis conditions.

1.1.3.1 INORGANIC MATERIALS

Unfortunately, a significant part of the ionisation process is still unexplained due to the complexity and to a large number of interactions in the system. Ionisation can vary of many decades for an element. The variation is principally linked to the electronic affinity (ionisation potential) [59] of elements and the composition of the matrix surrounding them (matrix effect). Due to the electrostatic affinity, the elements can acquire a positive or a negative charge. It is then important to choose the appropriate polarity (extraction field) during analysis.

Another aspect deriving from ion bombardment is the implantation of primary species. In the case of passive elements (argon or xenon), their effect is mainly limited to the mere physical implantation. This is not the case of primary reactive sources (caesium and oxygen) in which the quantity and the depth of implanted elements vary the chemical and ionisation behaviour of the first few monolayers [60]. Significant contributions to this argument come from the works of Wittmaack *et al.* [61] and Vandervorst *et al.* [62].

The secondary ion generation has shown to be dependent on the primary source used. Bombarding the sample by caesium the electronegative element yield is enhanced [63], while positive element yield is favoured during oxygen bombardment [64]. In the case of inorganic materials, the two principal ionisation processes are the redox and the MCs_n^+ [65] process where M is the target atom.

Oxidation process with O_2^+: $M \rightarrow M^+ + e^-$

Reduction process with Cs^+: $M + e^- \rightarrow M^-$

Caesium is one of the most reactive elements of the periodic table, with the lowest electronegativity and strong reducer. When implanted into the polymer, it efficiently reduces the macromolecules. Generated fragments by ion impact create anions following the generic redox reaction:

$$Fragment + Cs \rightarrow Fragment^- + Cs^+$$

As far as surface is bombarded with positive Cs^+ a neutralisation method of positive charges has to be used. This neutralization is done during SIMS analysis using an electron flood gun [58]. This solution gain much more in interest for strong insulating layers.

MCs_n^+ process consists in the recombination of neutral chemical species (M_0) with the reactive element (Cs^+). The ionisation yield is higher than the atomic element M, but this method is limited only to caesium bombardment [65].

Dimer MCs_n^+ process: $M + Cs^+ \rightarrow MCs^+$

Trimer MCs_n^+ process: $M^- + 2Cs^+ \rightarrow MCs_2^+$

In the case of chemical elements chemo-adsorbed on surface such as caesium, the ionisation is ruled by the charge transfer between the primary ion and the target [65]. In the case of oxides or halides, the ionisation takes place by ionic or covalent bond break [62, 66].

In dual beam ToF-SIMS, the current density of sputter beams is usually orders of magnitude higher than the analysis beam. As a consequence, the surface chemistry and ion formation mechanisms are predominantly determined by the sputtering beam and optimised by the choice of primary ions, energy and angle of incidence. Normally, ${O_2}^+$ and Cs^+ beams with energies lower than 1 keV are used thanks to the high ion positive and negative yield respectively. For both sources the enhancement of the secondary ion yield is directly linked to the increasing surface concentration of the reactive ions that varies depending on the acceleration energy on the target and stopping range depth. The decreasing sputter yield at low sputter energies leads to higher surface concentrations of the sputter species with a consequent stabilisation of the ion yield. It has been

demonstrated by Berghmans and Vandervorst [67] that in the case of low energy sputter caesium energies, the secondary ion intensity of silicon is enhanced. The reason is that caesium atoms share a negative charge to the outer surface decreasing the working function and promoting negative ion formation as proposed by Verhoef [68]. The particularity of caesium is its variable concentration on surface during sputtering. In particular, several studies have shown that the maximum caesium surface concentration ($[Cs]_{MAX}$) that can be achieved during caesium bombardment is directly related to the sputtering yield of caesium (Y) in the material according to Eq.1.4 (for more details see Brison *et al.* [69]).

$$[Cs]_{MAX} \propto 1/(1+Y) \qquad \textit{Eq.1.4}$$

It is also shown that the higher the energy, the higher the sputtering yield, the lower the retained caesium surface concentration and the lower the work function variation, as shown in Figure 1.9.

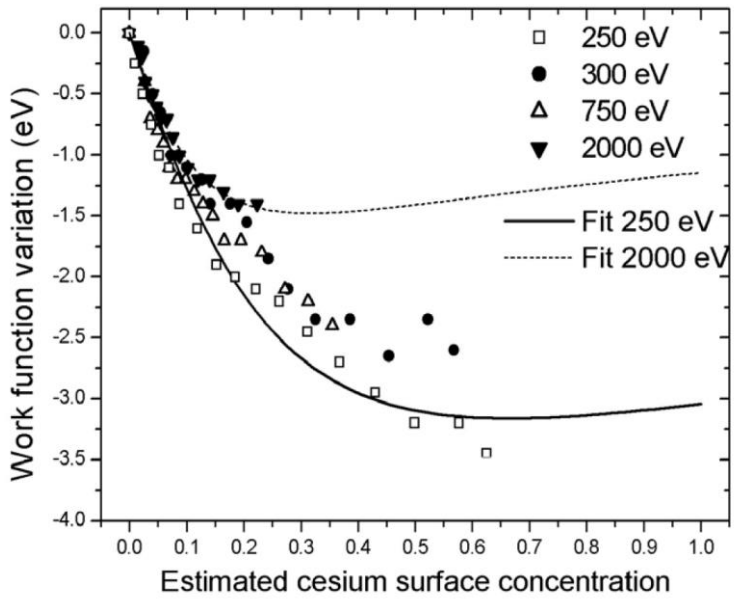

Figure 1.9: Variation of the silicon work function on the estimated caesium surface concentration for four different beam energies ranging from 250 to 2000 eV and modelling of the 250 eV and the 2000 eV curve [69].

Moreover, results showed that for fixed caesium coverage, the work function decrease is lower for the highest energies. This effect is because caesium ions are implanted deeper for high energy beam compared to lower energies.

A recent work came to the conclusion that implanted caesium ions diffuse in relatively short time scales to the sample surface to form adatoms [70]. The high mobility of

caesium is supported by the formation of caesium oxide dots in both inorganic [71] and organic [72] surfaces in areas with high caesium concentrations once the samples are exposed to air.

A limitation of this ionisation yield sensitivity to primary chemical nature is the quantification by SIMS; in fact, this technique is classified as "semi-quantitative". The ionisation probability of each ion is partially dependent on the surrounding environment defined as "the matrix" [10]. The same chemical species located in two different chemical environments may be subjected to different secondary yields. Matrix effects often impede the exact determination of doping elements in semiconductor substrates. This impediment is still a limitation in ToF-SIMS technique but there is always the possibility to compare samples composed by a similar matrix. The quantification is possible if strict standards protocols are kept [73], although these operations are difficult to apply to a large selection of materials. In the case of molecular organic materials, the situation is even more complicated.

1.1.3.2 ORGANIC MATERIALS

The ionisation phenomena of macromolecular samples differ from the inorganic materials. In this case, the direct ionisation generated by the impacting primary ion is not the predominant phenomenon [10]. A distinction between the generation of molecular ("parent-like") and fragment ion phenomena is conducted.

PARENT-LIKE IONS

Parent-like ionisation can occur in many different ways. Cations are formed by the association of a molecule with a cation and vice versa, parent-like anions formation occurs through the association with an anion or the loss of a proton. It is commonly accepted that the association of the molecule with an ion takes place a few angstroms above the sample surface during the desorption process [74]. A list of major ionisation pathways is presented:

- The ejection of an electron from an entire molecule M. This mechanism happens with apolar and aromatic hydrocarbon molecules,
- Polar molecules are ionised via Brönsted-Lowry acid-base reaction. It consists of the exchange of a H^+ proton generation $(M+H)^+$ and $(M-H)^-$. These ions can be either pre-formed on surface either induced by bombardment,

- Charged molecules may also be formed by metal cationization (Na^+, K^+, Cu^+, Ag^+ or Cs^+) to form $(M + Me)^-$. Alternatively, H^-, Cl^-, Br^-, Au^- induce negatively charged aggregates.

Metal cationization was studied in the '80s [8, 75] and recently by Delcorte *et al.* [50] being able to determine the oligomer distribution centred around the polymer molecular weight (M_w) of a polystyrene (PS) equal to $1100\ amu$ (Figure 1.10). In general, there are several series of peaks in the positive spectrum of Ag-cationised PS oligomers: (i) the fingerprint region ($0<m/z<200$), with fragments formed from one or two repeat units or including chain-ends; (ii) the cationised oligomer distribution (centred around the polymer molecular weight); and (iii) the fragmentation region (intermediate), with a distribution of cationised fragments.

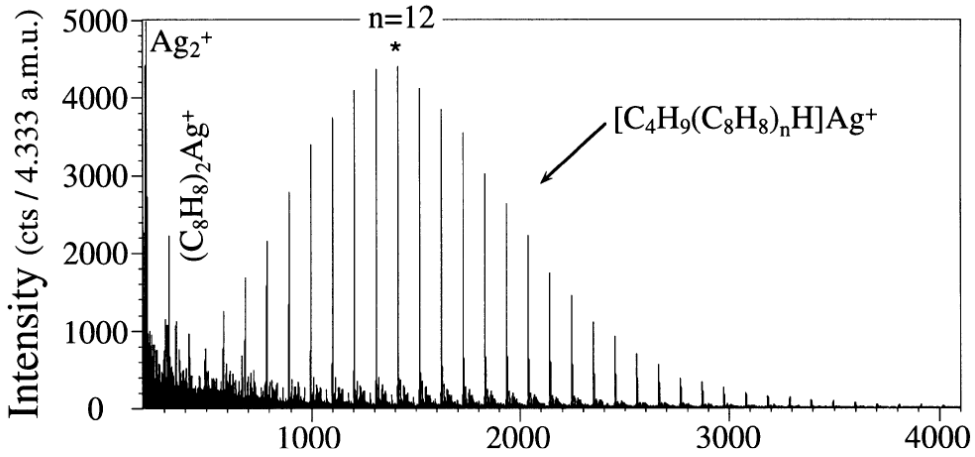

Figure 1.10: Positive secondary ion mass spectrum of PS1100 cast on a silver foil [50].

This method used to determine the M_w is not applicable for molecular weights un to $5 - 8\ kamu$ because cationised molecules are too heavy to be extracted and analysed by the time of flight spectrometer.

FRAGMENT IONS

In the case of fragments deriving from organic molecules, the ionisation can occur by recombination reactions such as these described previously. As an example, the characteristic fragment of polystyrene $C_7\ H_7^+$ is the result of the association of $C_7\ H_6^+$ with a proton H^+, while $(C_8\ H_8\ )Ag^+$ is observed in spectra for oligomers adsorbed on silver [50].

High molecular weight polymers are different from oligomers mainly because the secondary species under investigation are necessarily characterised by fragments. Ions are generated by bond-scissions and fragment rearrangements activated by degradation processes. Therefore, the decrease of high mass signals in-depth profiling during bombardment fluence is not caused by the disappearance of the sample but by the physicochemical modification of its surface (chain scission, cross-linking or dehydrogenation reactions).

MATRIX EFFECTS

As for inorganic materials, matrix effects can occur in organic materials. There are myriads of organic materials that may be of interest and the extraordinary array of combinations of these cannot be practically addressed by reference materials. The main contributions come from the works of Seah and Shard *et al.* [76, 77] on the identification and comprehension of matrix effects on organic blend materials. To study this issue, various polymer stacks with different types of Irganox [1] in variable concentrations were prepared and in-depth profiles carried out to study sputtering yields and ionisation behaviours. Matrix effects were evidenced through the observation of sputtering yield variations in Figure 1.11-a. Sputtering yield is normalised by Irganox 1010 and a decrease of Y is observed while increasing the Irganox 1098 content but it is not univocal for any kind of polymer blend. The matrix effect has also an important contribution on the generated secondary ions. In Figure 1.11-b, three unique ions for Irganox 1010 and Irganox 1098 have been plotted after normalisation. Resulting intensities show both enhancement and suppression indicating a non-lineal trend in mixtures.

Therefore, the only practical approaches to obtaining reliable quantitative data from SIMS are either: to eliminate or reduce matrix effects or to understand and correlate them. The first step is then to find suitable materials that display matrix effects so that, following the latter approach, the effects can be classified and described and attempts to mitigate the impact.

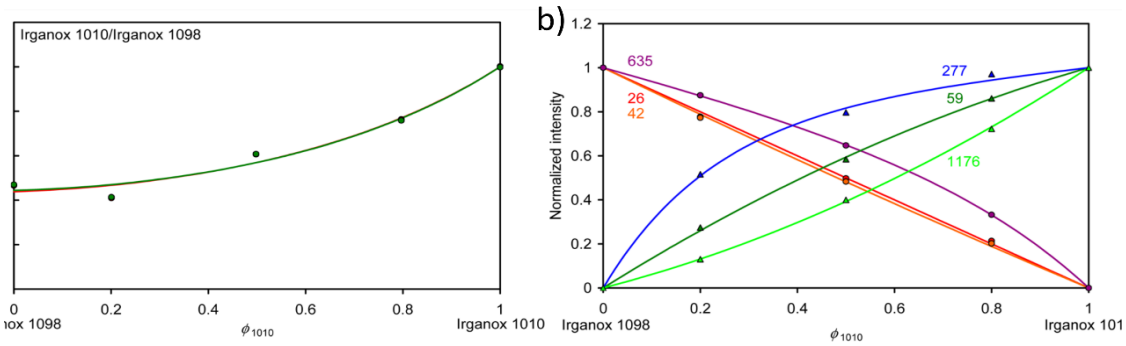

Figure 1.11: a) Sputtering yields of the mixtures of Irganox 1010 and Irganox 1098, normalised to the sputtering yield of Irganox 1010, as a function of the volume fraction of Irganox 1010. The fitting curve underline the decreasing trend and b) normalized intensities for secondary ions representative of Irganox 1010 (red, orange and purple) and Irganox 1098 (dark green, blue and light green) [77].

All the concepts in terms of sputtering and ionisation phenomena previously presented refer to the studies performed on solid and dense materials. However, low density and soft materials have been recently included in the growing panorama of SIMS characterisations and the fundamental concepts have to be verified or reinterpreted.

1.2 State of the art in the comprehension of the chemical information for fragile materials

The application of low densities and soft materials in the micro and nanotechnology domain is getting large. In this work the behaviour of these innovating materials under specific ToF-SIMS analysis conditions is explored by studying the ion/matter interactions and secondary ion generation.

The first material category is porous silicon, a form of silicon with generated porosity in its microstructure inducing a large surface to volume ratio and the possibility to vary surface functionalization with promising applications are in the field of bio-inert or bioactive materials, energy storing and optics.

The second category of materials concerns polymers widely integrated into micro and nanotechnologies and subjected to critical working conditions , i.e. nanometric thin films.

The third category concerns low dielectric constant insulators (low-*k*) successfully used as insulators between interconnection lines of integrated circuits. These materials are characterised by a structural and chemical fragility introduced by pores and by their hybrid (organic/inorganic) state [78]. Pores characteristic of these materials (nano-pores

generated by porogen agent stirring) have a different nature compared to p-Si meso-pores (dendritic shape) and do not generate the same type of fragility.

1.2.1 POROUS SILICON P-SI DEGRADATION UNDER ION BOMBARDMENT AND RELIABILITY OF SECONDARY ION INFORMATION

Porous silicon was first discovered in 1956 during electropolishing experiments [79].

Nowadays p-Si finds an industrial application in sensor technology and many other application fields briefly described in chapter 1.

In Figure 1.12 classical porous structure of a sample similar to the ones studied in this work is presented. Incorporated voids (pores) have a dendritic structure and each pore is separated by the ones next to it by thin silicon membranes. These silicon membranes have origins from solid pillars that keep the solid structure preventing to collapse.

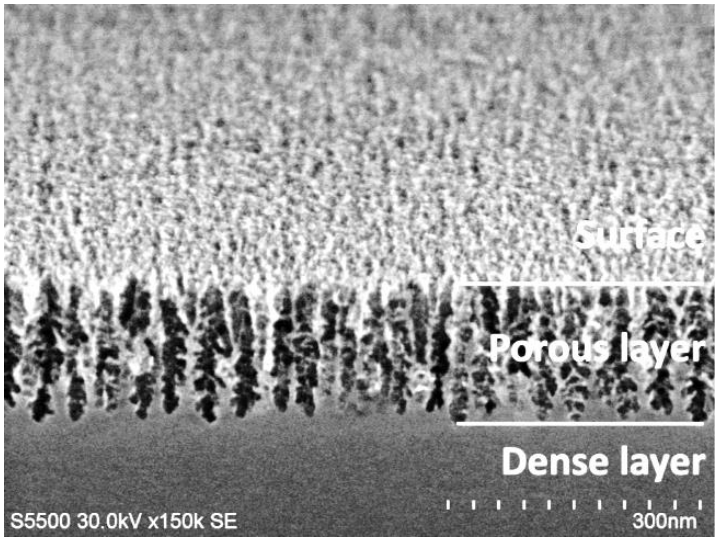

Figure 1.12: 40° tilt SEM image of a porous silicon layer. In the image, the columnar shape of the porous layer can be clearly observed.

Physical properties of p-Si are tightly connected to the morphology of the material and above all to its chemical composition. The zone with the highest chemical variations on a p-Si is the surface, with a specific area of more than 500 m^2/cm^3 and surface chemical composition affects enormously optical, electrical and adhesion properties; natural aging, intentional oxidation and surface modifications are then used to induce chemical changes. The preservation of the demanded function and operability for a specific technological need are required. A reliable surface and in-depth chemical characterisation is then required to connect the physical properties with the material chemistry.

This large variety of applications depending on a specific chemistry demands a huge effort of characterisation that often have to face with the detection of doping elements present in traces and the degradation phenomena occurring during analysis.

As porous silicon is an extremely fragile and reactive material [1], chemical or morphological alterations can occur during its lifetime as well as under analysis. It is the case of electron microscopy or photoluminescence spectroscopy (PS) and all the characterisation techniques using high energetic ions [2, 3], electrons [80, 81] and X-ray beams [82] or lasers [83, 84] as primary source.

The presence of voids can be an obstacle to the heat transfer induced by laser or ion irradiation, that coupled to the nanometric dimensions and chemical composition of the solid silicon structure, can induce a melting at lower temperatures compared to bulk dense silicon. For instance, the melting phenomenon has already been observed on porous silicon by single laser pulses during adsorption/ionisation characterisations [85]. In Figure 1.13 the comparison of porous silicon before and after laser exposure reveals an important morphological modification interpreted as fusion.

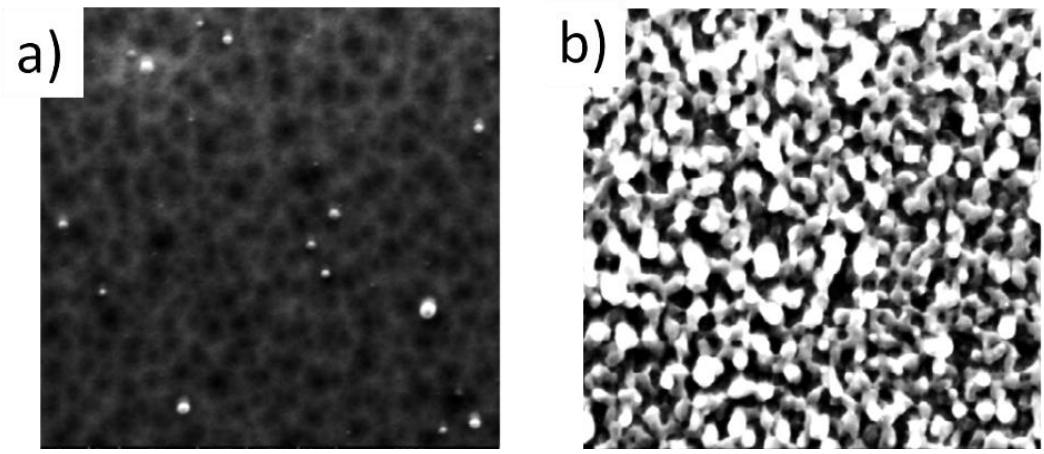

Figure 1.13: SEM images of desorption/ionisation on porous silicon surface a) before and b) after the exposure to single laser pulses of 15 mJ/cm^2 revealing surface rearrangement. Field of view 1.7 µm [85].

It has been shown that high energetic ions (H^+ and Ba^+ at 500 keV) produce artefacts during analysis [2] and the structure of the sample under investigation is damaged. In particular, ion implantation destroys mechanically the porous structure until the porous layer transforms into a compact material of pore columnar orientation is deviated.

It is then logical to think that ToF-SIMS can be the source of similar issues because energetic ions are used inducing issues in the dissipation of the transferred energy during

ion impact. The dissipation is function of the primary ion energy, target chemical composition and configuration such as pore shape, dimensions and concentration.

ToF-SIMS has been used for the evaluation of p-Si induced detrimental effects of plasma-based pattern transfers [86]; it is shown that depending on the overall porosity and plasma used, the penetration depth of plasma agents changes and important modification of the surface chemistry are observed. However, only the effect of plasma etching was considered and evaluated while an additional study on a potential p-Si morphological modification after SIMS analysis was not proposed.

The lack of information in bibliography on p-Si analysis by SIMS technique forces the research of similar systems to be compared with. Studies concerning morphological modifications and chemical information reliability for nanometric particles under ion bombardment can be considered as relevant. Indeed, in the case of nanoparticles, the recurrent melting phenomenon under SIMS ion bombardment was observed. To be more precise, ion bombardment can induce a material melting that takes place at a temperature lower than the one of the bulk material due to the nanometric dimensions [87, 88]. The decrease of melting temperature is related to the large internal surface of nano-objects (nanoparticles as well as pore solid walls) that allows additional degrees of freedom for the thermal atoms vibrations [84]. In the particular case of nano-particles, this phenomenon is even more amplified by the reduced contact with the substrate and radical changes of the morphological aspect were observed. The target chemical composition is also fundamental as it determinates if a sample is thermally conductive or refractory.

Particularly interesting are the results obtained using mono-atomic (Cs^+, O_2^+) low energetic sputtering conditions on SiO_2/Au and $SiO_2/Ag/SiO_2$ 138 nm core-shell nanoparticles (Figure 1.14-a-b). In particular, 500 eV Cs^+ bombardment showed a good conservation of the gold core intact. On the contrary, the silicon dioxide shell melted under applied sputtering conditions. In the case of 98 nm gold nanoparticles bombarded by 20 keV C_{60}^{++} primary ions (Figure 1.14-c-d), SEM studies confirmed this early melting, but the particle shape was largely maintained.

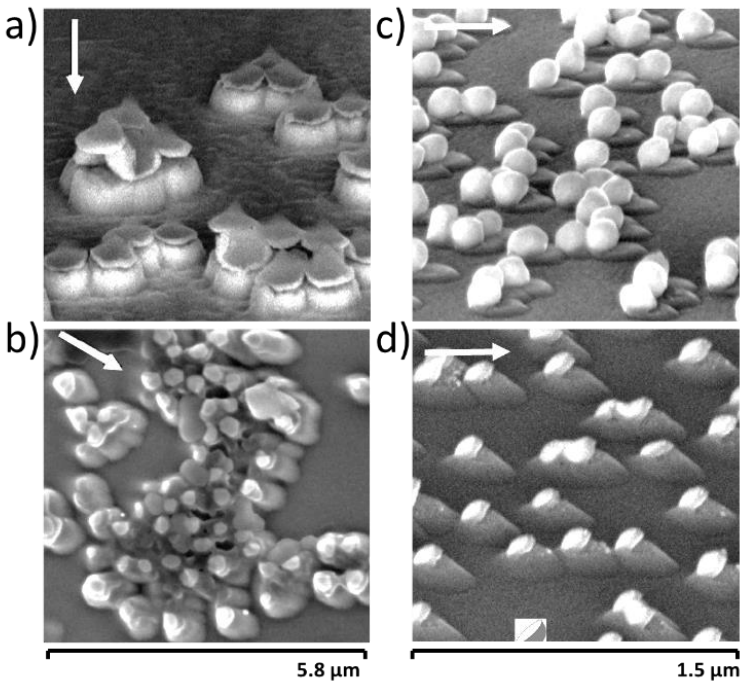

Figure 1.14: SEM images of:

a) $SiO_2/Ag/SiO_2$ particles after $500eV$ O_2^+ bombardment

b) SiO_2/Au particles after $500eV$ Cs^+ bombardment [4]

c) Au particles after $5x10^{18}$ ion/m^2 and

d) $20x10^{18}$ ion/m^2 fluences of 20 keV C_{60}^{++} bombardment [89].

Harrows indicate the direction of primary ions.

In both these studies, melting was not mitigated by sample cooling (during analysis samples are placed on a holder that can be cooled by liquid nitrogen or heated by resistances). The authors concluded that without a good heat sink, profiling nanoparticles and analysing their surfaces may not be at all straightforward with SIMS. The impeded heat transfer due to the spherical shape of particles induces the melting phenomenon. Once the SiO_2 layer is melted, it becomes heat conductor and the energy is transferred through the underlying substrate. Yang *et al.* [4] underline the problem of the heat sinking as the principal responsible for nano-particles melting under ion bombardment. The increase of temperature for each single particle is directly linked to its diameter as well as to the energy of the primary ion and the number of impacting ions, as shown in Figure 1.15.

This figure shows clearly that for nanometric systems melting can easily occur also at low bombarding energies (500 eV) in opposition to bulk materials calculated coupling the Dulong–Petit law, consisting in a thermodynamic rule that states the classical

expression for the molar specific heat capacity of certain chemical elements, with the melting point depression. The melting point depression is the phenomenon of reduction of the melting point of a material with reduction of its size. This phenomenon is very prominent in nano-scale materials, which melt at temperatures hundreds of degrees lower than bulk materials.

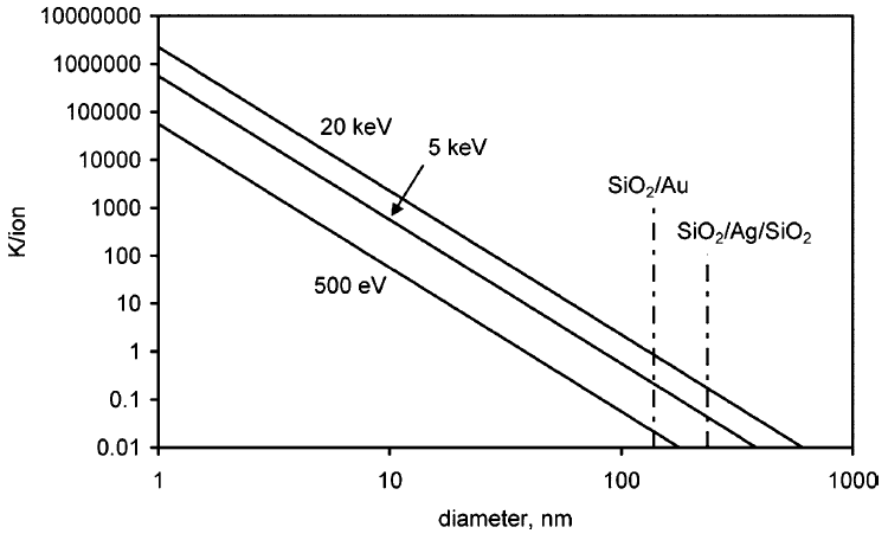

Figure 1.15: Rise in temperature per incident ion as a function of a nanoparticle diameter and for different incident energies, supposing it is isolated with no heat losses [4]. These values are independent from the nanoparticle chemical composition and type of incident ion.

The parameters of the ion beam impacting a nanometric shaped surface, as well as the chemical composition of this surface are then important factors that have to be explored and correlated to the modification induced to the target.

As stated before, many similarities could exist permitting the comparison of porous silicon and nanoparticles systems. In Figure 1.16 these similarities are summarised and consist in a comparable nanometric scale, limited heat sinking and 3D structured surface. It is important to remind that pore surface is also covered by silicon dioxide and as describes for SiO_2/Au nanoparticles, the oxide melts under primary ion bombardment conditions.

A thermodynamic study would add a good complement to this comparison but is beyond the scope of this work and will be not developed here. A relevant importance will be given to the interpretation of ion/matter interactions during ion bombardment. This objective will be achieved by analysing in detail the chemical information modifications induced during SIMS analysis in comparison with the expected morphological modifications induced by ion bombardment. To do so, in chapter 1, a set of porous silicon

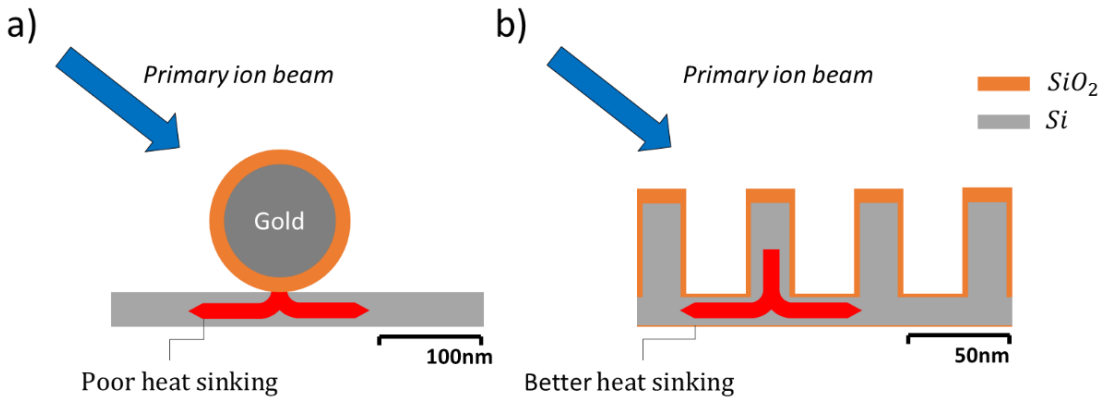

Figure 1.16: Comparison between a) nanoparticle on a flat structure under primary ion bombardment and b) columnar porous structure. In both cases, the exposed surface is not flat. It can be assumed that each porous pillar corresponds to the top area of a nanoparticle.

samples with a varying overall porosity are sputtered by different primary ion sources; results are compared by a phenomenological and chemical approach.

1.2.2 MAXIMISING THE CHEMICAL INFORMATION ACHIEVABLE FROM METHACRYLATE THIN POLYMER FILMS

In the recent past years, polymers started to be the more and more studied in the micro and nanotechnology development thanks to their versatility and low cost of production [5]. In general, polymers used in microelectronics need characterisation techniques sensitive to extremely thin films. Ideally, these techniques have to be able to give fine chemical information about composition while keeping an ideal depth resolution in order to correctly determine interfaces in the cases of stacks [5].

In this work, in particular, the research is focussed on the characterisation of thin films deposited by an innovating Chemical Vapour Deposition (CVD) technique called initiated CVD [90, 91]. Essentially, i-CVD can be considered as a free radical polymerization without the use of a liquid phase, conveniently combining polymerization and coating in a single step (more details in chapter 3). Since the i-CVD method uses initiated radical polymerisation process, a good control of the resulting polymer chemistry can be potentially obtained by controlling the injection of initiator and monomer.

At present, one of the challenges of this deposition technique is to obtain a good control of the film molecular weights. In the wide panorama of characterisation techniques, ToF-SIMS is one of the most promising. This statement finds its explanation thanks to the high mass resolution coupled with an outstanding mass detection range of this technique. By

since the continuous evolution of primary sources brought to the introduction of the first polyatomic analysis sources with a reduced sample degradation during depth profiling and an increased high mass chemical information. The first polyatomic source was the SF_5^+ [92, 93] shortly replaced by C_{60}^+ source [94] with promising results for the organic depth profiling. This solution was limited to a low selection of organic materials due to the damage accumulation and roughness formation [37]. Indeed, many polymers cross-linked under C_{60}^+ bombardment impeding the right in-depth profiling as shown in section 1.1.2.2. Among the solutions explored two of them were the most effective:

- Sample cooling [35] with the objective of freezing molecules preventing them to cross-link, this solution was investigated by Mahoney *et al.* [36, 54] in the case of SF_5^+ sputtering
- Use of reactive NO (nitric oxide) in the analysis chamber with the objective to trap the radicals formed impeding polymer branching [95].

Initially proposed in applications such as X-ray photoelectron spectroscopy (XPS) [96], argon cluster ion sources started to be applied in ToF-SIMS technique. ToF-SIMS chemical information [97] was shown to be well preserved and improved depth resolution was obtained [77, 98]. This solution has proved to be particularly adapted by Yamamoto *et al.* [99] for the evaluation of damage induced on organic materials by monoatomic argon ions irradiation.

With the introduction of gas cluster ion beam GCIB as sputtering source, systematic studies to find out the connection between bombardment conditions and analysed material behaviour were carried out. Seah [34] proposed, by empirical observations, the link between the energy (E) and cluster size (n) of primary cluster ions and the sputtering yield (Y) of a given material (Eq.1-5).

$$\frac{Y}{n} = \frac{B\left(\frac{E}{An}\right)^{q}}{1+\left(\frac{E}{An}\right)^{q-1}} \qquad \textit{Eq.1-5}$$

A is a parameter related to the bonding energy per atom required to eject the sputtered fragments, q is a power index in the range 2–4 and B is a parameter in the range between 0.18 nm^3 to 0.27 nm^3 , which is of the same order as the volume occupied per atom ignoring the hydrogen atoms. Listed values are determined by fitting experimental data obtained on a large variety of materials, in a broad range of sputtering conditions. It is then possible to plot the sputter yield vs. energy per atom and the result is presented in Figure 1.17.

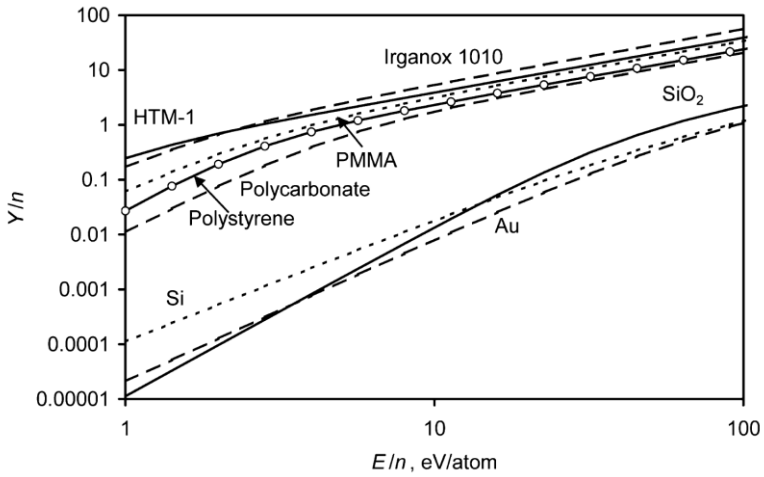

Figure 1.17: Argon GCIB sputtering yields per atom as a function of the energy per atom for organic and inorganic material obtained by Seah (ref. [34]).

A clear distinction between organic and inorganic materials is evidenced. Low sputtering yield is associated with inorganic materials where sputtering at low E/n values is almost insignificant. High sputter yields correspond to organic materials with no particular distinction between the two kinds of degradation (depolymerisation and cross-linking) suffered by polymeric materials (section 1.1.2.2). In addition, Cristaudo *et al.* recently pointed out that the degree of polymerisation can play a key role in the modification of polymer sputter yield especially at low M_w. This phenomenon, studied on pmMa and PS, is shown in Figure 1.18.

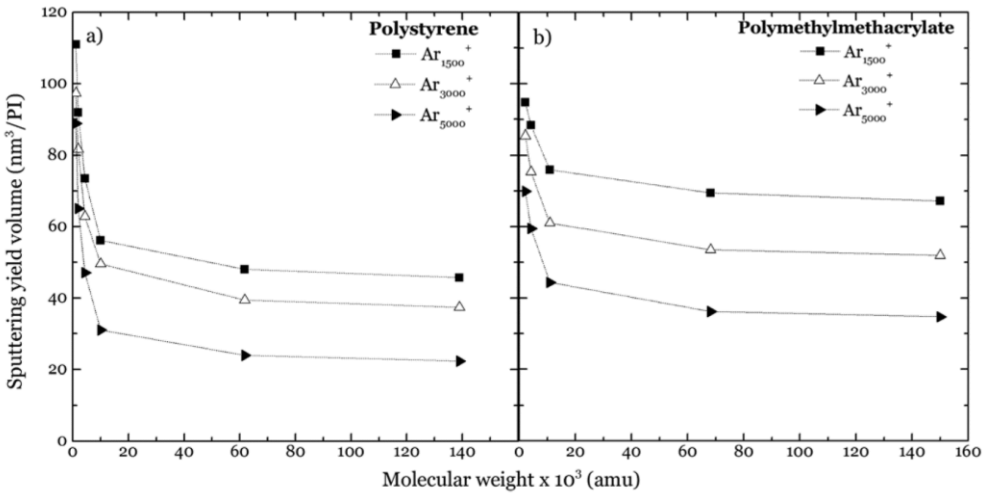

Figure 1.18: Sputtering yield volume versus molecular weight of pS (a) and pmMA (b), obtained for three different 10-keV Ar cluster ions (nominal mean cluster size of 1500–3000–5000 atoms/ion, respectively) (ref. bib. [100]).

An improvement was then proposed by Seah to upgrade his universal equation (Eq.1-5) for GCIB sputtering yields introducing the M_w variable in the proposed model

[34]. In particular, *A* parameter, that reflects the average fragment release energy per atom, decreases as the molecular weight decreases and it is inversely proportional to the number of end groups per nm^3 [101]. The general concepts of the universal equation for sputtering yields by cluster ions were accurately upheld.

In parallel with the use of gas cluster ion sources, monoatomic sources are still used with success for the characterisation of organic materials. In particular, low energy sputtering is successfully used for the in-depth depth profiling of organic samples as shown by Houssiau *et al.* [58, 102, 103] applying energies lower than 500 eV to prevent the sample degradation by cross-linking or graphitisation (section 1.1.2.2). The second advantage is the incredible enhancement of the ionisation of organic fragments occurring thanks to the implanted caesium.

The ability of ToF-SIMS to successfully profile polymers stacks by using large gas cluster ion beams was already explored [104]. The difficulties deriving while characterising polymers are due to the complex geometries of these materials and, in particular, their thickness. At these dimensions, intrinsic properties such as degree of polymerisation and blend quantification in the case of mixture become fundamental.

It is then fundamental to identify and understand the integration processes mechanisms and their effect on the obtained product. Furthermore, specific analytical needs are requested to characterisation such as molecular information, in-depth profiles etc. In this context, ToF-SIMS appears a well-adapted technique already known to be an excellent instrument for surface characterisation.

The ability of ToF-SIMS to successfully profile polymers stacks by using large gas cluster ion beams is stated and explored in chapter 3. In particular, an i-CVD deposited double-stack sample composed of quasi-identical polymers is characterised in depth. This preliminary work is then used to develop a protocol for the quantification of copolymers films composed of the same repeating units as a double-stack sample. Moreover, the high mass secondary ion information produced while analysing M_w varying samples is thought to be dependent by the degree of polymerisation as observed in previous works but not achieved for high polymerisation degrees (section 1.1.3.2). In this case, the sputtering yield modification observed by Cristaudo *et al.* suggests that fragmentation phenomena are linked to the molecular weight and then to the produced secondary ion information. To verify this hypothesis, low damaging analysis conditions have to be used coupling the detected secondary ion information with statistical tools for the appreciation of the complex multivariate data system.

1.2.3 MAXIMISATION OF THE ELEMENTAL CHEMICAL INFORMATION OF DIELECTRIC MATERIALS USED IN MICROELECTRONIC DEVICES

Performance improvements in microelectronic integrated circuits (ICs) over the past few decades have been achieved by reducing transistor size and packing more transistors onto a single chip. An emerging factor that may disrupt this trend is the slowing speed of signal propagation within the chip. Signal delays, caused by the interconnection wiring, increase with each generation of scaling and may soon limit the overall performance of the integrated system.

Conventional materials such as Al and SiO_2 were replaced by materials with higher performances such as Cu for conductive lines and cross-linked hybrid organosilicates glass (OSG) $SiOCH$ as insulators [105]. The insulating dielectric materials are also loaded with porogen agents [106] to promote the formation of porosities inducing a structural fragility to the final material but in parallel enhanced dielectric properties.

Deposition of a uniform, thin and porous low-*k* film is only the first of many steps. As a matter of facts, the real challenge is the integration of these film into IC manufacturing processes. Indeed, the low-*k* films need to be etched and cleaned to pattern conductive lines and prepare a clean surface for subsequent processes and deposition steps. As these etching processes are repeated for each interconnection level (about 10 for a 28 nm technological node), the impact of these steps on the overall chemistry must be explored [107]. One central point to this damage is the adsorption of water in the porous dielectric material, this uptake results detrimental for the insulating properties (more detains in chapter 4).

After the plasma etching processing, material characterisation aims at two objectives:

- verify that the plasma processing reached the desired morphological characteristics in the case of patterned films achieved by scanning microscopy
- verify that the low-*k* retained its original properties (no water adsorption, no deterioration of the *k*-value and the mechanical properties)

The chemical characterisation of patterned plasma-induced damage results complicated due to their non-planar morphology. Although it is easier to characterise non-patterned (blanked) wafers, though plasma damage of low-*k* dielectrics remains a complex phenomenon. It involves both physical and chemical effects due respectively to ion bombardment (energy distribution and flux of each ionic species) while chemical reactions between the plasma and low-*k* constituents and/or induced by plasma radiation. The increase of the dielectric constant is directly correlated with the changes in bonding

configuration, to the formation of carbon-depleted layer and surface densification. The carbon depleted layer becomes hydrophilic due to the presence of $Si-OH$ bonds and adsorbs moisture that drastically increases the dielectric value. The in-depth chemical plasma damage was determined by the diffusion of active radicals (O, H, F, etc.) into the pores of the low-*k* material and the removal of organic hydrophobic groups (SiH and $SiCH_3$).

Detailed studies of plasma damage were obtained by ellipsometric porosimetry (EP), where porosity, pore size distribution, and the proportion of adsorbed water was measured [78] . Another rising characterisation technique for non-patterned plasma damaged dielectric materials includes secondary ion mass spectrometry (SIMS) that measures the depth profile of various elements present in the film such as carbon depletion [108].

ToF-SIMS measurements in Figure 1.19 gives a clear idea about the nature of "chemical" damage. The pristine low-k film is characterised by a uniform carbon (organic groups) concentration. Further, it was found that (Figure 1.19-a) the CF_4 plasma etches the $SiOCH$ film without bulk material modification. After exposure to oxygen stripping plasma, the depth of carbon depletion directly depends on porosity and pore size. This is caused by an easier penetration of oxygen radicals into the pores. In Figure 1.19-b-c, the O_2 plasma oxidizes the $SiOCH$ film converting the top layer in a hydrophilic SiO_2-like porous material due to the deletion of carbon, removing hydrophobic $Si-H$ or $Si-CH_3$ bonds. These chemical modification make these dielectric films hydrophilic.

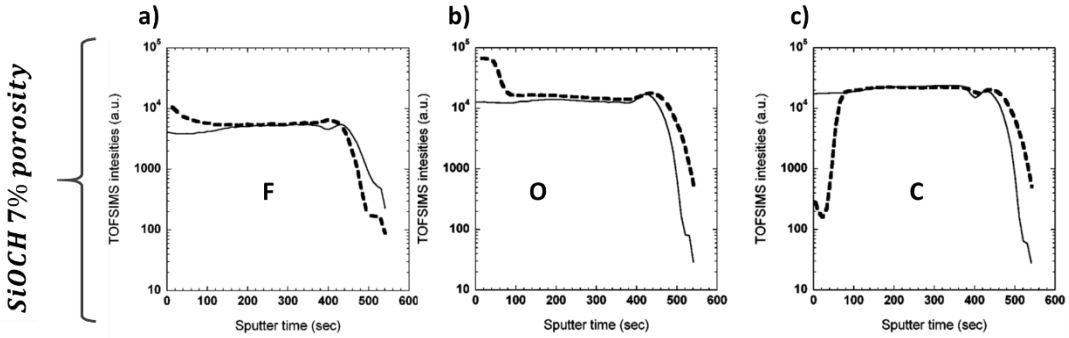

Figure 1.19: a) ToF-SIMS intensities of fluorine ion obtained for SiOCH 7% porous film. Thin curves represent films before plasma treatment, while bold dashed curves represent the same films after CF_4 plasma treatment. ToF-SIMS intensities of b) oxygen and c) carbon obtained for SiOCH 7% porous films before (thin curves) and after (bold dashed curves) O_2-plasma exposure [108].

ToF-SIMS was also applied on low-*k* materials treated with fluorine-plasma etching. The chemical modifications were interpreted by the use of statistical analysis methods to enhance chemical differences in samples after being exposed to plasmas. Results are

reported by Lazzeri *et al.* (Figure 1.20) and chemical surface variations were studied for three types of dielectric materials (SiO_2, nano-porous silica NPS and organosilicate glass OSG) before and after plasma etching C_4F_8/90% argon). In Figure 1.20, three main groups corresponding to the untreated OSG, NPS, and SiO_2 samples are present, while a fourth cluster commonly classifies all the dielectric materials after partial etching. The partially etched samples have common scores values because this plot highlights their major features compared to the untreated samples. The main differences in the static-SIMS spectra that are pointed out in this case are in fact the occurrence of fluorine and the disappearance of the fingerprints characterising the pristine materials.

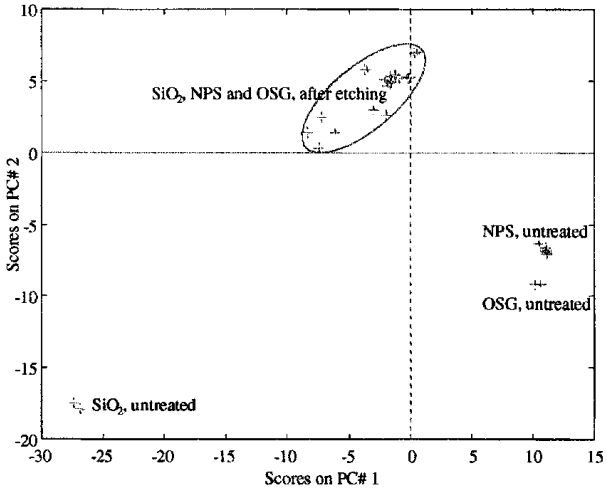

Figure 1.20: PCA scores/scores plot of negative static SIMS dataset. Spectra are normalised to the most intense peak before autoscaling. PC 1, 2 capture 49% and 29% of the variance, respectively[109]

Nowadays, fluorocarbon plasma chemistries are commonly used for etching. Although the damage in fluorocarbon plasmas is much smaller than in oxygen plasma, in most of the cases the etch damage exceeds the present technology requirements. Therefore, careful optimization of the etch processes is needed in each case or dielectric constant has to be re-established. The influence of adsorbed water on OSG reliability was reported by Li *et al.* [110] and between the attempted strategies to bring low-*k* properties to the original condition, the chemical surface treatment capable to substitute functionalising groups on the surface (the so-called "Restoration") [111, 112] was found to be a promising solution. "Restoration" process consists in a thermal annealing at 190 °C associated to surface silylation or UV-assisted thermal treatments.

The large use of these materials in the micro and nanotechnology panorama is now requesting a higher effort to the characterisation field. As these dielectric materials start to be hardily integrated into newer and more scaled technologies, a better knowledge of

the real chemical modification occurring during integration treatments and most of all their in-depth distribution is needed. This need is double fold; i) a precise information about chemical modification is needed and ii) an in-depth localisation of the modified layer as 3D nano-structuration is induced (porosity) to increase further dielectric properties. To accomplish this target, low-*k* materials already largely applied in microelectronic industries will be analysed at different stages of integration steps (plasma etching and "Restoration"). The variation of dielectric constant due to integration processes will be chemically interpreted by using the advantageous characteristics of ToF-SIMS technique such as high mass resolution and the possibility to analyse thin films with high depth resolution. These advantages are obtained using a low energy sputtering gun or large cluster ion gun and afterwards spectra are analysed applying Principle Component Analysis (PCA) to discriminate the integration treatments impacts on the low-*k* chemical composition. The unique insulation properties, chemical structure and the porous nature of the H or C rich low-*k* materials make SIMS analysis very challenging since the analysis itself can degrade the material such as for nanoparticles, porous materials or polymeric samples. In chapter 4 ,the impact of sputtering sources on this kind of cross-linked hybrid porous materials will be studied in order to determine the appropriate analysis conditions capable to couple a fine chemical information and an appropriate depth resolution.

1.3 ToF-SIMS INSTRUMENTATION, ACQUISITION AND DATA TREATMENT

In this Ph.D. work, a ToF-SIMS V designed by IONTOF (Münster, Germany) was used. The instrument is equipped with three types of primary ion sources, which geometry is arranged in order to have a 45° angle of incidence to the sample for all the produced ion beams. In this work, surface analysis was obtained by means of a liquid metal ion source (LMIG) producing a Bin+ (acceleration energy un to 30keV). When working in "dual beam mode" depth profiling, sample sputtering was obtained either by using a gas cluster ion beam (GCIB) source or a monoatomic beam (for Xe^+, Cs^+) produced in a dual source column (DSC) equipped with an election impact source (for O_2^+, Xe^+) and a surface ionisation source (for Cs^+). The system is also equipped with a low energy electron gun, necessary for charge compensation on insulating samples. The secondary ions generation by the analysis beam are then accelerated in the time of flight (ToF) analyser by an extraction potential.

1.3.1 PRIMARY ION SOURCES

LIQUID METAL ION GUN (LMIG)

Commonly used as analysis source it can be used to generate monoatomic (gallium or bismuth) or polyatomic (bismuth) ion beams. A schematic representation of the source is presented in Figure 1.21. The emitting part is composed of a reservoir containing the metal with a tip on the top. This reservoir is heated by a current to melt the alloy. A ring-like extractor is placed near the tip. A voltage is applied to the extractor that accelerates the metallic ions covering the tip. A balance is established between generated and extracted ions assuring the ion flux. The flux is then deflected to assure the pulsing. In this phase, the flux deflection also assures the ion mass selection. This pulsed working mode is necessary because the analyser works by measuring the time of flight. Good mass resolutions are achieved by using short pulses (<1 ns). In order to obtain the required pulse length, the relatively long pulse (~20-40 ns), obtained by flix deflection through an aperture, needs to be "shortened" by means of an "electrostatic bunching" technique; when the "long" pulse passes through the bunching plates, an electrostatic potential is suddenly applied. As a result, the ions in the "tail" of the pulse are accelerated toward

those in the front of the pulse, so that the ion packet hits the surface over a shorter time length.

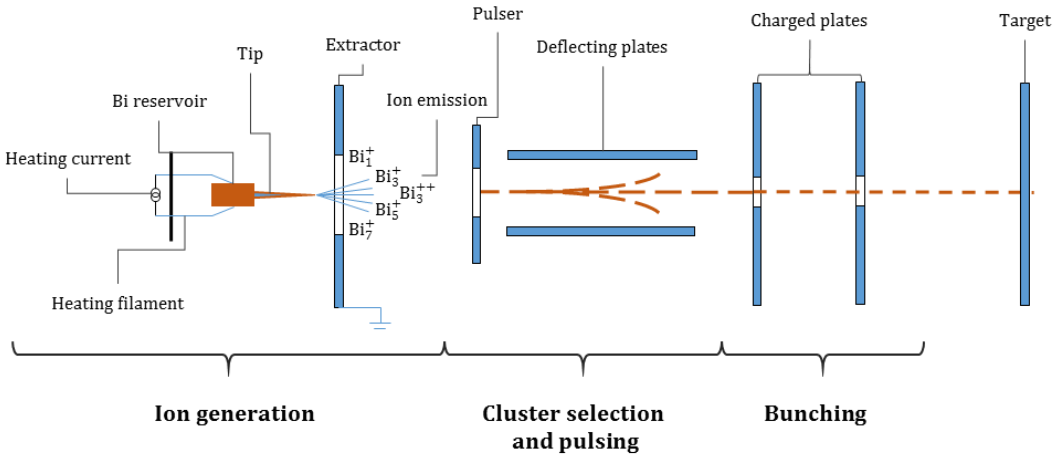

Figure 1.21: Schematic principle of a liquid metal ion gun (LMIG).

Liquid metal sources are the ideal compromise in versatility and efficiency thanks to the possibility to produce polyatomic ions. These ions are well focusing and sample damaging during bombardment is reduced.

SURFACE IONISATION SOURCE

Caesium ions are produced by a surface ionisation technology (Figure 1.22-a). This source is composed of a solid caesium reservoir that once heated, generates caesium vapour driven to a heated porous tungsten plug. Electrons are trapped by the tungsten as its work function is superior to caesium ionisation potential. Formed caesium ions are then extracted from the tungsten plug and injected into the optical column for focusing.

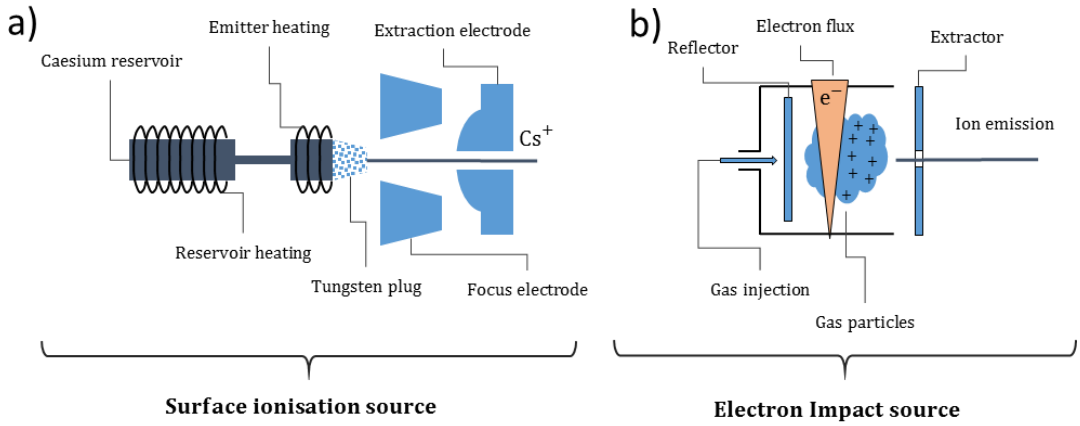

Figure 1.22: Schematic principle of a) the caesium surface ionisation source and b) gas ionisation by electron impact source.

ELECTRON IMPACT SOURCE

Electron impact ionisation (EI) is at present the main technique for ion generation from gaseous species such as noble gases ($He, Ar, Xe…$) or oxygen O_2 (Figure 1.22-b). The gas is injected in the source and it is bombarded by an electron flux. The impact of electrons with the gas atoms induces the ejection of an electron generating an ion. The electric field generated by a reflector forces the injection of generated ions into the optical column. Electron bombardment is a system also used for ion generation in GCIB source discussed in the next paragraph.

GAS CLUSTER ION SOURCE

The gas cluster ion beam used in this work can generate argon clusters variable in energy and in number of atoms. The advantage of this source is that it can be used as sputtering source or analysis source as well. The architecture of this source is schematized in Figure 1.23. As it can be seen, the design is complex and it is made of three different steps for cluster generation and ionisation coupling.

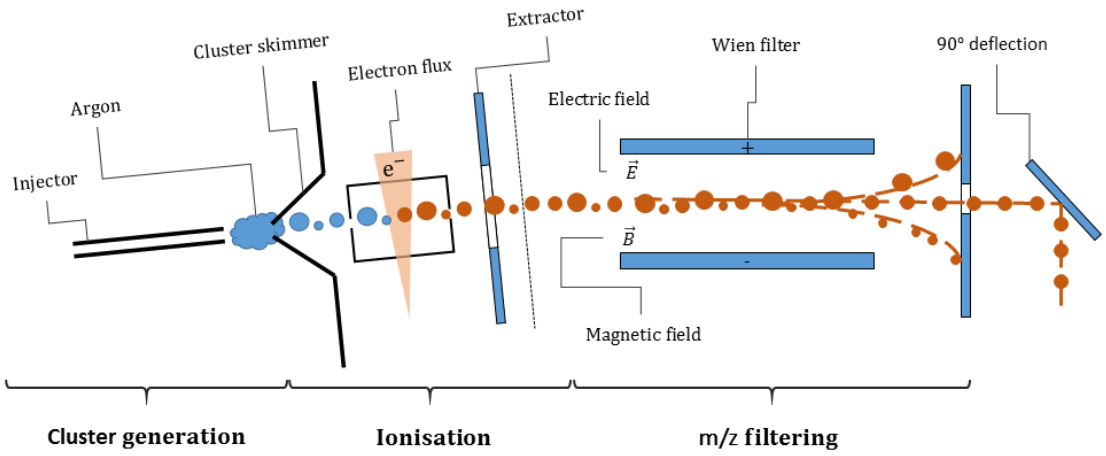

Figure 1.23: Schematic principle of the GCIB gun.

The first part of the gun deals with the cluster formation where an adiabatic expansion of an argon gas flux at high pressure (around 20 bar) takes place. The expansion in vacuum conditions (10^{-3} $mbar$) is supersonic with the subsequent gas cooling. Argon atoms move at a supersonic speed condensing in clusters [10]. A cluster skimmer placed after the cluster formation zone, mechanically selects the argon clusters keeping only the ones moving along the axis of the source rejecting non-condensed atoms. The clusters reach the ionisation chamber based on an electron impact technology described

previously. Since now a cluster ion flux is produced, a mass separation to select, ideally, a single cluster size is needed. Clusters are accelerated by an extractor and soon after the separation is made by a Wien filter. This filter is composed of two plates producing an electric field and several magnetic elements producing a magnetic field orthogonal to the electric one. When these different fields are applied they interact with the charged particle modifying its path. For a given combination of field parameters, only a type of mass/charge (m/z) will pass through the filter without been deviated. The filtering selection is not optimal, as a consequence the resulting flux is composed by a distribution of argon cluster around the chosen size. This operation is followed by a 90° flux deflection to permit the cluster injection in the optic column. This deflection is also used to further optimise the ion beam and pulse it when necessary, as shown in Figure 1.24.

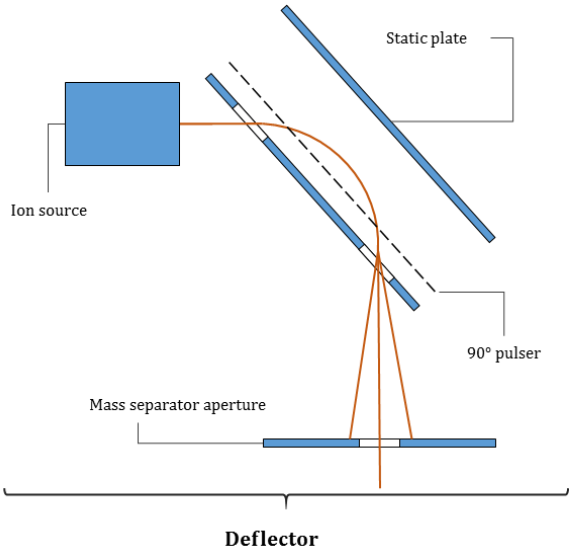

Figure 1.24: Schematic principle of the 90° ion beam deflection of the GCIB gun.

The deflector is composed of a static and a pulsing ("90 degrees pulsed") deflecting plate. The argon cluster beam can be then adapted for the acquisition of spectra (pulsed mode) or depth profiling.

Spectra acquisition: the 90° pulser electric field is alternated to let only the ion clusters near this plate pass through the deflector giving them a chosen pulse. Depending on the initial kinetic energy and m/z ratio, argon clusters will have a different exit angle. This behaviour combined with a mass separator aperture permits the separation of double and triple charged clusters.

Depth profiling: each ion having the same energy follows the same trajectory through the 90° deflector. The m/z ratio of argon clusters is directly linked to their kinetic energy, as a consequence heavier clusters will have more kinetic energy and a longer distance to

travel and vice versa for lighter ions. The consequence is a spatial distribution of argon clusters skimmed by the mass separator aperture.

The ion beam then enters in the optic column shared with a Gallium Focussed Ion Beam (FIB).

1.3.2 ANALYSIS CHAMBER

The analysis chamber consists of a UHV chamber allowing the introduction of the sample holder by a pre-stage chamber called load-lock. Pressure control (vacuum level, oxygen flooding), temperature control (cooling of heating) and sample charge control (electron flooding) can be modified by the user. All the primary ion beams are 45° tilted from the sample normal (Figure 1.25). This configuration is in many cases a good compromise in terms of sputtering [23] and analysis properties. Moreover, it is a very practical solution to accommodate all the ion sources and the ToF analyser chamber placed in the orthogonal plane to the sample. This solution is particular to ToF-SIMS instruments designed by IONTOF.

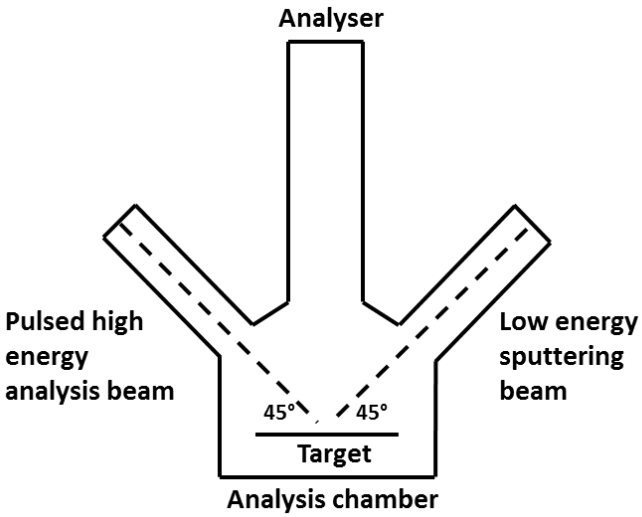

Figure 1.25: Setting of the ToF-SIMS used in this study with the two ion sources tilted of 45° to the normal of the target. A third gas cluster ion gun (GCIB) equips the instrument also inclined at 45° to the front of the analysis chamber upon the load lock chamber (not shown here).

ToF-SIMS Analyser

The time of flight analyser is composed of a UHV tubular shaped chamber with a given length, in the range of a metre. In this chamber, the ions are free to drift and separate as a

function of their mass [113, 114]. A reflectron, consisting of an electrostatic mirror, is placed at the extremity of the flight chamber, opposed to the entering zone of the ions. Its function is to deflect ions and send them towards the detector (Figure 1.26). The use of the reflection has two key benefits:

- To increase the drift length compared to a simple tube, enhancing ion segregation without raising the dimension of the analyser tool,
- To compensate the difference of initial kinetic energy between ions with same mass (ΔE_0). Ions with the same mass but with different ΔE_0 will penetrate at different depths in the electrostatic mirror. Ions with a higher velocity will penetrate deeper in the electrostatic field while slower ions will penetrate less: all the ions will then hit the detector simultaneously.

The detector is a Multi-Channel Plate (MCP) with a dead time of a few nanoseconds.

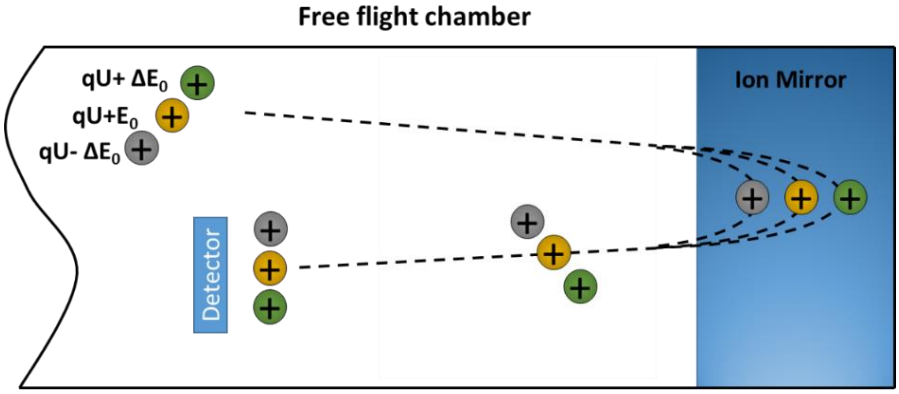

Figure 1.26: the schematic principle of three ions with the same mass but different initial energy.

1.3.3 ToF-SIMS IONTOF ACCESSORIES

Some important accessories used in this work are listed as follow.

A "flood gun" is used to control the surface charge effect by creating a pulsed electron flux at low energy (a few eV). This tool is fundamental for the depth profiling of insulating materials and for the organic material study. In particular, flood gun has shown its usefulness in the charge compensation after caesium primary bombardment to enhance the secondary ion generation.

All the characterised samples had an adapted size of $1x1\ cm^2$ in order to be handled in a particular sample holder called "Backmount". The interest of the sample holder is to host an important number of samples (18 samples) and a high degree of automations. In

the centre of this sample holder a Faraday cup is placed for primary beam current measurements and two grids for alignment and focalisation of primary beams.

1.3.4 LARGE DATA MANAGING BY MULTIVARIATE ANALYSIS (MVA)

In parallel to the development of analysis sources able to reduce sample damaging during bombardment and then increasing the chemical information, the necessity to find tools capable of interpreting the big amount of data collected become fundamental. The high mass resolution and high mass range spectra offered by modern ToF-SIMS instruments carry the ability to obtain rapidly large amounts of data. Simplifying data into usable information is an issue in the analysis of organic materials. Multivariate data analysis techniques have become increasingly common for assisting with the interpretation of complex ToF-SIMS datasets [115]. The term multivariate implies working with multiple variables. These variables can be anything that is measurable. For ToF-SIMS, the variables are typically the integrated peak areas or possibly the intensities of individually analysed mass. It is a statistical procedure that uses an orthogonal transformation to convert a set of observations of possibly correlated variables into a set of linearly uncorrelated variables called principal components. Geometrically, principal component analysis is a type of axis rotation designed to define a new set of axes that capture the major differences between the samples.

PRINCIPAL COMPONENT ANALYSIS (PCA) FOR DATA COMPLEXITY REDUCTION

Principal Component Analysis (PCA) [45, 115, 116] is an unsupervised pattern recognition technique that simplifies SIMS data sets reducing its dimensionality by describing the variance in a data set. PCA compares multiple spectra, each one being composed of multiple peaks, and calculates new variables called principal components (PCs) that describe orthogonal directions of the variance in the data set.

Variance (σ) is defined as the measure of the spread in the data and it is calculated by taking the differences between each number (X) in the set and the mean (μ), squaring the differences (to make them positive) and dividing the sum of the squares by the number of values in the set (N).

$$\sigma^2 = \frac{\sum(X - \mu)^2}{N}$$

PCA needs to know how each variable varies compared to all of the other variables. For this reason, the covariance matrix is needed. PCA determines sequential orthogonal axes that capture the greatest directions of variance within the data set. The results from PCA are scores and loadings [117]. The scores are the projection of the spectra onto each PC and show the relationship between the spectra in the data set, with each point on a scores plot representing one ToF-SIMS spectrum. The loadings display the relationship between the PCs and the peaks in the ToF-SIMS data set. Combining scores and loadings plots, one can determine which peaks are related to which sample type. Graphically, this is done by examining the location of the spectra and peaks in the scores and loadings plot for a given principal component (more information about PCA and result interpretation can be found in the works of National Institute for Biomedical Imaging and Bioengineering[2]). Confidence limits are normally integrated into the scores plot ant represent the confidence mark for each sample group indicating the data dispersion in a range of 95%. PCA analysis is already successfully applied for the quantification of polymer blends characterised by varying ending groups in the case of formaldehyde resins, polystyrene and aliphatic polyesters [118].

1.4 Conclusion

In this first chapter, the versatility of ToF-SIMS to characterise a large variety of materials has been shown. Moreover, thanks to the introduction of new ion sources, this characterisation technique has already been successfully applied for the characterisation of low density and soft materials largely used in micro and nanotechnologies. However, ionisation and sputtering phenomena have not been fully considered. At present, a large research has been performed on solid dense materials that in some cases it loses its validity while moving towards low density and soft materials characterisation. Aspects such as ion/matter interactions, target melting, nature of generated secondary ion information have been observed to change as a function of the material density. This work evaluates these types of aspects by using low energy and monoatomic new sources on low density materials and interpreting the results. The generated secondary ion spectra are also evaluated and explored as the chemical information produced is shown to become the more and more characteristic of a given material in parallel with the decrease of damage produced by primary sources. In addition, the more the detected masses increase

in weight the more the complexity of the chemical information increases. Therefore, to solve the complexity of the collected chemical information, chemometrics (PCA) is considered here as a reliable tool, applying statistical mathematical methods to decrease the degree of data system complexity by the identification and the arrangement of the principal chemical detected modifications.

---

[1] http://www.telko.com/files/images/telko/ru/basf/termostabilizator/irganox_1010_tds.pdf (February 2016)

[2] http://www.nb.uw.edu/mvsa/mvsa-tutorials (January 2016)

2 IMPACT OF POROUS STATE MATTER ON THE DETECTED SIMS INFORMATION: POROUS SILICON

This chapter concerns the application of ToF-SIMS technique for the characterisation of porous silicon. The porosities introduced during the fabrication process decreases the density of the material and data such as sputter rate, surface morphology, ionisation and depth profiling are compared to these of dense silicon materials.

2.1 INTRODUCTION TO POROUS SILICON (P-SI)

2.1.1 HISTORICAL REMARKS AND CONTEXT

Porous silicon was first discovered in 1956 during electropolishing experiments [79]. Uhlir polished silicon wafers with an electrolyte containing hydrofluoric acid (HF) finding that, under appropriate conditions, the solution was not dissolving uniformly the silicon, forming holes propagating in the <100> set of crystalline directions. In the ‘70s, thanks to its high surface area, this material gained in interest as a platform for inorganic and organic compounds decomposition [119, 120] in order to generate a thick oxide layer. At the same period it was applied in capacitive-based chemical sensors [121]. In the ‘90s, p-Si was discovered to have luminance properties [122], from now on the interest of researchers to this material constantly grew as well as scientific publications. Nowadays p-Si is largely used in in sensors and capacitors applications [123-128].

APPLICATIONS

There are a lot of different applications at present for p-silicon depending on their properties (Table 2.1) and pore dimensions [129].

Table 2.1: Potential application areas of porous silicon from [130, 131]

Application area	Role of porous silicon	Key property
Optoelectronics	LED Waveguide Field emitter Optical memory	Efficient electroluminescence Tunability of refractive index Hot carrier emission Non-linear properties
Micro-optics	Fabry-Pérot Filters Photonic band gap structures All-optical switching	Refractive index modulation Regular macropore array Highly non-linear properties
Energy conversion	Antireflection coatings Photoelectrochemical cells	Low refractive index Photocorrosion cells
Environmental monitoring	Gas sensing [132]	Ambient sensitive properties
Microelectronics	Capacitors [128, 133] Insulator layer [134] Low-k material Radio-frequency devices [135]	High specific surface area High resistance Electrical properties
Wafer technology	Buffer layer in heteroepitaxy SOI wafers	Variable lattice parameter High etching selectivity
Micromachining	Thick sacrificial layer	Highly controllable etching
Biotechnology	Tissue bonding [136] Biosensor [137]	Tunable chemical reactivity Enzyme immobilization

In micro technologies, for example, it is shown that while varying the functionalization and the fulfilling of pores with active agents, different application of p-Si can be obtained. Some examples can be found in the works of Boarino *et al.* [132] concerning the functionalization of p-Si surface with $-ONO$ groups to increase the yield of NO_2 gas detection (in Figure 2.1 dynamic response of p-Si as a function of time and gas concentration is shown). Another significant example is the deposition on pore surface of dopants such as erbium performed by Mula *et al* [138] to increase the light emission of p-Si. Portable electrochemical capacitors and super capacitors have been produced by introducing porous silicon as support for electrolytes by combining doping and metallization processes on pore walls [128] or by depositing an ultra-thin graphene

coating that simultaneously passives surface charge traps and provides an ideal electrochemical interface between electrode and electrolyte [133]. In the field of microelectronics, p-silicon is also used as insulator layer and separator between active devices (transistors and interconnections) thanks to its dielectric and mechanical properties [134].

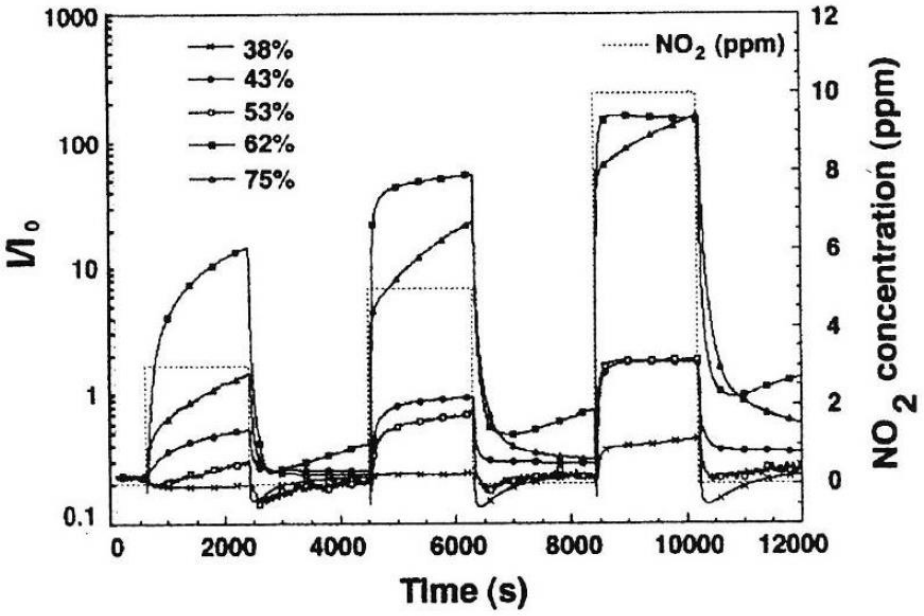

Figure 2.1: NO_2 sensor dynamic p-Si response [132]

Promising applications are in the fabrication of solar cells to reduce costs [139]. In this case, p-Si is used as a sacrificial layer for the deposition of buried contacts in silicon. Applications in tissue engineering are also investigated thanks to biocompatibility [136, 140], biodegradability and photo-luminescent properties. Drug encapsulating and delivery applications are also possible thanks to its high loading capacity, controllable surface chemistry and structure, and controlled release properties [137] (Figure 2.2).

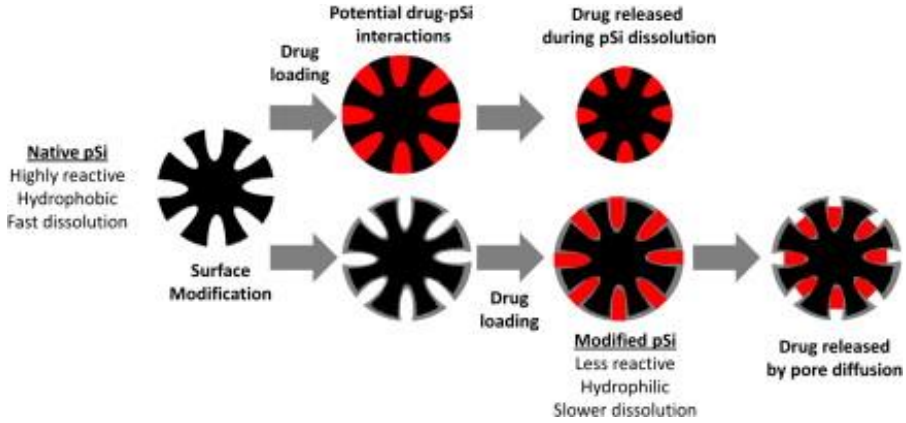

Figure 2.2: Porous silicon design as high potential drug delivery vehicle (image from [137])

FABRICATION

Among all the advantageous properties of porous silicon, its simple and easy preparation by electrochemical dissolution of silicon wafers in solutions based on hydrofluoric acid (HF) [141] is the predominant. The surface of a silicon wafer, wired on the back, is immerged in a solution containing hydrofluoric acid (HF). After applying a voltage, between the wafer backside contact and an electrode in the HF solution, pore growth starts [1], see schematics in Figure 2.3.

Constant direct current (DC) source is usually used to ensure a constant concentration of electrolyte at the cathode tip for a better control of the corrosion rate. In this field, it is generally accepted that semiconductor carriers known as holes are important for the initial oxidation steps during pore formation favoured in *p*-doped (i.e. boron) silicon. Hence, for n-type (i.e. arsenic and antimony) Si, an appreciable amount of anodisation may only take place under light illumination [142, 143], high fields, etc. The magnitude of illumination is dependent on the doping level of the native wafer. The following equation provides a plausible surface chemical reaction that occurs during silicon anodisation:

$$Si + 6HF \rightarrow H_2SiF_6 + H_2 + 2H^+ + 2e^-$$

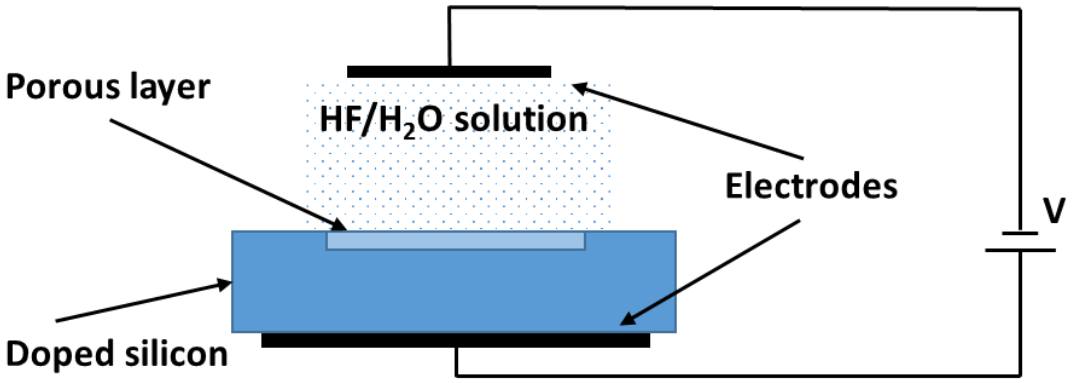

Figure 2.3: Schematic diagram of the porous silicon anodisation circuit.

SURFACE CHEMICAL COMPOSITION

The zone with the highest chemical interest of p-Si is the surface corresponding to an extension of more than 500 m^2/cm^3. Surface chemical composition can be varied and its chemical composition affects enormously optical, electrical, and detecting properties. Natural aging, intentional oxidation and intentional surface modifications are the main causes that induce chemical changings. To verify, control and improve porous silicon

properties, an accurate knowledge of surface chemical composition and distribution of chemical species in depth is logically needed. The characterisation field disposes of a limited number of techniques providing this answer. By now it is possible to determinate the elementary surface composition of p-Si by the analysis of chemical species functionalising the pore surface.

However, sometimes there is an aspect that is not fully taken into account that is the influence of the analysis techniques on the results.

Several techniques have been applied in bibliography to characterise the interesting features that arise from the anodisation process of silicon wafers. These results allow an easier identification of characteristic elements and species detectable also by SIMS technique in this work.

The original impurity which is always found in p-Si layers is hydrogen. Infrared absorption (IR) experiments have shown the presence of $Si - H_x$ groups (x = 1; 2; 3) on the internal p-Si surface during the etching process. After formation and drying, the $Si - H_x$ groups are still present on the inner surface for weeks and even for months, as it has been demonstrated using IR absorption [82].

The second original impurity found in p-Si is fluorine (F) [144]. The content of fluorine decreases with time. It has been proposed that SiF bonds are progressively replaced by $Si - OH$ bonds through hydrolysis reaction with water vapour in air.

Oxygen is the most important non-original impurity and is normally adsorbed in a few minutes after drying in ambient air. IR spectrum performed a few hours after anodisation on a p-Si layer has shown the presence of $Si - O - Si$ group [82]. It is shown that natural oxidation takes place in a relatively long period of time.

Other impurities are usually incorporated after the anodisation process as carbon present in the atmosphere [145]. The carbon comes from hydrocarbon molecules present in the ambient air and often also in the residual gas or vacuum pump oil [146] in the analysis chambers used for SIMS, XPS, etc…

Doping elements such as boron or antimony are present in traces in p-Si, limiting the application of classical techniques such as infra-red for a full knowledge of the chemical composition. Regarding trace analysis, electron tomography has been successfully applied on mesoporous silicon [147] offering a robust method in terms of 3D structure reconstruction and surface doping element localisation.

2.1.2 STRATEGIES

Referring to the wide range of p-Si applications, the use of secondary ion mass spectrometry for a fine chemical characterisation is investigated. Pore size and distribution, surface functionalization and volume fulfilling are parameters usually modified with the intention to vary the applications of this versatile material. As explained in section 1.2.1, the interaction of an energetic ion beam, such as the one used in SIMS analysis, is expected to generate serious modifications on the material, directly affecting the final chemical information expected to describe its depth chemical composition.

In order to try to evidence these phenomena, a methodical analysis is then carried out on mesoporous silicon samples with an overall variable porosity (40% to 70%) and a constant pore diameter ($\phi = 20\ nm$). This choice was made in order to limit the sample set variations only around one variable and in reason of production constraints. The effect of different sputtering ions on these samples has been made considering three primary ions: caesium, xenon and oxygen.

Sputtering sources are chosen because of their specific properties: caesium (132.9 g/mol) and xenon (131.29 g/mol) have a very similar atomic weigh however caesium is extremely reactive with the target (section 1.1.3.1) while xenon as a noble gas is particularly inert. The comparison between these two ion beams is expected to reveal ionisation distinctive phenomena related to caesium bombardment. This phenomenon is energy dependent as shown by Mine N. *et al.* (section 1.1.3.1) as it is linked to the amount of caesium deposited on surface during sputtering and also linked to the overall porosity. In addition, it is important to remind that caesium has the particularity to diffuse to surface and create agglomerates on flat surfaces [148]. This particular behaviour can be characterised in porous samples by a diffusion of caesium through the vertical pores with a migration deep into the pores. Oxygen ions too are an extremely reactive as described in section 1.1.3.1 and it is potentially largely instructive for the comprehension of ionisation phenomena in porous samples depending on the applied sputtering energy. Moreover, oxygen can oxidise sample inducing a change in the chemistry of the sample such as the formation of silicon dioxide on surface also linked to the chosen sputtering energy. However, because no in-depth diffusion and accumulation effects take place, acquired depth profiles are potentially very different compared to caesium. Moreover, the flooding with an additional oxygen flux in the analysis chamber is supposed to induce an ulterior matter oxidation with a direct effect on the generated secondary ion information.

In this work, a phenomenological approach is followed through the observations of variations induced by sputter settings at different sputtering energies (0.5 to 2 keV) on the sputter rate of each sample. These observations are completed by scanning electron microscopy of SIMS craters to appreciate and evaluate the morphological modifications occurring during sputtering as documented for nanoparticles in section 1.2.1 such as surface melting.

Only the effect of sputtering beam is studied, as morphological modification induced by analysis gun (bismuth) are considered less damaging due to the low currents involved and applied for short period of times. It was indeed estimated that a sputter setting of 500 eV at 40 nA applied on a surface of 300x300 μm^2 (lowest used sputter energy) has an impact on surface in terms of current doses 1000 times higher compared to the used analysis setting of 15 keV at ~1.7 pA on a surface of 100x100 μm^2.

In order to monitor and at the same time quantify the effect of primary impacting ions on the generated secondary ion information, values such as sputter rate, pore and bulk ionisations of characteristic elements were extrapolated and ionisation ratios calculated.

Interpretations were supported by simulations with SRIM software (section 2.2.4) to evaluate the ion stopping range of primary ions in solids targets.

2.2 EXPERIMENTAL

2.2.1 POROUS SILICON SAMPLES AND DENSE REFERENCE

In Figure 2.4-a classical porous structure of a sample similar to the ones studied in this work is presented.. Voids (black spots - pores) have a dendritic structure and each pore is separated by the ones besides it by thin silicon membranes. These silicon membranes are connected to solid pillars that keep the solid structure of sample, preventing it to collapse. Samples were produced at CEA Grenoble.

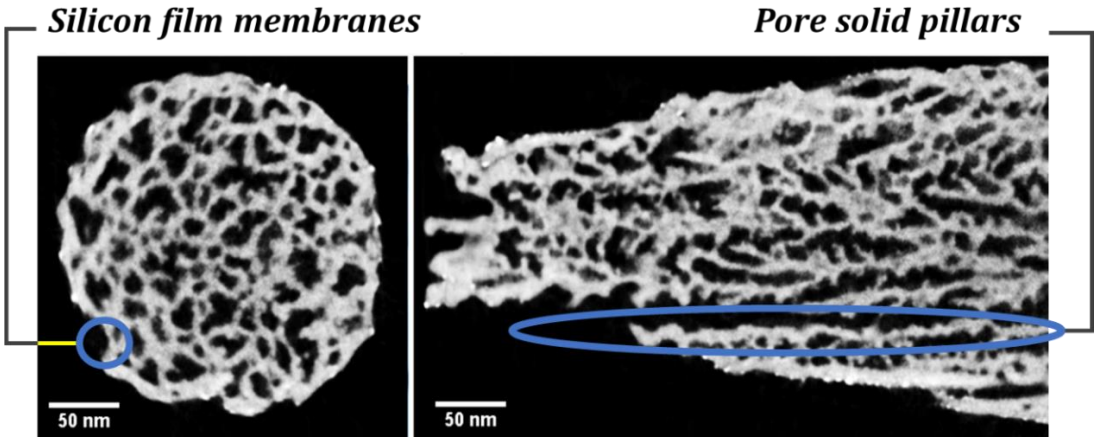

Figure 2.4: Transmission electron microscopy tomography of a 10 nm pore size porous silicon sample showing pores (black regions) and silicon (grey region). Left image a perpendicular section to pores and in the right image a parallel section [147].

The porisification process was performed on boron doped silicon wafers creating porous layers around 200 nm thick. Four different wafers were prepared with a different overall porosity between 40% and 70% (Table 2.2). To reduce natural oxidation, samples were stored in dark conditions but an uniform aging of several weeks was applied to all samples. In order to reduce even more the impact of aging on samples, all the analysis were performed in a unique characterisation session.

Porosity, defined as the void fraction in the p-Si layer (Eq.2-1) can be determined by weight measurements. Weighing the wafer before (m_1) and after (m_2) anodisation, the porosity is given by the following equation:

$$P(\%) = \frac{(m_1 - m_2)}{\rho\, S\, t} \qquad \textit{Eq.2-1}$$

ρ = silicon density, S = wafer surface, t = thickness of porous layer

The pore layer thickness and pore size were measured by cross-section SEM observations and results are reported in Table 2.2.

Table 2.2: Set of porous silicon samples studied.

Overall porosity*	Pore Size (nm)	Thickness (nm)
$(40 \pm 3.4)\%$	20 ± 3	200 ± 10
$(50 \pm 2.7)\%$	15 ± 5	200 ± 3
$(60 \pm 2.3)\%$	20 ± 3	186 ± 3
$(70 \pm 2.0)\%$	25 ± 8	193 ± 3

*measured by gravimetric measurements (precision weighting balance with an absolute error of $1x10^{-5}\ g$)

Figure 2.5 presents the cross-section view of the 60% p-Si layer is presented and the porous and dense layer can be clearly distinguished. In particular, the vertical columnar shape of the porous layer is associated with a dendritic structure and all the columnar pores are opened through the surface. Tilting sample is possible to appreciate the surface roughness.

In addition to these row material samples, a reference material grown by epitaxy composed by "boron delta" layers (for more details [149]) in a silicon was used to determine the sputter rate in dense silicon (Figure 2.5-b). This sample is extremely useful because the sputter rate is directly calculated on the sample without the need of external characterisation, in particular for craters sputtered at low energies. It was also used to determine the ionisation of characteristic bulk species (silicon and its isotopes) compared to porous layers depending on the applied sputtering protocol.

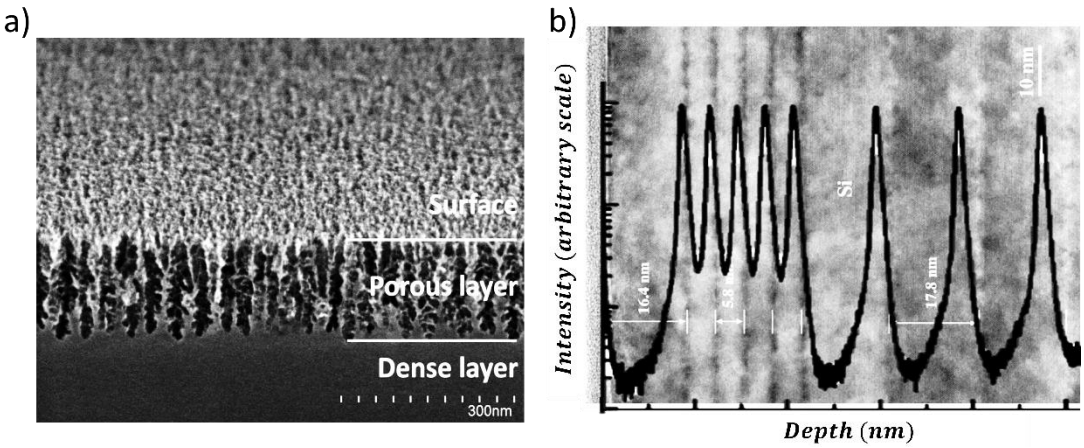

Figure 2.5: a) 40° tilted SEM image of 60% p-Si sample. The image is acquired by secondary electrons emitted by a 30 keV primary field effect cold source at 15 nA current on a Hitachi S5500 instrument. b) in-depth concentration of boron in a "boron delta" layer superposed to a TEM cross-section observation of the sample.

2.2.2 ToF-SIMS SETTINGS

Three distinct sources were used to sputter samples as explained in "strategies" section:

- Monoatomic caesium (Cs^+)
- Monoatomic xenon (Xe^+)
- Oxygen (O_2^+)

accelerated at three different energies 500 eV, 1 keV and 2 keV on a common raster of 300x300 μm^2.

As presented in chapter 1, ToF-SIMS for depth profiling is performed in "dual beam mode": sputtering guns are coupled to an analysis gun for spectra acquisition between the sputtering cycles. In this chapter, the analysis ions used are monoatomic bismuth ions accelerated at 15 keV with a measured current of ~1.7 pA, rastered over 100x100 μm^2.

In Table 2.3 sputtering settings used and currents are listed. The porous morphology of analysed samples induces an electrical property variation. In particular, the presence of incorporated voids and silicon dioxide on pore surface transform the semi-conductive silicon into a dielectric. "Non-interlaced" mode (section 1.1.1.2) is applied during sputtering because a longer pause time between sputtering and analysis is needed to properly compensate charges and to assure matter ionisation (section 1.1.3.1). The sputtering energies are chosen among the existing settings normally available on the ToF-SIMS instrument used.

Table 2.3: Table reporting the primary sputtering ion types, acceleration energy and current used for in-depth profiling of p-Si samples.

Source	Energy	Current (nA)
Cs^+	500 eV	40
	1 keV	90
	2 keV	134
Xe^+	500 eV	50
	1 keV	155
	2 keV	493
O_2^+	500 eV	75
	1 keV	200
	2 keV	460

In the particular case of oxygen source, characterisations were performed with and without the presence of an oxidising flooding of O_2 in the vacuum main chamber. The oxygen flooding was obtained by setting the main chamber vacuum to ~$3x10^{-6}$ $mbar$.

2.2.3 SCANNING ELECTRON MICROSCOPY SETTINGS

Scanning electron microscopy (SEM) was used for sample observations and size measurements (porous diameter and layer thicknesses). SEM allows the acquisition of high resolved images with a lateral resolution lower than 1 nm. This technique uses a primary electron source accelerated in a range between 0.35 to 30 kV. The electron beam while interacting with the sample induces the emission of different signals. Among these signals, low kinetic energy electrons can be used for imaging purposes. For this study, an Hitachi S5500 was used with an acceleration energy of 30 kV and a current of 15 μA. Samples were analysed in a short time after SIMS depth profiling (less than 12 hours), samples being stored during this period in glove box system with a controlled inert N_2 atmosphere.

2.2.4 THE STOPPING AND RANGE OF IONS IN MATTER (SRIM)

Stopping and Range of Ions in Matter (SRIM) [150] is a group of computer programs which calculate interactions of ions with matter; the core of SRIM is a program TRansport of Ions in Matter (TRIM). SRIM is based on a Monte Carlo simulation method, namely the binary collision approximation with a random selection of the impact parameter of the next colliding ion. As the input parameters, it needs the ion type and energy (in the range 10 eV to 2 GeV), impacting angle (0° to 90°) and the material of one or several target layers.

As the output, it lists or plots:

- the three-dimensional distribution of the ions in the solid and its parameters, such as penetration depth, its spread along the ion beam (called straggle) and perpendicular to it
- sputtering rate, ionisation, and phonon production in the target material.

However, it does not take account of the crystal structure nor dynamic composition changes in the material that severely limits its usefulness in some cases.

Other approximations of the program include:

- binary collision (i.e. the influence of neighbouring atoms is neglected)
- the material is fully dense and amorphous
- thermodynamic calculations and the consequent matter state variations are also neglected.

- the system is layered, i.e. simulation of materials with composition differences in 2D or 3D is not possible

Despite all these limitations and approximations, SRIM has been used in this study to obtain a quantification of the primary ion stopping range used to characterise porous materials. To do so, the target is approximated to a dense silicon layer impacted by a 45° tilted primary ion beam. The simulation algorithm chosen was "surface sputtering/monolayer collision", it is optimised for the calculation of the primary ion stopping range, its spread and detailed atom collisions as shown in Figure 2.6.

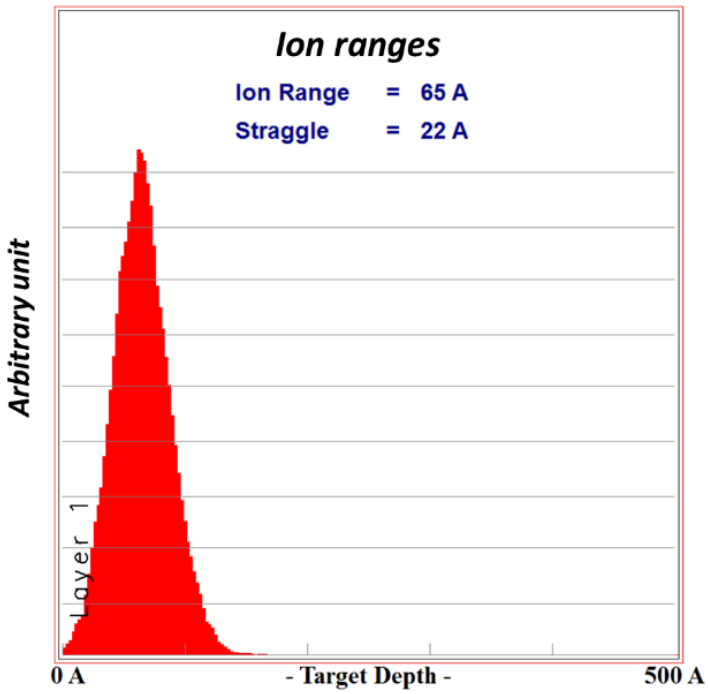

Figure 2.6: In-depth distribution range diagram of caesium ions accelerated at 500 eV on a 50 nm thick silicon target tilted at 45° with the corresponding stopping "ion range" and distribution spread ("straggle").

These results are far from being descriptive of a mesoporous silicon system such as the one studied in this work. However, results are considered extremely useful for the comprehension of sputtering phenomena such as primary ion implantation and tracking in the porous matter and hints about the size dimensions of the ion/matter interactions.

2.3 PHENOMENOLOGICAL APPROACH: PHYSICAL AND MORPHOLOGICAL STUDY OF SURFACE MORPHOLOGICAL VARIATIONS AND EFFECTS ON THE SPUTTERING RATE

The first aspect being evaluated is the observation of the physical aspects deriving from ion bombardment on the surface of samples. Sputter rate is a fundamental parameter for the determination of the efficiency of sputtering conditions. The variation of the overall porosity is tightly linked to the variation of matter density. As a consequence, the efficiency of primary ion sources bombarding samples can be different. Moreover, the comparison with a solid silicon reference ("boron delta layer") material will clarify the role of the overall porosity in the efficiency of sputtering process. As speculated, melting can also occur during ion bombardment further impacting sputtering rate. The results will be then associated with a morphological study by SEM observations designed to observe the bottom crater surface aspect after stopping the sputtering process in the porous layer.

2.3.1 SPUTTER RATE VARIATIONS AS FUNCTION OF MORPHOLOGICAL MODIFICATIONS AND POROUS MATERIAL PROPERTIES

The sputter rate ($SR_{porous\ material}$) were calculated using the thicknesses of the porous layers for each sample measured by SEM as a function of the time spent to sputter the entire porous layer. Sputter time was calculated on the silicon (^{28}Si) or on one of its isotope with non-saturated intensity. This choice derives from an easiness to identify interface using silicon ions and because it correctly represents the behaviour of the entire emitted ions. Once the sputtering reach the dense substrate a sharp decrease in Si signal is observed. Logically, there rates change as function of the energy (E_i) and beam used. Normalisation was performed (Eq.2-2) dividing the $SR_{porous\ material}$ by the measured sputter rate of bulk silicon ($SR_{bulk\ material}$) obtained in the same experimental conditions (E_i).

$$SR_R = \left(\frac{SR_{porous\ material}}{SR_{bulk\ material}}\right)_{E_i} \qquad Eq.2\text{-}2$$

Before going further in the interpretation of the obtained results a comparison between sputter rates of dense silicon is proposed as a function of energy and ion beam employed (Figure 2.7-a). As expected in all cases the SR increases as a function of the acceleration energy of primary ions. The sputter rates at 500 eV are comparable for all the sputter

beams. However, for higher sputtering energies, a discrepancy between trends is observed. In particular, high SR correspond to xenon source as it is characterised by important beam currents. A linear trend characterises the oxygen behaviour without a particular distinction depending on the presence of the oxygen flooding. Caesium sputter rate is low at 2 keV sputtering energy: the reason is due to lower ion flux values. In fact, xenon and oxygen currents are more than 3 times higher compared to caesium at 2 keV (see exact values in Table 2.3).

In order to exclude from these results the contribution of the primary ion current, the experimental sputter yield is plotted as a function of the sputtering energy. The experimental sputter yield (S_y) represents the number of target atoms composing a volume (V_{target}) sputtered per impacting primary ions characterised by a measured current (I) during a measured time (t). The V_{target} is defined as the rastered area (R^2) multiplied by the crater depth (th).

$$S_y = \frac{\rho_{target} R^2 * th}{\frac{I * t}{q}}$$

where ρ_{target} is the target atomic density and q the electron charge expressed in Coulomb. The SR corresponds to a depth (th) sputtered during a time (t) and the previous equation can be then written as follows:

$$S_y = \frac{q * \rho_{target} * R^2}{I} * SR$$

In Figure 2.7-b, it is observed that the sputter yields of caesium and xenon on the dense silicon target, in the considered energy range, are similar because of the reduced difference in atomic mass. Contrary, oxygen S_y appear lower being its atomic weight ~8 times lighter compared to Cs and Xe ions. In presence of oxygen flooding, the sputter yield calculation is performed considering silicon dioxide atomic density because the flooding is supposed to oxidise the target. The 500 eV oxygen sputtering in presence of oxygen flooding is observed to be lower compared to the values in absence of flooding. This discrepancy is due to the swelling phenomenon deriving from the silicon oxidation having as consequence the decrease of the sputter yield value.

Measured sputter yield are in the same range of values calculated by Monte Carlo simulations for a given ion-garget combination (see Yamamura *et al.* [151]) and tabulated in IONTOF software as a function of the impacting angle.

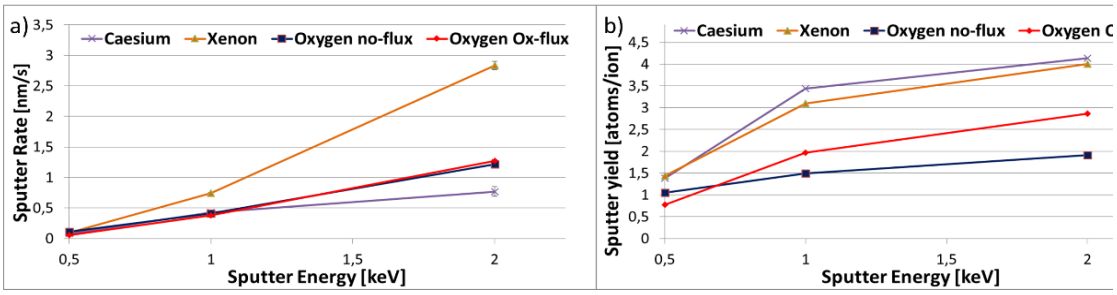

Figure 2.7: a) Sputter rate and b) sputter yield plots of dense silicon for applied sputtering setting.

Considering the SR (y) as a function of the materials density (x between 0 and 1) without considering secondary effects such as matter melting the "theoretical" trend is supposed to be described by an hyperbole as follows:

$$y = \frac{1}{1 - x}$$

In absence of porosity ($x = 0$) the sputtering rate assumes an unitary value while for 100% porosity the SR grows asymptotically as shown in Figure 2.8

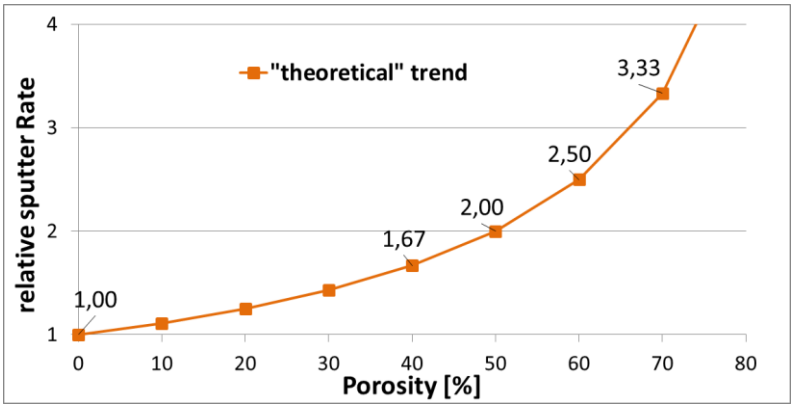

Figure 2.8: "Theoretical" sputter rate trend of a material with an increasing overall porosity rate.

These values will be used in the following sessions to compare the theoretical sputter rate trend with the values tabulated experimentally on the analysed sample set.

CAESIUM SPUTTERING SOURCE

In Figure 2.9-a relative sputter rates are reported for the used caesium settings. At first, SR values at 40% of porosity are very similar to the sputter rate of dense silicon indicating that, for this overall porosity, the sample has a sputter behaviour comparable to a dense material. Besides, for each of the three sputtering energies, an increase of the sputter rate

is observed as a function of the porosity. In particular, for porosity rates higher than 50% a discrepancy between 2 keV and lower energies is observed suggesting that sputtering is more efficient for highly porous samples (higher than 50%). Comparing results to the "theoretical" sputter rate trend calculated previously it can be observed that experimental data present inferior values. This observation is not valid for the 2 keV sputtering setting of samples above 50% porosity. It is reasonable to think that two distinct regimes of sputtering take place.

Plotting SR_R as a function of the sputter energy (Figure 2.9-b) the slope discrepancy between 2 keV and lower energies becomes clearer. A positive slope after 1 keV sputtering is observed for samples with an overall porosity above 50%. For porosity values below 50% a stabilisation of SR is observed indicating a less effective sputtering at high energies compared to more porous samples. It can be imagined that for high porosities the quantity of solid matter separating pores is low and the efficiency of sputtering is higher. In this case, the thin membranes connecting solid pillars can be preferentially sputtered increasing sputtering efficiency.

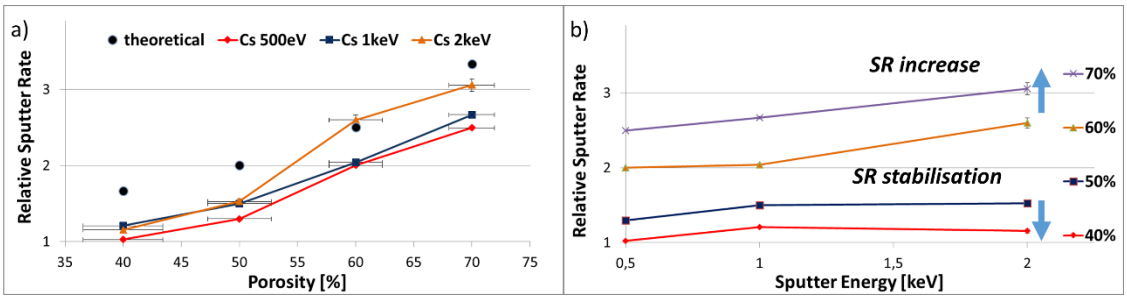

Figure 2.9: Sputter rate plot vs. a) overall porosity and b) sputtering energies for porous samples sputtered by monoatomic caesium source at 500 eV, 1 keV and 2keV.

Calculations by SRIM modelling have been performed on dense silicon target. In particular, the implantation depth was assessed. In Table 2.4-a ion penetration range for each sputter energy is reported with the corresponding standard deviation associated. Depth penetration increases with the increase of the acceleration energy and data dispersion increase as a consequence. These values are compared to the interdistances between columnar porosities for each sample. To measure pore interdistances, SEM cross-section observations of the porous layers were acquired and the mean of thicknesses of solid matter separating pores are reported in Table 2.4-b. Comparing the two tables, it can be observed that for energies higher than 1 keV, implantation depth is in the range of the interdistance between pores for overall porosities above 50%. In this case, the

impacting ion has a high possibility to cross the pore walls from one side to the other generating multiple sputtering site. As a consequence, the sputtering efficiency is higher.

Table 2.4: a) Table reporting the penetration depth of accelerated caesium ions through a silicon dense target by TRIM modelling (tilted by 45° to reproduce SIMS design) b) table reporting the mean of the interdistances between adjacent pores measured by SEM observations of porous layers cross sections.

Energy	***Stopping range***
500 eV	$2.6 \pm 0.8\ nm$
1 keV	$3.4 \pm 1.1\ nm$
2 keV	$4.4 \pm 1.4\ nm$

Porosity	***Interdistance***
40%	$18 \pm 3\ nm$
50%	$15 \pm 3\ nm$
60%	$10 \pm 3\ nm$
70%	$7 \pm 3\ nm$

In Figure 2.10 a schematic representation of the ion likely path through a pore thin wall is schematised. It can be supposed that in this particular case multiple sputter sites are generated: one at the impact site zone and the others when the ion crosses the pore wall. It can be reasonably assumed that at an energy above 1 keV and for porosity over 50% multiple sputtering sites can be generated per impacting ion.

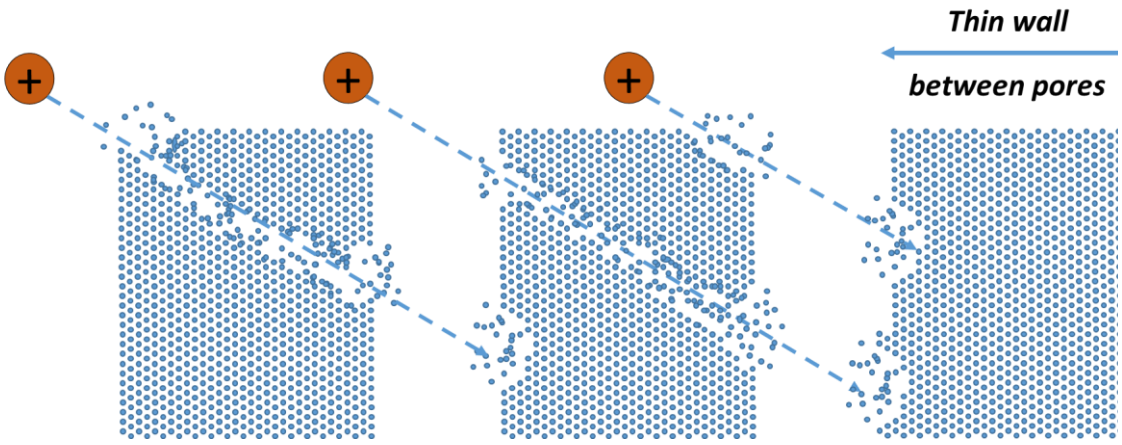

Figure 2.10: Schematic representation of an energetic ion passing through a thin barrier (proportions are not respected) generating multiple sputtering sites per impact.

XENON SPUTTERING SOURCE

The same type of study is performed on p-Si samples using the xenon as sputtering source (Figure 2.11). In Figure 2.11-a, the relative sputter rates for each sputter setting are plotted as a function of the overall porosity and a linear increment is observed for every sputtering energies. In additions, 500 eV and 1 keV curves perfectly overlap the "theoretical" trend, while samples sputtered at 2 keV describe a faster sputtering regime. The trend discrepancy between 2 keV and the other energies is comparable to the one observed in caesium sputtering with a threshold at 50% but with higher efficiencies probably due to the higher sputtering fluences that have an enhanced destructive effect on porous matter.

In Figure 2.11-b, all trends show an increase in sputter rate after 1 keV for samples with a porosity above 50% as observed for caesium.

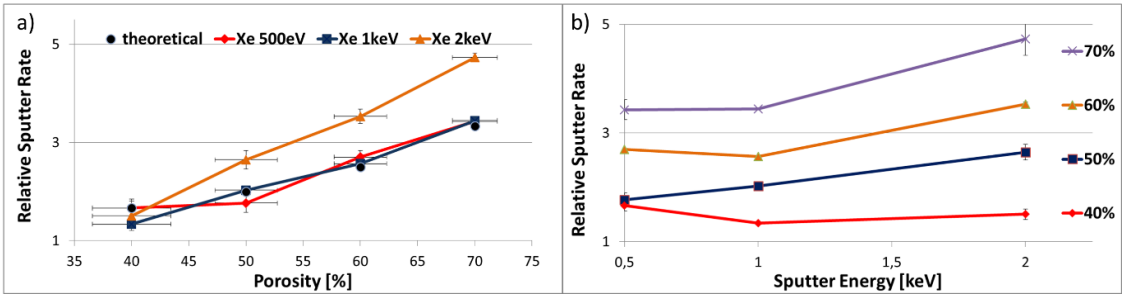

Figure 2.11: Sputter rate plot vs. a) overall porosity and b) sputtering energies for porous samples sputtered by monoatomic xenon source at 500 eV, 1 keV and 2keV.

TRIM simulations were performed substituting caesium to xenon as impacting ion (results not presented here). However, no differences in stopping range and primary ion distribution in-depth were observed, concluding that the observed data trends cannot be fully explained by the collision cascade. Therefore, the ion/matter interaction are different between a reactive species such as caesium and a neutral one such as xenon and are able to produce specific behaviours under ionic bombardment.

OXYGEN SPUTTERING SOURCE

In Figure 2.12 the relative sputter rate is calculated for oxygen O_2^+ sputtering in presence or in absence of a supplementary oxygen flooding. In Figure 2.12-a-b an increase of the sputtering rate proportional to the overall porosity is observed and no differences in data trend are produced by the additional oxygen flooding. This result is similar to what observed for caesium and xenon sputtering. In this case, though primary

ion currents are similar to xenon, sputter rate results are comparable to caesium because of the significantly lower sputter yield of O_2^+ compared to the other two sputtering species. The curves trend is also comparable to what observed with caesium, i.e. a strong increase of SR above 50% of porosity. As observed for caesium results, SR values are under the theoretical values especially for data at 50% and 70% porosity.

In Figure 2.12-c-d sputter rates are plotted as a function of the sputtering energy. In this case, keeping constant overall porosity, a decrease of sputter rate for higher sputter energies (1-2 keV) is observed for both cases with and without additional O_2 flooding. In particular, the sputter rates decrease between 500 eV sputtering and 1 keV and newly increase at 2 keV. This behaviour is distinctive of this source and is not comparable to caesium and xenon sputter rate data. Moreover, a clear vertical discrepancy between samples below and above 50% porosity is observed. In particular, SR of samples with an overall porosity lower than 50% appear to be in the range to dense material sputter rate values. However, above 50% porosity, sputter rates are clearly distinctive at every energy.

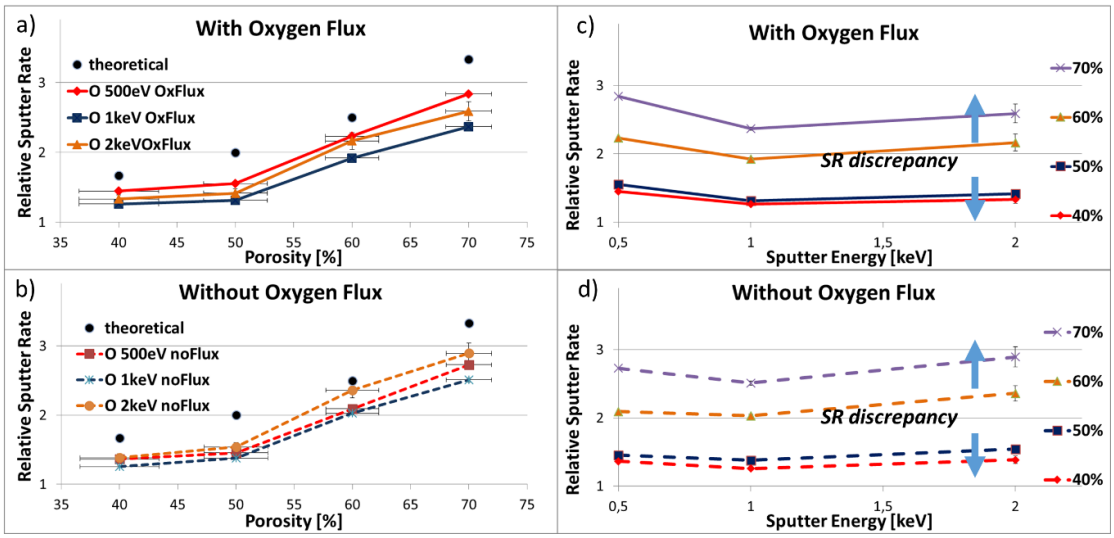

Figure 2.12: Sputter rate plot vs. a-b) overall porosity and c-d) sputter energies for porous samples sputtered by oxygen source (O_2^+) at 500 eV, 1 keV and 2keV and a) and c) correspond to data obtained in presence of an additional oxygen flooding

In order to explain the decreasing SR trend between 500 eV and 1 keV, the starting hypothesis is that this difference is linked to the composition of the matter exposed to primary ion beam.

As oxygen has the particularity to oxidise silicon, it can be expected that silicon dioxide is produced during sputtering. At the same time, as explained in section 2.1.2, oxygen is already incorporated in the porous material as an oxidation take place as soon

as the sample is exposed to the natural atmosphere. During sputtering, additional oxygen is implanted in the oxidised layer enriching it in oxygen. The system can be simplified to a silicon dioxide surface sputtered with an oxygen primary source (Figure 2.13-b). To simulate a lower oxygen content, a silicon reference surface by exposed to an oxygen flooding while sputtering the surface (Figure 2.13-a). In this way, two distinct sputtering behaviours can be induced:

- high oxygen content surface characteristic of a low energy sputtered samples
- low oxygen content sample characteristics of high energy sputter settings

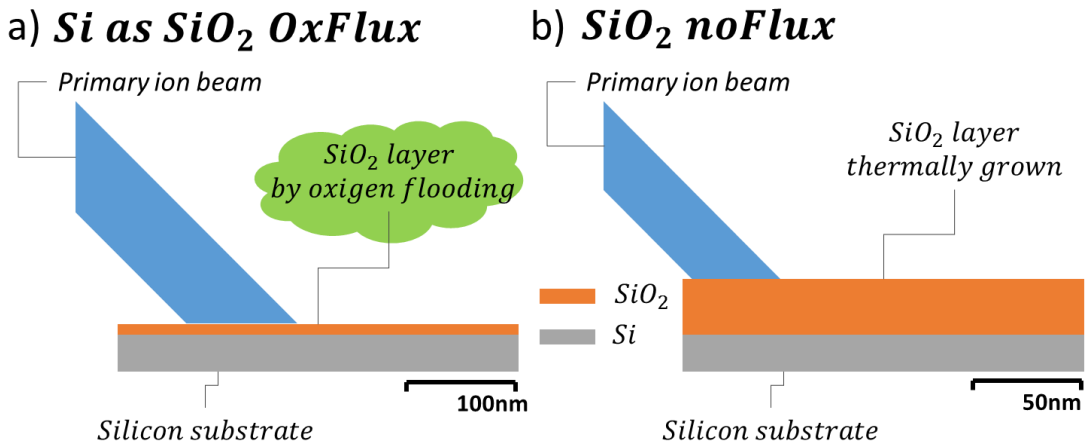

Figure 2.13: Schematic representation of a) silicon target oxidised in surface by an oxygen flooding (Si as SiO_2 OxFlux) and b) silicon sample with a thermally grown silicon dioxide layer (SiO_2 noFlux) employed to determine sputter rate and yield of oxygen primary source..

In Figure 2.14-a, the comparison between the sputter yield of silicon sputtered during oxygen flooding and SiO_2 shows that silicon dioxide is easily sputtered at any energy compared to silicon. An intermediate behaviour is defined and it assumes values corresponding to a silicon dioxide surface enriched in oxygen ($SiO_2\ noFlux$) for low sputtering energy condition (500 eV). Concerning higher energy values, they are associated to sputter yield data characteristic of silicon sample oxidised by an oxygen flux with a reduced implantation of oxygen primary ions "$Si\ as\ SiO_2\ OxFlux$". Comparing this result to the curves representing the oxygen sputter rate, the differences in trend between 500 eV and 1 keV can be associated to a variable amount of oxygen retained in the silicon dioxide composing the surface.

In Figure 2.14-b, sputter rate values of samples described in Figure 2.13 are plotted. Comparing the sputter rate trend to the relative SR in Figure 2.12-c-d as function of the energy, it can be concluded that sputter rate of porous samples at low sputtering energy

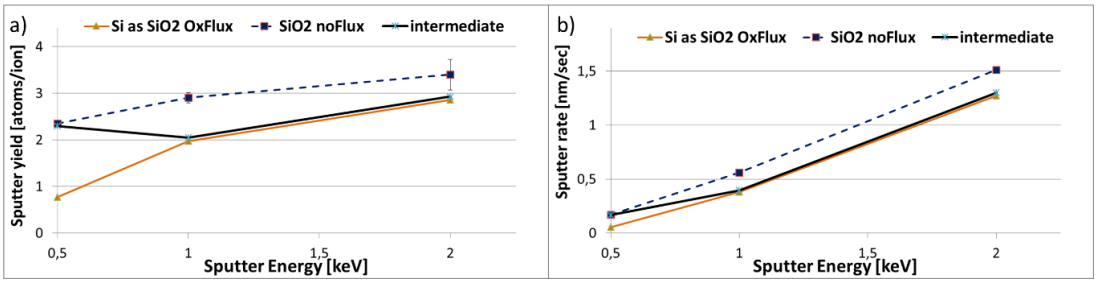

Figure 2.14: a) Sputter yield and b) sputter rate comparison of silicon and silicon oxide systems described in Figure 2.13 sputtered by O_2^+ primary ions.

presents higher values due to the higher sputter yields of silicon dioxide. However, for higher sputtering energies, lower sputter yield characterise the sputtered target and the difference in sputter rate between reference and porous sample is lower.

PRELIMINARY CONCLUSION

In conclusion, distinctive trends depending on the sputtering sources are underlined and interpreted. In caesium and xenon sputtering mode, the behaviour observed for high sputtering energies and overall porosity above 50% is associated to a particular sputtering phenomenon characterised by the presence of multiple sputtering sites per impacting energetic ion. In the case of overall porosities lower than 50% the sputter rate stabilisation is interpreted as a surface densification due to a pore sealing probably induced by a local melting of the surface as observed for nanoparticles described in section 1.2.1.

The sputter rate results and attempts of explanations are now compared to SEM observations.

2.3.2 SURFACE MODIFICATIONS OBSERVED BY SCANNING ELECTRON MICROSCOPY (SEM)

As already stated in section 2.1.2, scanning electron microscopy observations were performed in order to observe the surface changes induced by energetic ion bombardment on the porous silicon morphology. In order to unify and correctly interpret the data collected, all the observations have been performed after sputtering one-third ($\sim 70\ nm$) of the depth of the entire porous layer. In order to have a quantitative appreciation of the sample roughness, atomic force microscopy measurements in tapping mode have been made but the process was too detrimental for the AFM tip and no reliable results were

obtained; as a consequence only qualitative observations of this parameter has been made by tilting samples during SEM observations.

The craters left by SIMS analysis was clearly visible with SEM observations and each crater bottom has been observed perpendicularly and 40° tilted from the sample surface (Figure 2.15).

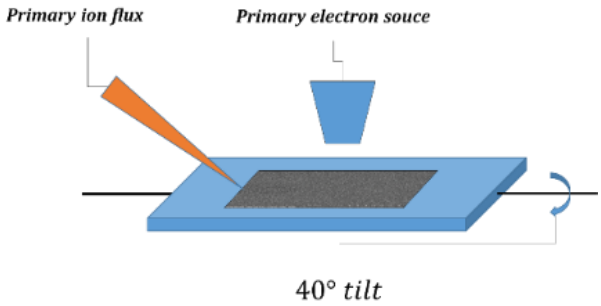

Figure 2.15: For all the proposed SEM observations, primary ion flux comes the left. SIMS and SEM are not coupled, this is a schematic representation to guide the reader through the result comprehension.

In the previous study regarding sputter rates, a threshold at 50% of overall porosity was estimated to separate two distinct behaviours. These behaviours corresponded to a constant increase of the SR for high porous samples increasing sputtering energy while in the other case a stabilisation was observed and interpreted as a "surface densification". A distinction in sputter rate observation was effectively obtained under and above 50% overall porosity. For convenience of legibility and information densification, only the results for samples at 40% and 60% of porosity will be shown as representative of these two discriminated populations.

CAESIUM SPUTTERING SOURCE

In Figure 2.16 the images of the bottom crater morphology sputtered by caesium are presented. It can be observed that radical changes take place, depending on the overall porosity. In the case of 60% porosity, the increase in sputtering energy induces an enlargement of pore diameter. The extreme case is presented by 2 keV sputtering where a pore lengthening along sputter direction is observed suggesting the idea of pore "coalescence". The term coalescence can appear inappropriate but it is thought to well describe the phenomenon of pore connection that can take place when a solid pore structure is sputtered. Considering the 40% porosity sample, the pore shape is maintained through the sputter energies used but at the same time, a decrease in the pore concentration on surface is observed for higher sputtering energies. In this case, surface

starts to present the aspect of a locally densified material, supporting the theory of surface densification inducing the sputter rate stabilisation observed previously (see Figure 2.9).

Tilted images (Figure 2.17) are also proposed in order to qualitatively estimate the surface roughness. Concerning the 60% porous sample, a roughness increase is observed as a function of the sputtering energy.

This increased roughness is thought to be due to preferential sputtering of silicon thin membranes compared to pore solid pillars On the contrary, sputtered surface of the 40% overall porosity sample at any sputter energy presents a lower roughness compared to 60% porous sample. In this case, the appearance of wavelets nano-patterned structure suggests a rearrangement perpendicular to the sputtering direction with a consequent sealing of pores. This observation completes the theory of the surface densification observed in the sputter rate study (stabilisation of SR, see Figure 2.9) and by the top surface SEM observations (decrease of pore concentration). These morphological changes depending on overall porosity and sputtering energy are expected to take place also with the other sputtering sources.

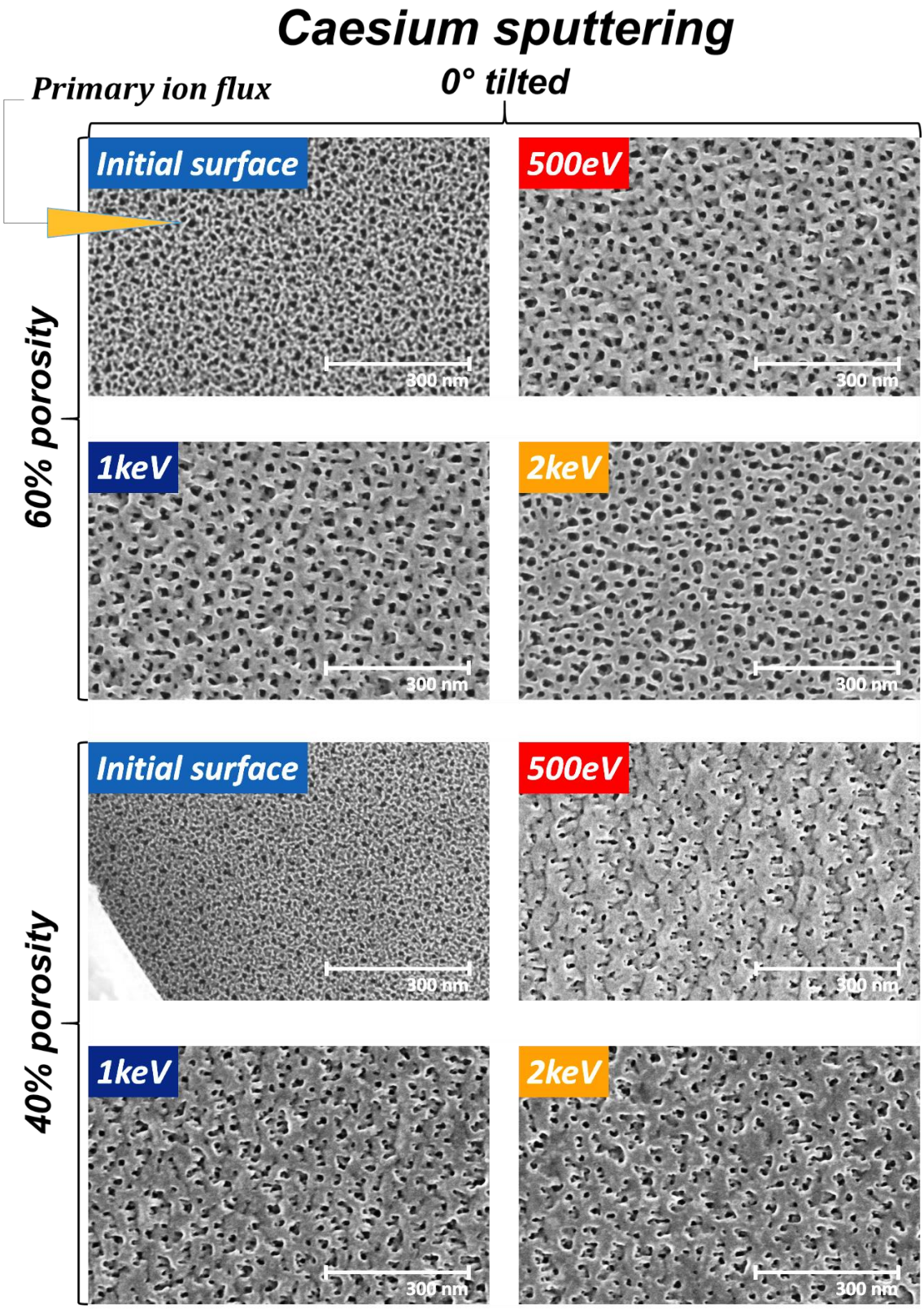

Figure 2.16: 0°tilt SEM image of 60% and 40% porous samples sputtered by caesium ion source.

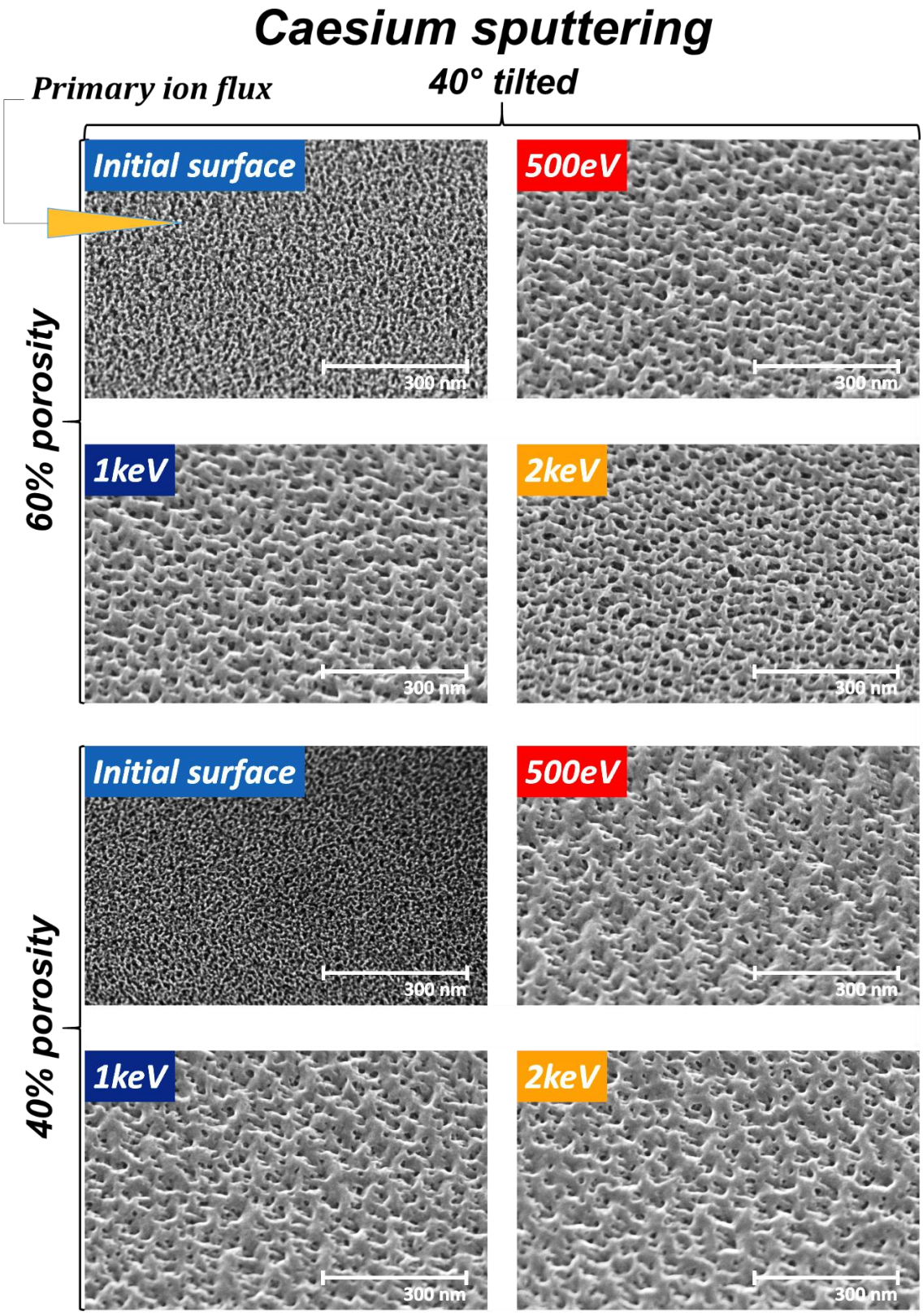

Figure 2.17: 40°tilt SEM image of 60% and 40% porous samples sputtered by caesium ion source.

XENON SPUTTERING SOURCE

An identical study is then performed using xenon as a sputtering source (Figure 2.18). It is important to remind that xenon and caesium have similar atomic weights and then a similar effect on the p-Si surface during sputtering can be expected; but there is a considerable difference in Xe/Cs ion fluences rates, in a fraction of 1.25 to 3 between 500 eV and 2 keV. This difference is accentuated at high sputtering energies. An important surface morphology difference at 2 keV between the used sources can be expected. Surface observations at 1 keV are not proposed because of the limited interest as they are comparable to surfaces sputtered by caesium at the same energy.

During the SR study on xenon sputtered samples, results showed that much higher sputter rates are obtained compared to caesium (see Figure 2.11). Similarly to caesium, the 60% porous sample surface indicates that a "pore coalescence" takes place at high sputtering energies. However, observing surface in tilted images suggests that roughness surface is smoother compared to surface sample sputtered by caesium (Figure 2.17). As underlined previously, high primary currents are characteristic of xenon ion beam. Under these conditions, the difference in sputtering rate between solid pillars and thin membranes separating them is expected to be smaller. Roughness will be then lower compared to the surface of the sample sputtered by caesium.

The surface aspect of the 40% porous sample sputtered by xenon is comparable to caesium sputtering for every sputtering energy. It can be concluded that also in this case a surface densification occurs.

OXYGEN SPUTTERING SOURCE

Scanning electron microscopy observations are also performed for porous samples sputtered by oxygen (Figure 2.19). The presence of an oxygen flooding do not change the aspect of the obtained surface morphology, as a consequence, no distinction is made in this section between the two modes. As observed for the other sputtering settings of 60% porous sample, low energy sputtering mode (500 eV) surface is uniformly sputtered and the corresponding 40° tilted image shows a reduced surface roughness in low energy sputtering mode (500 eV). When sputtering energy is increased marked horizontal traces parallel to the sputtering direction appear. This phenomenon has been already observed with caesium sputtering but it appears more evident during oxygen bombardment. This trend is also observed at 1 keV sputtering (not shown here) and morphologies are

comparable to 2 keV sputtering. The reason can be explained by the high primary ion doses involved comparable to xenon sputtering. However, oxygen being a reactive specie, the surface exposed to the ion flux is oxidised. As a consequence, thin solid membranes are easily sputtered compared to solid silicon pillars. As SiO_2 is easily sputtered compared to silicon, the resulting morphology is characterised by a high roughness such as for high energetic caesium sputtering. Surfaces of 40% porous sample sputtered with an O_2^+ source present many morphological similarities characterised by the caesium and xenon bombarded surfaces with same porosity. In all cases the appearance of wavelet nano patterned structure suggests a local fusion of the top surface with a consequent pore sealing.

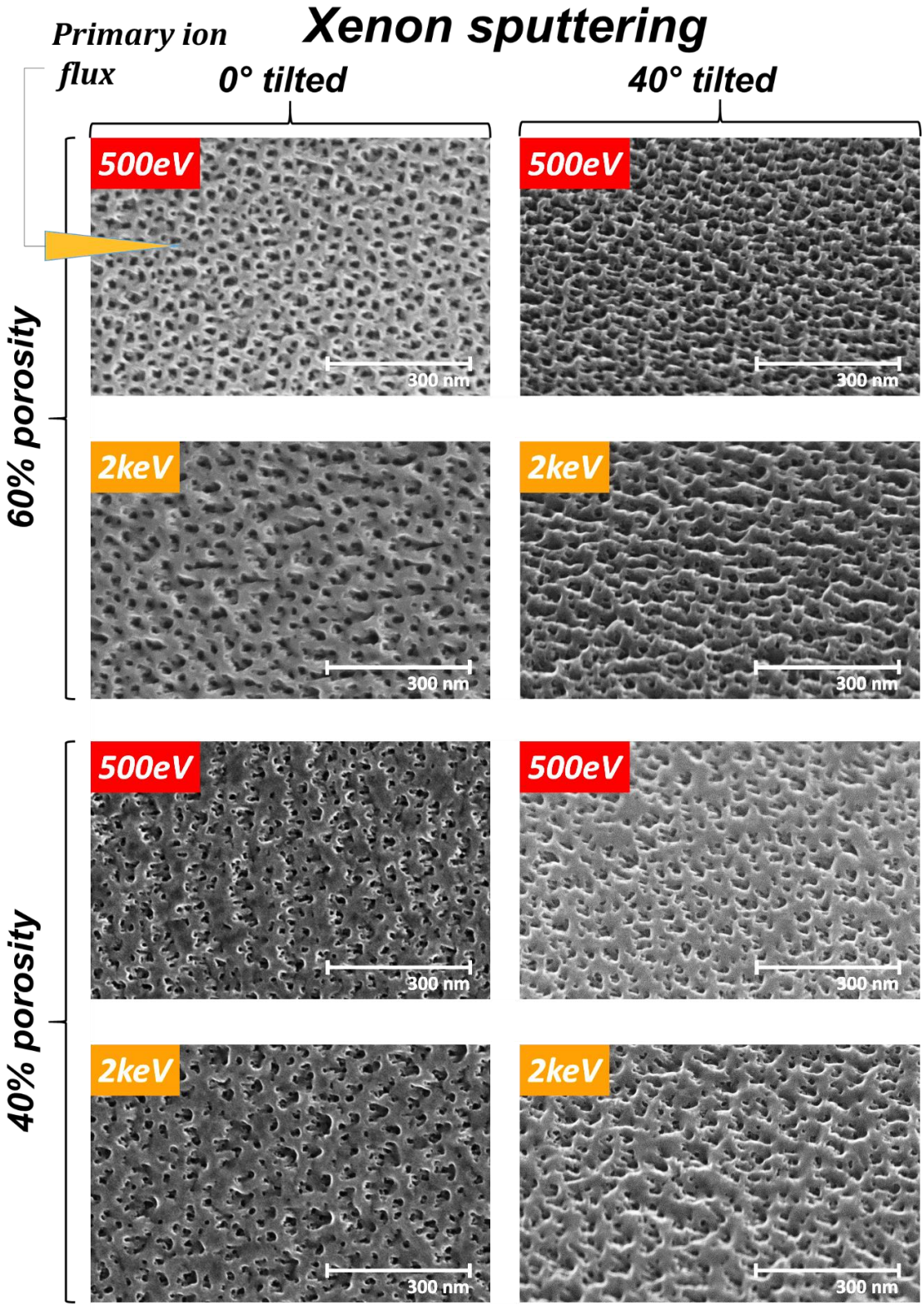

Figure 2.18: 0° and 40° tilt SEM image of 60% and 40% porous samples sputtered by xenon ion source.

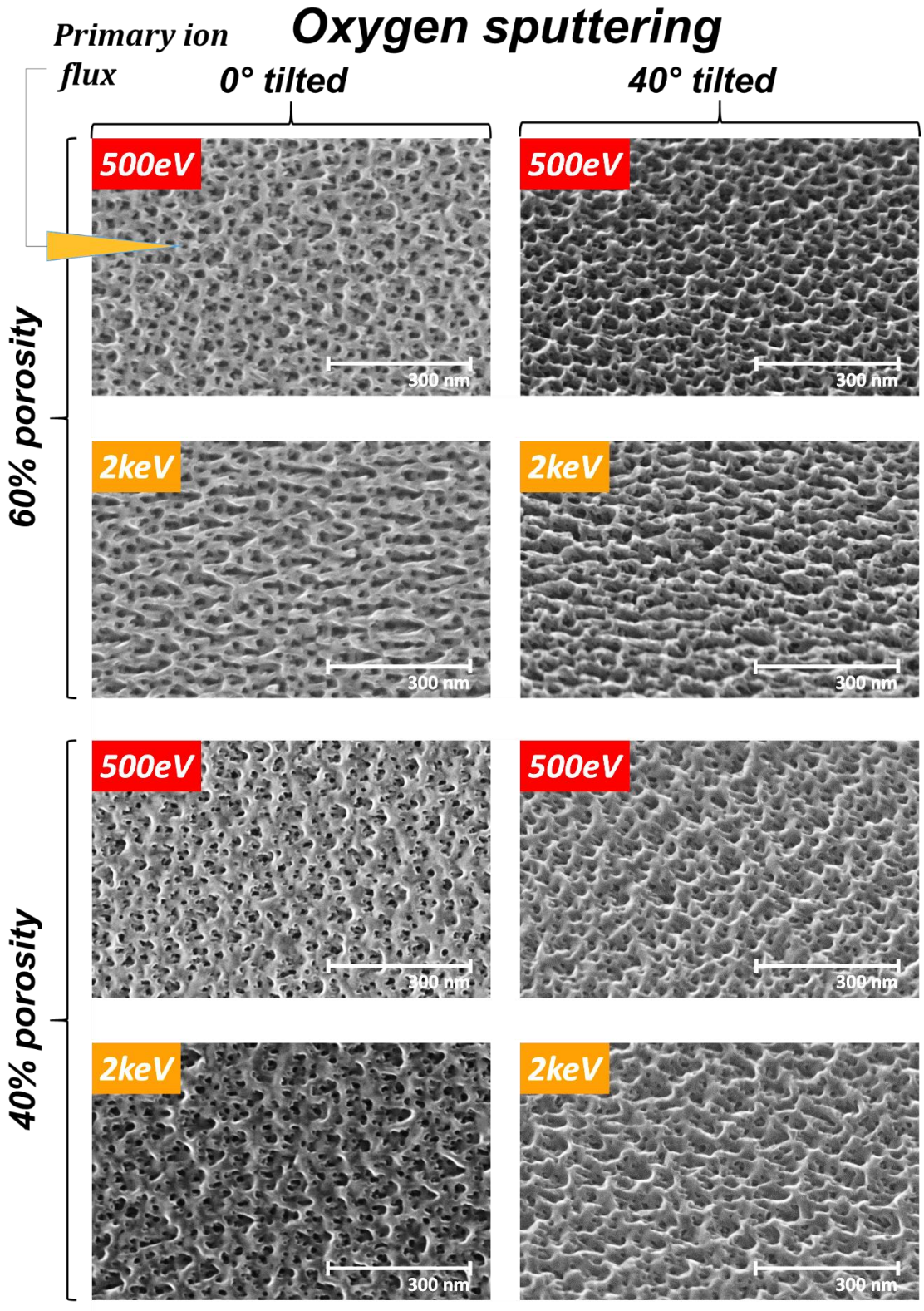

Figure 2.19: 0° and 40° tilt SEM image of 60% and 40% porous samples sputtered by oxygen ion source.

PRELIMINARY CONCLUSION

Important morphological changes caused by specific sputtering conditions are then revealed on samples with a variable porosity. A threshold at around 50% of the overall porosity has been identified as a porosity limit separating two distinct surface morphological phenomena modifications:

- Under 50%: pore sealing and surface densification
- Above 50%: pore coalescence and preferential sputtering of thin solid membranes in between columnar pores in the sense of the sputtering ion flux.

This limit is consistent with most of the observations made for relative sputter rate considerations. In the following sections, the impact of these different sputtering ions will be observed and explained from the point of view of matter ionisation and chemical information obtained from the in-depth profiling of the p-Si samples.

2.4 CHEMICAL APPROACH: IMPACT OF THE SPUTTERING CONDITIONS ON THE OBTAINED SECONDARY ION INFORMATION

2.4.1 VARIATION OF IONISATION DEPENDING ON THE APPLIED SPUTTERING ENERGY

Before going further in this chemical approach it is important to remind that the secondary ion information detected is obtained by bismuth primary ion bombardment and not by the different species previously considered for sputtering. However, as explained in section 1.1.3 the sputtering conditions have an impact on the generated secondary ion information and this is what is going to be studied here.

In Figure 2.20, 60% and 40% porous sample are sputtered by a 2 keV caesium source and depth profiles are given. As a complement of information, the depth profile of the "boron delta layer" sample analysed in the same conditions is given too. Two peaks are plotted:

- $^{30}Si^-$ peak: it is representative of the entire material as it is composed of silicon
- F^- peak: characteristic for both surface contamination (delta layer) and residual element of pore formation process

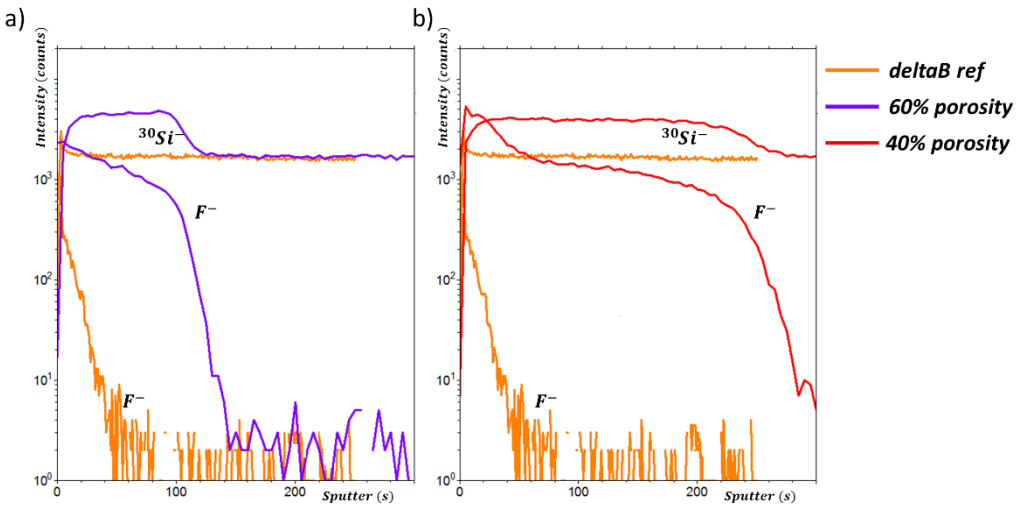

Figure 2.20: In-depth profiles of 2keV caesium sputtered samples for a) 60% and b) 40% porosity compared to delta layer depth profile.

In Figure 2.20-a-b, a clear distinction is observed between porous and dense layer. Fluorine is also present in the whole porous layer due to the production method involving HF diluted solution. It is important to underline how silicon and fluorine signals decrease

to the values of a dense silicon material (sputtered in the same conditions) as the porous layer is sputtered. Furthermore, in Figure 2.20, the behaviour of porous layer signal allows distinguishing pore/dense interface assuming bulk like intensities once the porous layer is sputtered. Referring to "delta layer" sample, fluorine is present only at the surface indicating a contamination limited to it. These conclusions are formulated observing depth profiles acquired by caesium at 2 keV, but for the definition of a descriptive model, 500 eV and 1 keV depth profile behaviours were also studied.

CAESIUM SPUTTERING SOURCE

In Figure 2.21, silicon signal ($^{30}Si^-$), characteristics of the bulk, and oxygen signal (O_2^-), characteristics of pore surface chemistry are plotted in-depth for each used caesium sputtering energy, for 40% and 60% porosity samples, above and under 50% overall porosity "threshold" (Figure 2.9). It is important to remind that in-depth profiles are normalised to the intensity of $^{30}Si^-$ in the bulk in order to take into account the decrease of ionisation yield due to the decrease of the caesium surface coverage (energy dependent) as presented in section 1.1.3.1. Thanks to this normalisation coupled, significant differences in depth profiles can be identified respectively for porosity or energy variation. For the 40% porous sample, $^{30}Si^-$ flat trend till the interface is observed during 1-2 keV caesium sputtering mode, while a positive slope is characteristic of 500 eV sputtering. Instead, for the 60% porous sample, all increasing curve tilts are observed through the porous layer till the interface. This discrepancy between in-depth profile is thought to be connected to ionisation differences. These ionisation differences are related to the presence of variable concentrations of caesium on the surface as a function of the surface exposed to the ion beam (linked to overall porosity) and the in-depth presence of reactive ions (caesium in-depth diffusion and accumulation). This phenomenon seems to be limited for the oxygen O_2^- signal where all the decreasing trends through the porous layer till the interface are similar probably due to the fact that this chemical information comes only from the pore surface.

However, an oxygen signal behaviour difference between porous samples is observed in the first 40 nm of the porous layer. In 40% porosity sample a fast decrease followed by a rapid increase of the O_2^- signal is observed. This phenomenon is more visible at low sputtering energies as sputter rates are reduced and it is attributable to a "transient" phenomenon induced by the presumed matter melting coupled with pore sealing before reaching a stable state. The described "transient" is not to be confused with the transient

normally taking place during the very few first scans inducing changes in the depth profiles caused by non-equilibrium processes accompanying the build-up of a steady-state concentration of the primary ions near the sample surface [10]. However, this transient is not observed for 60% porous sample.

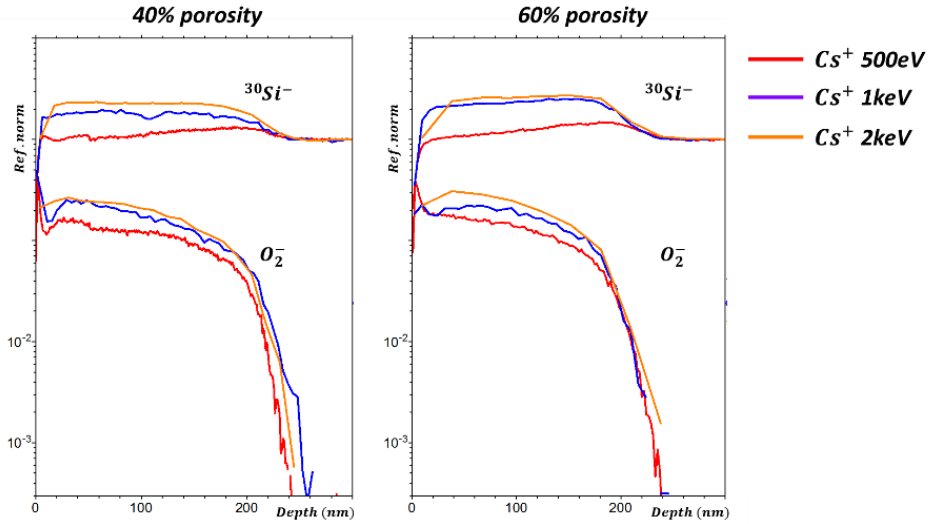

Figure 2.21: In-depth profiles of caesium sputtered porous samples normalised to the bulk $^{30}Si^-$ signal intensity.

Other chemical species characteristic of surface chemistry such as hydrogenated silicon (SiH^-) or silicon dioxide (SiO^-) are plotted to validate this observation as shown in Figure 2.22. The identical trend observed previously on O_2^- signal is found in the first 40 nm of the 40% porous sample in-depth profile. This similarity indicates that only chemical species present on pore surface are influenced by the so-called "pore sealing" phenomenon. On the other hand the "pore coalescence" phenomenon, i.e. related to samples over 50% of porosity, represented here by the 60% sample data, does not appear to produce visible modifications in the acquired in-depth profiles.

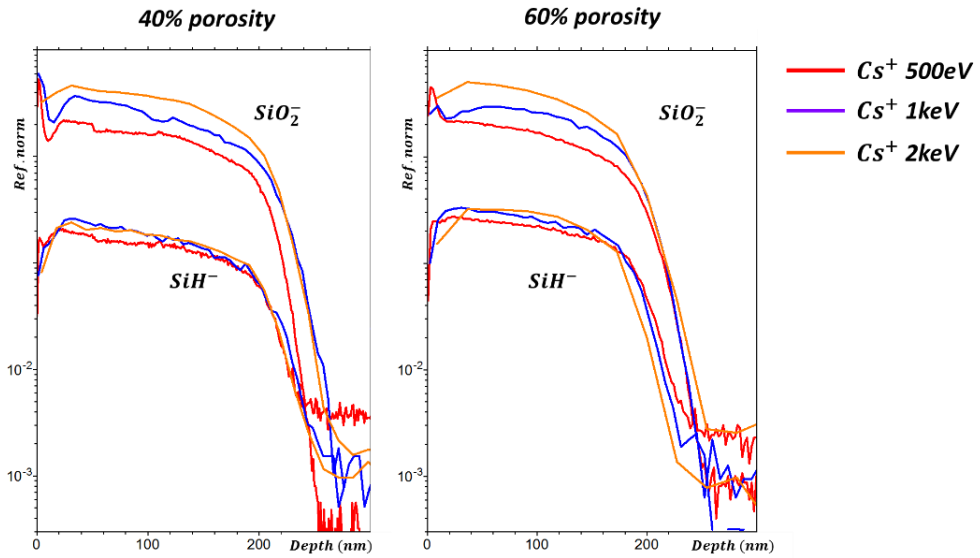

Figure 2.22: In-depth plot of chemical fragments characteristic of porous silicon sample surfaces. Profiles are normalised by the $^{30}Si^-$ peak intensities in the bulk.

In conclusion, caesium is found to play a key role in ionisation phenomena and its concentration in surface and in-depth is linked to its diffusion through pores during analysis and to the overall porosity of the sample. Indeed, during SEM observations of sputtered surfaced by caesium, it was common to find agglomerates at the bottom of SIMS craters. An Energy Dispersive X-ray Analysis (EDX) performed on some of the agglomerates showed that their chemistry was mainly composed by caesium as shown in Figure 2.23.

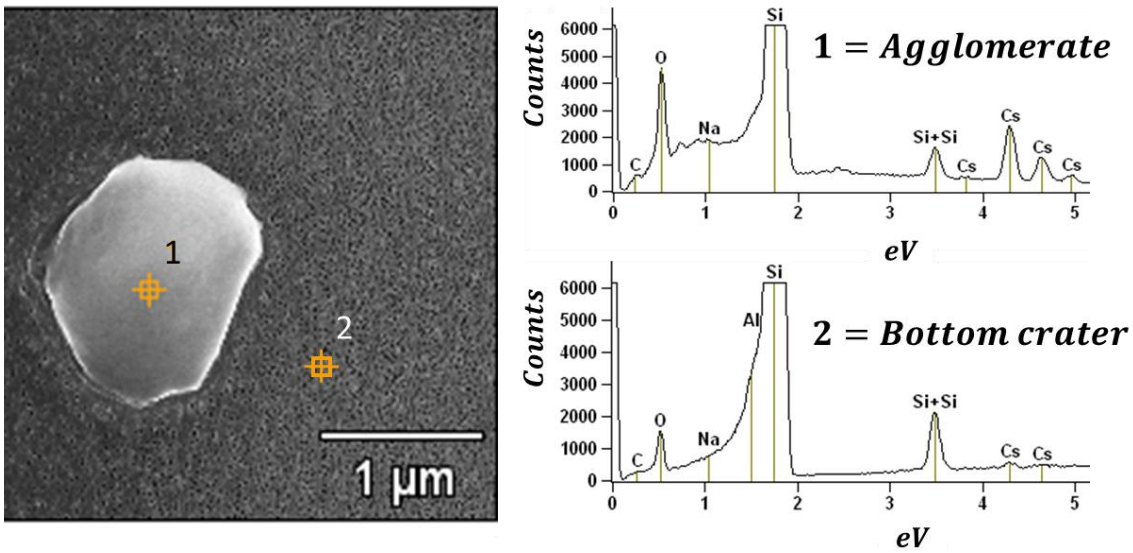

*Figure 2.23: a) caesium agglomerates observed by SEM and b) EDX analysis of an agglomerate (*1) and of the zone around it (*2).*

In order to further validate and discriminate the ionisation effects of caesium, in-depth profiles of the same samples were acquired using xenon that is known not to have the same reactivity of caesium with target material.

XENON SPUTTERING SOURCE

In Figure 2.24 such as for caesium study, 40% and 60% porous samples have been profiled by xenon energetic primary ions and corresponding depth profiles are plotted. In this case, the choice of plotted ions is different compared to the caesium case mainly because in this case positive secondary ion information is analysed. As xenon do not participate in the ionisation process as caesium does, the ionisation is only driven by primary analysis ions (bismuth ions) and the choice of the detection mode (negative or positive) depends on the secondary information needed. Saturated signals such as silicon during caesium bombardment become analysable during xenon bombardment and, as a consequence, isotopes such as $^{30}Si^{+}$ becomes much less intense. In both analysed samples, the silicon (Si^{+}) signal follows an identical trend for each sputtering energy. Concerning the 40%, the pore/bulk ratio decrease with the increase of sputtering energy while in 60% sample, the 500 eV, 1 keV and 2 keV match. The Si^{+} trend is compared with the $^{30}Si^{-}$ caesium depth profiles in Figure 2.21. Regarding caesium in-depth trends, different slopes were observed depending on the sputtering energy used probably due the secondary ion enhancement induced by deposited caesium during analysis. However, the observed signal depletion in the first 40 nm of porous layer for caesium sputtered 40% porous sample is also present during xenon sputtering . This common observation suggests that this phenomenon does not depend on the primary source used but probably by a macroscopic common phenomenon such as a morphological modification (“pore sealing”) described and observed in section 2.3.2.

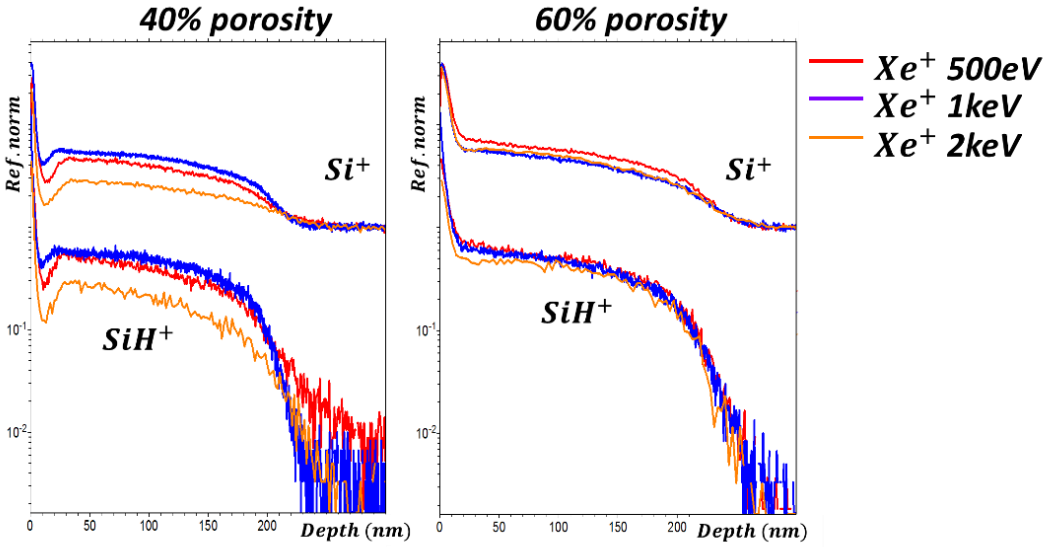

Figure 2.24: In-depth profiles Si^+ and SiH^+ of xenon sputtered porous samples normalised to the bulk Si^+ signal intensity.

In Figure 2.25 the in-depth profiles of $SiOH^+$ representative of oxygen content in samples are normalised by the Si^+ intensity in the bulk and plotted for 40% and 60% porosity samples. Oxygen such as hydrogen is characteristic of the surface chemical composition of pores and absent in the bulk. Results are consistent with depth profiles presented in Figure 2.24 with a decrease of intensity at the bulk silicon interface and the presence of a transient at 40% porosity (first 40 nm) attributed to morphological modifications, in particular the "pore sealing".

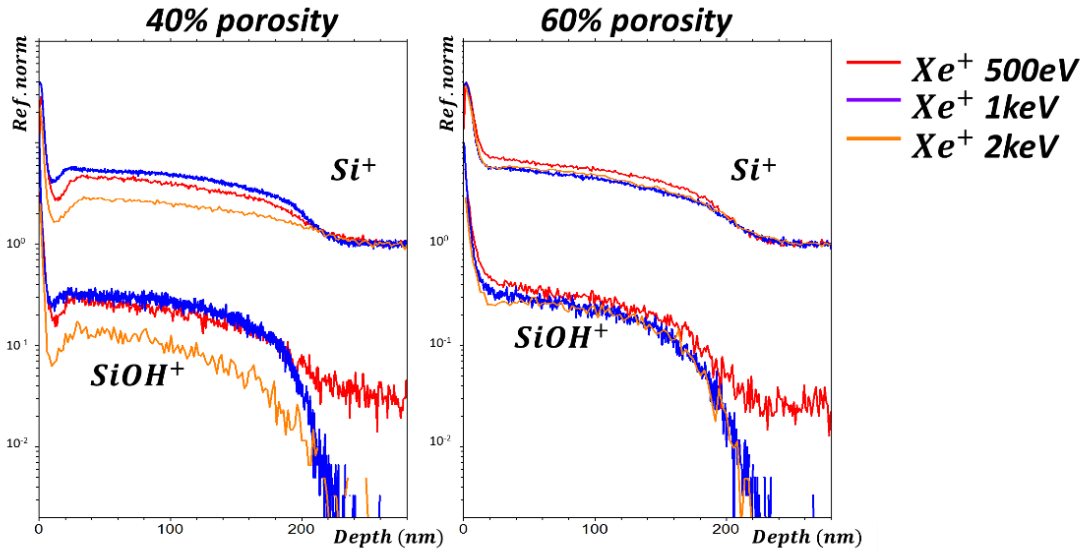

Figure 2.25: In-depth profiles Si^+ and $SiOH^+$ of xenon sputtered porous samples normalised to the bulk Si^+ signal intensity.

Comparing in-depth profiles of caesium and xenon some aspects are observed to change. In particular, the silicon signal observed to considerably change as a function of caesium energy. Silicon conserves a relative similar trend during xenon in-depth profiling between sputter energies and in both cases, a transient is observed for samples under 50% porosity.

OXYGEN SPUTTERING SOURCE

As described in the strategies (section 2.1.2) in-depth profiling performed by oxygen sputtering was performed in two different modes: in ultra-high vacuum conditions such as for caesium and xenon sputtering mode ($\sim 5x10^{-9}\ mbar$) or with an oxygen additional flux in the main chamber with a vacuum of $\sim 3x10^{-6}\ mbar$ creating a supplementary oxidising atmosphere. In Figure 2.26, in depth profiles of $^{30}Si^{+}$ and SiH^{+} are plotted for 40% and 60% porous samples. In the case of oxygen sputtering in absence of additional oxidising flux, the profiles corresponding to the three sputtering energies draw a comparable trend. This trend describes a plateau till the interface pore/bulk followed by a decrease of intensity. This decrease is more evident for SiH^{+} signal because of the much lower proton content in the bulk.

The addition of the oxygen flux in the analysis chamber radically change the aspect of depth profiles. The most affected by the oxygen flux are the depth profiles acquired while sputtering at 500 eV. Both for 40% and 60% porous samples the Si^{+} curves has a decreasing slope compared to higher sputter energies. Unexpected is the in-depth behaviour of SiH^{+} at 500 eV sputtering in 40% porous sample that increases in intensity till the bulk where theoretically should decrease in intensity (new in-depth acquisitions could clarify this behaviour). It was not possible to rely this observation to a valid explication. On the contrary, SiH^{+} signal at 500 eV sputtering in 60% porous sample has the expected behaviour but with intensities much lower compared to higher sputtering energies.

During caesium, xenon and oxygen sputtering mode, the differences in intensities between pore and bulk layers vary as a function of the sputtering energy. Observations performed on 40% and 60% porous samples are then extended to the entire sample set by the extrapolation of ionisation intensities to numerically evaluate data trends. In particular, pore/bulk intensity ratios are calculated on reference ions such as silicon and plotted as a function of overall porosity and applied sputter energy as shown in the following sections.

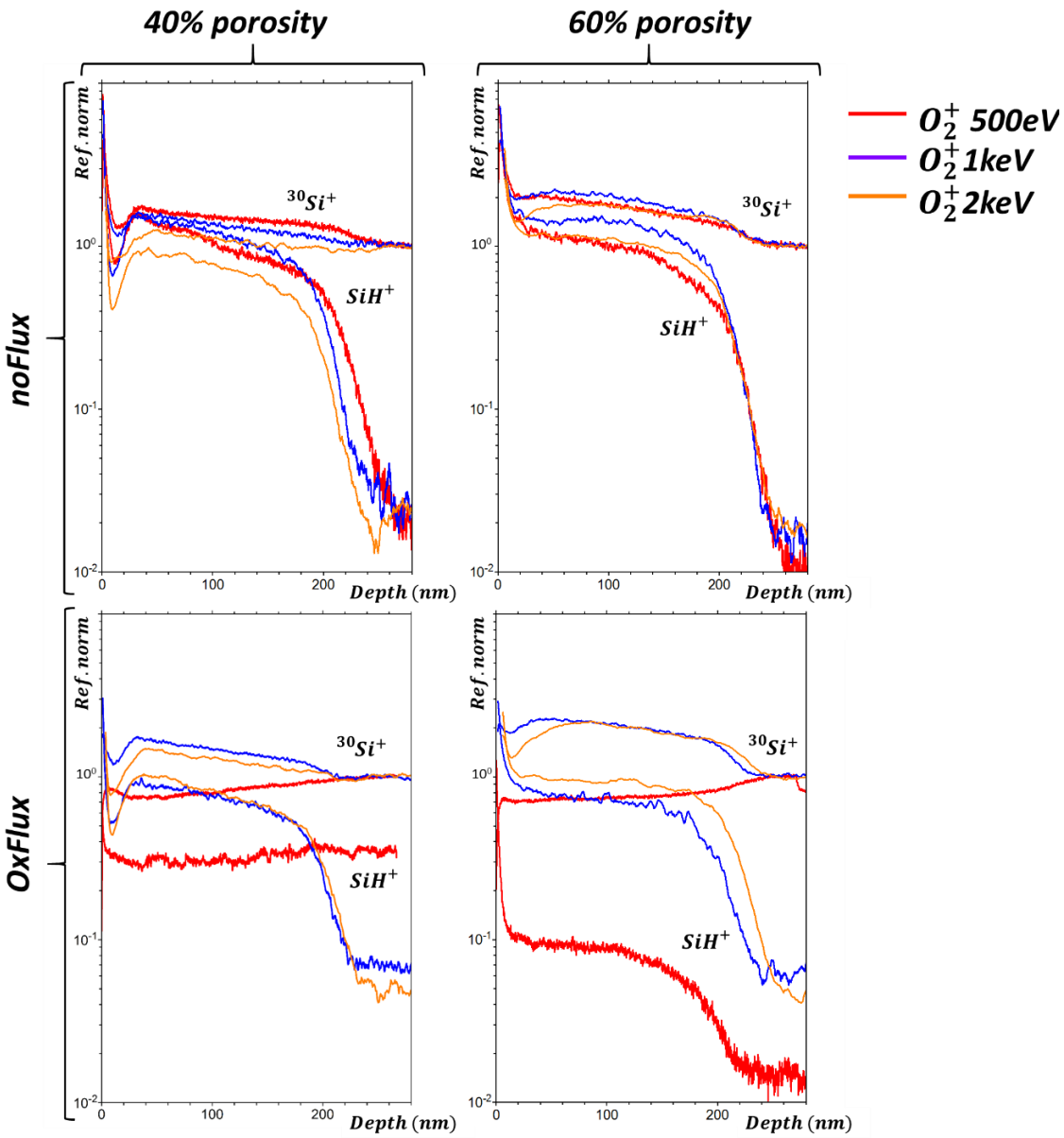

Figure 2.26: In-depth profiles of $^{30}Si^+$ and SiH^+ ions for 40% and 60% porous sample sputtered by oxygen with (OxFlux) and without (noFlux) the supplementary oxygen flux in the analysis chamber. Profiles are normalised by the intensity of $^{30}Si^+$ signal in the bulk.

2.4.2 Role of the primary source on the ionisation phenomena

In this section, the observations and explanations given on depth profiles are tabulated for the entire sample set and used energies. Indeed, as observed in depth profiles, significant pore/bulk ionisation differences were observed.

2.4.2.1 SILICON BULK IONISATION BEHAVIOUR DEPENDING ON THE SPUTTERING SOURCE AND ENERGY

At first, bulk intensities of silicon signals were tabulated and plotted in Figure 2.27. The choice of the silicon or its isotope for data tabulation was choosen with the same criteria used for in-depth studies. As expected, bulk $^{30}Si^-$ intensity is inversely proportional to the caesium sputtering energy. The reason is found in the surface caesium concentration that decreases while increasing sputter energy as explained in section 1.1.3.1 [69]. Instead, Si^+ intensities generated by bismuth ion bombardment, while sputtering with a xenon source are only weakly impacted by the sputtering energy. Same behaviour is observed for dense samples sputtered by O_2^+ source. However, the presence of an oxygen flooding in the analysis chamber induces a data discrepancy especially at low sputtering energy. It is deduced that the oxidation kinetics is not optimised at higher sputtering energies.

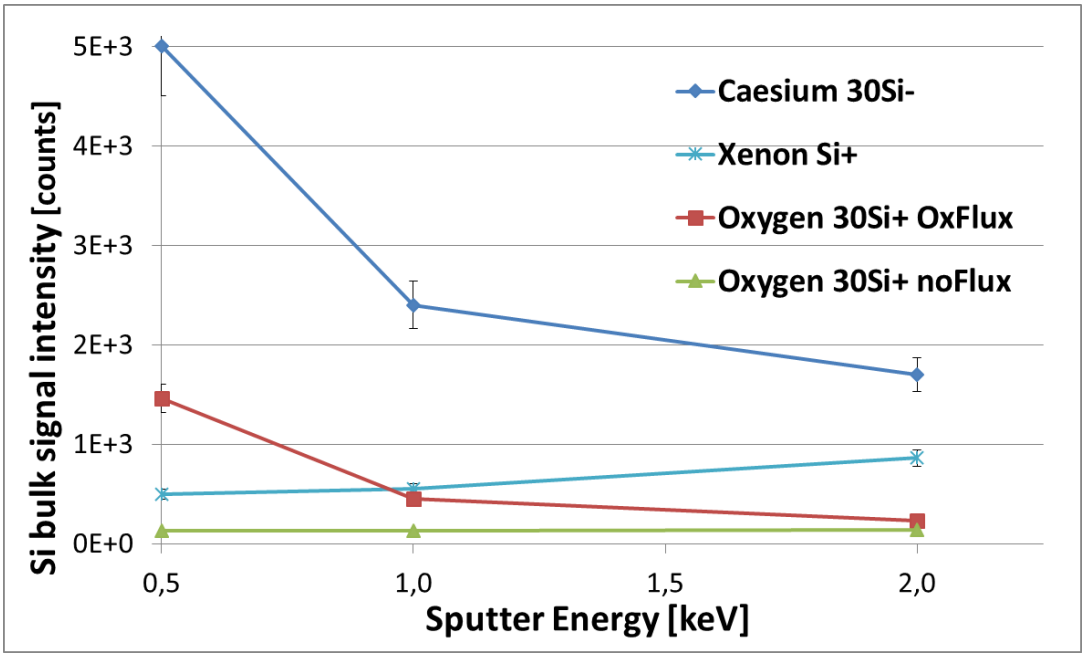

Figure 2.27: Plot of silicon trends in dense silicon reference as a function of sputter energy and source.

The data trend observed on a silicon dense reference depending on the primary ion source are thought to be enhanced in presence of pores and function of the overall porosity.

2.4.2.2 STUDY OF THE POROUS/BULK IONISATION PHENOMENA DURING SOURCE SPUTTERING

In this section, the role of porosity on the ionisation efficiency is investigated as a function of the used primary sources. In order to do so, the tabulated intensities of silicon or its isotopes in the porous layer were normalised by its value in the dense reference and results are plotted. As for the previous study on the bulk ionisation, silicon signal or its isotopes well describe the in-depth profile. Silicon signal is indeed a good marker for the study of pore/bulk ionisation phenomena distinguishing the porous layer from the bulk.

The silicon intensity in the porous layer is extrapolated at the maximum value of the ${}^{*}Si_{pore}$ intensity in the porous layer while ${}^{*}Si_{bulk}$ intensity is extrapolated in the zone of depth profile after pore/ion interface (Figure 2.28).

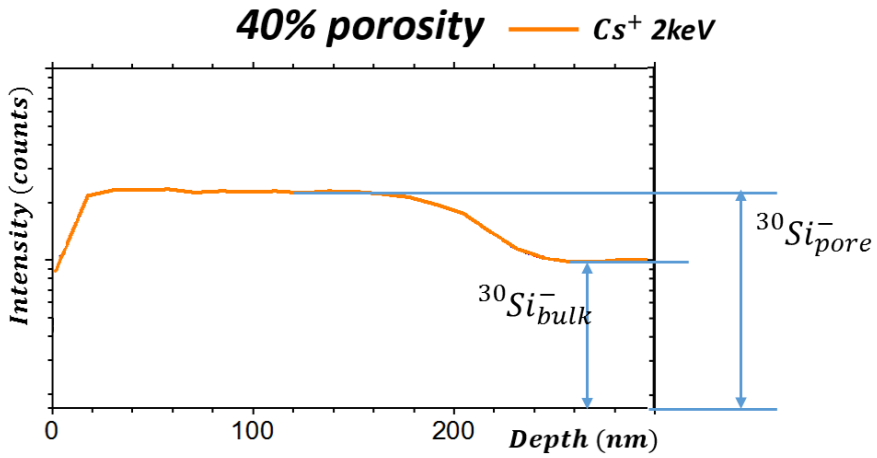

Figure 2.28: ${}^{30}Si^{-}$ in-depth profile of the 40% porous sample showing ionisation levels in porous and bulk silicon.

The Eq.2-3 is applied to the entire set of measurements covering the complete set of samples sputtered by caesium. This operation is repeated for each sputter energy (E_i) used.

$$I_R = \left(\frac{I_{porous\ layer}}{I_{bulk}}\right)_{E_i} \qquad \textit{Eq.2-3}$$

CAESIUM SPUTTERING SOURCE

In Figure 2.29 the results obtained applying Eq.2-3 are reported. In Figure 2.29-a, 500 eV relative ionisations (I_R) appear to be only slightly impacted by the overall porosity value. Considering 1 keV sputtering energy, an increase in relative ionisation is only observed for samples with an overall porosity above 50%. In 2 keV caesium

bombardment, a reduced decrease (in the error range) of ionisation rate under 50% porosity is observed while I_R values increase above 50% porosity.

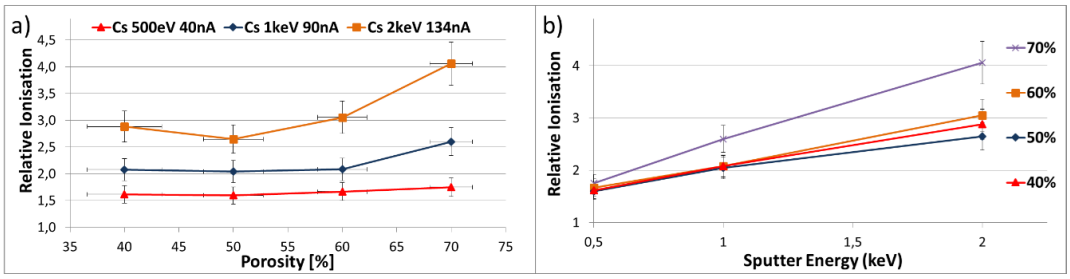

Figure 2.29: $^{30}Si^-$ relative ionisation plotted values a) as a function of overall porosity and b) function of the used sputtering energy.

As 500 eV I_R values are restrained to a quasi-horizontal trend at all the characterised overall porosities. It is then deducible that there is an important dependence to the caesium sputtering energy on this data system. To be more precise, at 500 eV sputtering, caesium ions are thought to be in high concentration on the porous layer and in the bulk their stopping range is calculated (TRIM) to be $\sim 2.6\ nm$. Then, in the porous layer and bulk, caesium actively participates to ionisation mechanisms (during secondary ion generation by bismuth primary ions) decreasing the pore/bulk ionisation discrepancies and also the impact of the porosity. On the contrary, at high sputtering energies, caesium is more implanted in depth, the resulting ionisation will be favoured in the porous layer having an impact on the pore/bulk relative ionisation. This ionisation phenomenon is observed to be function on the overall sample porosity.

In Figure 2.29-b relative ionisations are plotted as a function of the sputtering energy and a positive slope for every overall porosity is observed. In particular, 70% porosity sample is characterised by an enhanced increasing trend. TRIM simulations on the stopping range of bismuth applied settings are performed and tabulated in Table 2.5. Stopping range of bismuth ions suggests that, as deducted for caesium sputtering, multiple ionisation sites can be induced in the porous matter increasing the detected secondary ion signal. To be more precise, bismuth ions can cross solid silicon membranes and pillars separating poser with the consequent generation of multiple sites where ionisation takes place.

Table 2.5: Stopping range and sputter yield calculated by TRIM simulation of bismuth ions impacting a silicon dense target 45° tilted.

Ion	Stopping range	Sputter yield
15 $keV\ Bi^+$	$11 \pm 3\ nm$	$7.69\ at/ion$

XENON SPUTTERING SOURCE

In Figure 2.30-a, the relative ionisation yields as a function of the overall porosity of characterised samples sputtered by energetic xenon ions are plotted. It is observed that plotted data do not or slightly differ each other depending on the used sputtering energy. However, the overall porosity is the discriminating aspect between samples due to the availability of reactive species functionalising the surface. These reactive species are considered to be proportional to the porosity value as they are linked to the specific pore surface. Compared to caesium, where relative intensity was found to be a function of the applied sputtering energy, in xenon sputtering the contribution to relative intensity variation is only due to overall sample porosity. In Figure 2.30-b, the quasi-horizontal curves confirm that the sputtering energy has a marginal effect on data behaviour while the overall porosity dominates the trend. In particular, ionisation values for all the sputter energy increases consistently with the porosity value. Furthermore, as underlined for caesium sputtering, a discrepancy is observed between samples above and under 60% porosity concerning multiple ionisation sites induced by bismuth analysis primary ions.

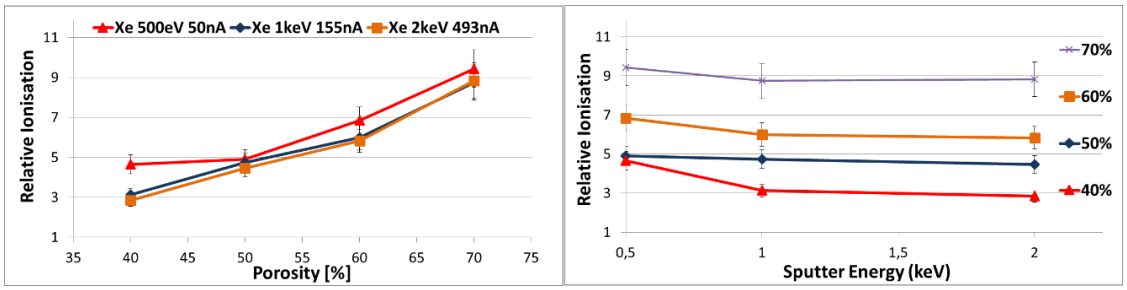

Figure 2.30: Si^+ relative ionisation plotted values a) as a function of overall porosity and b) function of the used sputtering energy.

The reported ionisation values under xenon bombardment are on average three times higher compared to caesium values. A valid explication is that once reached the interface with the bulk, silicon ionisation decrease considerably because of the absence of reactive species (mainly oxygen) involved in secondary ionisation.

OXYGEN SPUTTERING SOURCE

To complete the pore/bulk ionisation study, values for oxygen sputtering plotted as a function of the overall porosity are reported in Figure 2.31-a. Values obtained without additional oxygen flux are plotted in dotted lines. Values are characterised by an increasing trend proportional to the increase of the overall porosity. In Figure 2.31-b, ionisation values for each porosity are plotted as a function of the sputtering energy. It is observed a weak increase of relative ionisation at 1 keV oxygen sputtering but then values decrease at higher sputtering energies. This decrease is supposed to be linked to the amount of oxygen implanted in porous sample in the sputtering phase. As oxygen sputter rate in the porous layer is higher compared to bulk and increases with the sputtering energy, it means that a lower amount of oxygen has being implanted in porous matter in comparison to bulk material. As a consequence the pore/bulk ionisation rate is equivalent to the one in the bulk material but still higher because of the higher bismuth sputtering efficiency in porous matter.

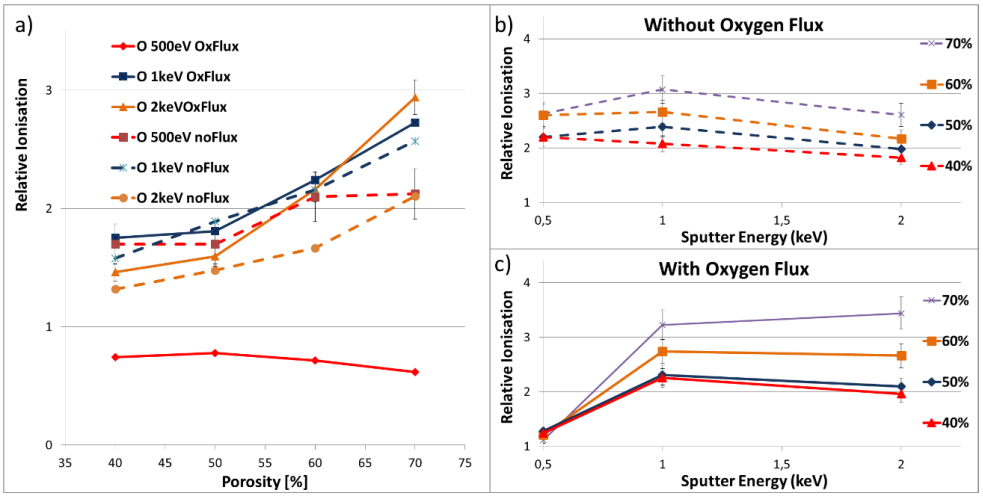

Figure 2.31: $^{30}Si^{+}$ relative ionisation plotted values a) as a function of overall porosity and b-c) function of the used sputtering energy.

On the other hand, continuous lines describe samples sputtered in presence of the additional oxygen flux (Figure 2.31-a). As observed in the depth profiling (section 2.4.1), the depth profiles at 1 keV and 2 keV present higher intensities compared to bulk; while 500 eV depth profile has a different behaviour. At 500 eV it seems to be constant or slightly decreasing with the increase of the overall porosity. In Figure 2.31-c the plot indicates that at 500 eV less secondary ions for all the porous samples, compared to bulk silicon are generated. It then rapidly increases at 1 keV followed by a stabilisation at 2 keV. The increase is observed to be more important for overall porosities above 50%.

The presence of an additional oxygen flux is shown to produce a secondary information enhancement. In particular, the reason for ionisation values in-between 0 and 1 at 500 eV sputtering suggests a higher ionisation in the bulk while at higher energies the ionisation promotes the porous matter. It is reasonable to think that at low sputter energies the oxidation kinetic of oxygen flooding is more efficient in the bulk as sputter rate is lower. The resulting bulk chemistry will be more enriched in oxygen inducing a higher secondary signal compared to the porous layer.

2.5 CONCLUSION AND PERSPECTIVES

In order to study the interaction between ion beams, conventionally used in a SIMS instrumentation, and porous silicon, a set of samples with a varying porosity has been characterised by ToF-SIMS. Different sputtering ions, at different energies and fluences have been considered. Their impact has been evaluated considering physic(sputter rate, surface morphological modifications)-chemical (secondary ion counting) parameters.

Deep and different morphological changes caused by specific sputtering conditions are then revealed on samples with a variable porosity. A threshold at 50% of the overall porosity has been identified as a porosity, limit common to all sputter sources, separating two distinct surface morphological phenomena modifications:

- Under 50%: pore sealing and surface densification
- Above 50%: pore coalescence and preferential sputtering of thin solid membranes in between columnar pores in the direction of the sputtering ion flux

Regarding the secondary ion information, specific behaviours depending on the used primary ion beam were observed. Caesium was found to play a key role in ionisation phenomena and its concentration in surface and in-depth was supposed to be linked to its accumulation and diffusion through pores. As a matter of facts, the detected secondary ion information was found to be tightly related to the sputtering energy used, in particular at low energies, the contribution of porosity on the ionisation is minimised compared to higher energies. This observation was shown to be linked to the varying implantation depth of primary reactive ions and their involvement in ionisation processes.

In the specific case of xenon as sputtering source, being a non-reactive source, the secondary ionisation was found to be principally function of the overall sample porosity and not of the sputtering energy. In the other hand the poor ionising contribution of xenon

make very difficult the analysis of elements present at low concentration in porous samples.

As far as concerns oxygen as sputtering source, it was observed that a material chemical modification occurs during bombardment induced by the oxidising property of this source. This effect has a direct impact on the sputtering rate and on the secondary ion information. Ionisation phenomena depend also by the presence of an oxygen flooding on sample surface. This dependence is observed to be enhanced at low sputtering energy and minimised at high sputtering energies as the oxidation kinetics do not permit a full target oxidation.

The results presented in this chapter evaluated the behaviour of porous silicon samples from a phenomenological and chemical point of view. To complete these results a next step would be better understand the thermo-kinetic behaviour of p-Si under primary ion bombardment. In the specific case of caesium sputtering, it would be of high interest to carry a study to validate the presence of a concentration gradient of reactive primary species in the depth of the porous matter and its energy dependence. Moreover, in terms of sputtering yield, the efficiency of xenon as sputtering source on p-Si could become interesting when coupled with a caesium source in co-sputtering mode. In this mode, the supposed in-depth caesium gradient formation would be limited and acquired in-depth profiles not affected by the observed gradient on silicon signals.

3 CHEMICAL CHARACTERISATION OF POLYMETHACRYLATES THIN FILMS DEPOSITED BY I-CVD

In this chapter, the capabilities of new generation primary ion sources to reduce the target damaging during analysis are explored. The analysed material are deposited by an innovating CVD technique able to deposit a large variety of polymers. The first part of the chapter is dedicated to the depth profiling of a stack of quasi-identical polymers in order to verify if the produced secondary ion information is fine enough to identify the chemical differences between layers. The acquired knowledge on polymer discrimination is used to develop a quantification method for copolymers. The goal is then brought to a more ambitious level trying to discriminate samples characterised by an identical chemistry but different molecular weights in order to validate the high mass detected information by coupling it with multivariate analysis.

3.1 INTRODUCTION

As described in the introduction, the i-CVD technique is an emerging deposition technique in the panorama of polymer deposition methods. The continuous optimisation regarding processes and equipment will make the i-CVD technique more and more applicable to the industrial area. Among the various early applications, the most promising are for gas sensing and insulating layers [6].

At present, many types of polymers have been successfully deposited with this technique such as polyacrylates and polymethacrylates. A precise in-depth

characterisation technique helping to describe the nature of the deposited material in its whole depth is one of the fundamental questions investigated in this chapter.

As described in section 1.1.2.2, the use of ToF-SIMS for in-depth profile chemical characterisation of such polymeric thin films is related to specific experimental conditions, especially when cluster sources are used (section 1.2.2). A relevant chemical information can be obtained in low damaging conditions as the result of a fragmentation of the original molecular chemical composition.

The i-CVD as polymer deposition technique is described and specific aims of this work are carried out.

3.1.1 SHORT INTRODUCTION ON I-CVD TECHNIQUE AND CHEMICAL ISSUES RELATED TO IT

As already stated previously, polymeric thin films are more and more used in the microelectronics industry in applications such as sensing layer for gas and biodetectors or in the energetic industry for solar cells [152] and fuel cells [153] production. Active research in the field of biomedical to increase biocompatibility and in Micro-Electro-Mechanical Systems (MEMS) for microfluid devices brought the research to innovating fabrication processes and materials. Most of the productions of devices integrating polymeric materials are focused on the liquid phase deposition technology by spin-coating. However, solvents can degrade the hosting substrate like paper, textiles and membranes. After production, parasitic strains can influence the properties of produced films and coatings in nanometric sophisticated devices.

Among dry methods, plasma-enhanced chemical vapour deposition is frequently used to form polymer films. However, plasma polymer compositions can deviate significantly from linear polymer stoichiometries due to the extensive cross-linking and loss of chemical functionality during deposition. Recently, initiated chemical vapour deposition (i-CVD) has been demonstrated as a way to produce stoichiometric polymers identical to liquid-phase polymers. This method allows a single-step solvent free polymerization-and-coating of planar as well as three-dimensional substrates [90, 91].

As i-CVD represents a relatively new concept for producing polymer films and coatings, much effort is still needed to help understand structure-property-processing relationships.

3.1.2 I-CVD WORKING PRINCIPLE

Polymer films and coatings made by initiated chemical vapour deposition (i-CVD) are shown to produce well defined polymer compositions, e.g., poly(tetrafluoroethylene), poly- (glycidyl methacrylate), poly(methyl methacrylate) [91]. Mostly, i-CVD can be considered as a free radical polymerization without the use of a liquid phase, conveniently combining polymerization and coating in a single step. The absence of solvents makes this technique unique in the domain of radical polymerisation techniques. It involves the vapour phase delivery of initiator (I) and monomer (M) into a vacuum chamber maintained at a pressure typically between 10^{-4} and 10^{-3} $Torr$. Radicals (R•) are formed by initiator degradation through a thermal activation using filaments heated to a temperature typically in the range of 100 to 400 $°C$. Radicals and monomers are deposited and adsorbed on the chilled substrate kept at a temperature lower than 50 $°C$, to promote adsorption. After monomer adsorption, the polymerisation takes place forming the polymeric film (P) (Figure 3.1).

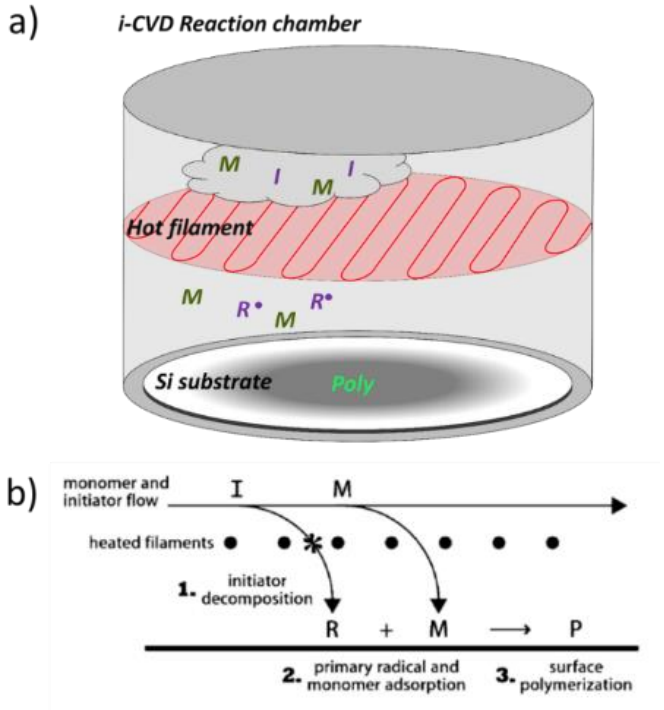

Figure 3.1: a) Schematic representation of the i-CVD reactor and b) the polymerisation steps. Chemical species are injected from the top part of the reactor and pass through the heated filament where initiator degradation is induced. Radicals and monomer are adsorbed on the substrate where polymerisation occurs.

Because the i-CVD method uses initiated radical polymerisation process, a good control of the resulting polymer chemistry is then obtained by controlling the injection of the initiator and the monomer. High retention of original functionalising groups and a

high growth rate [154, 155] are obtained by applying low process temperatures. The i-CVD deposited polymers have a chemical composition quite similar to the one obtained by liquid-phase polymerisation [156] as shown in the Ph.D. work of Bonnet L. [157]. In addition, the deposition of statistical and periodic copolymers can be achieved [158]. Polymers with different surface properties can then be deposited, making this deposition technique an excellent solution among the large varieties of CVD technologies.

Unlike bulk thermal polymerization, i-CVD separates the temperature of initiator decomposition from the temperature of polymerization events. This additional degree of freedom allows a greater degree of control over processing and resulting coating properties. It also provides processing flexibility because a lower substrate temperature could be used to coat heat-sensitive materials such as plastics, fabrics, and pharmaceutics.

3.1.3 QUESTION RELATED TO THIN FILM DEPOSITION

As just said, initiated chemical vapour deposition technique is gaining interest in the industrial field and first semi-industrial reactors appear. Furthermore, the i-CVD technique allows the co-deposition of polymers to create stacks or copolymer materials. In some cases, the deposition of quasi-identical polymers inhibits classical characterisation techniques such as X-Ray Photoelectron Spectroscopy (XPS) to discriminate materials. As extremely thin films (less than 20 nm) can be deposited with this technique, the amount of polymer deposited is then not sufficient to perform classical molecular weight (M_w) characterisations such as Size Exclusion Chromatography (SEC). The access to the molecular weight information is particularly important in general for any produced polymeric material. In this chapter in particular, the access to this information for very thin films is explored.

During ToF-SIMS analysis, the detected chemistry is the result of the different types of fragmentation depending on the energy transferred by the impacting ion and its size. As described in section 1.1.2.2, around the impact zone elemental fragments are produced. Getting far from this zone more polymer-like fragments are emitted. The attention is then focussed on the chemical species produced in low damaging analysis conditions to answer at some particular aspects regarding i-CVD deposited materials such as the identification of characteristic chemical fragments allowing to discriminate between two different types methacrylates. The next step is then an in-depth characterisation of a double-stack of the quasi-identical methacrylates.

A quantification protocol for copolymers is then investigated using intensities of characteristic peaks studied for bulk materials. In the case of identical polymers where only the degree of polymerisation change, very low damaging conditions during analysis are needed because the discrimination is made at high mass fragments. In the case of high polymerisation degrees, the ToF-SIMS technology is not able to detect the entire polymeric chain and the signal detected is a fragmentation of the original one (section 1.1.3.2). The objective is then to limit sample damaging phenomenon to increase the chance to discriminate and quantify methacrylate copolymer samples. However, the complexity of the detected chemical information has to be simplified in an easier one for interpretation. Multivariate analysis methods which have been successfully applied to SIMS data for the discrimination and classification of proteins mixtures or quantification of polymers blend composition [116] are used also in this work.

3.1.4 DEPOSITED POLYMERS

The samples studied were thermally i-CVD (10 to 1500 nm), coatings of poly(neopentyl methacrylate) p(npMa) and poly(ethylhexyl methacrylate) p(ehMa) deposited on a silicon substrate (Figure 3.2). The interest in the production and characterisation of these materials comes from their ability in toluene vapour sensing [159]. In a previous work, J. Grate [160] underlined the close link between the chemical structure of the adsorbing layer and the vapour phase. In the case of toluene, the presence of methyl groups is shown to increase the vapour adsorption.

The initiator was the tertbutyl-peroxide with the labile peroxide group in the middle of the molecule.

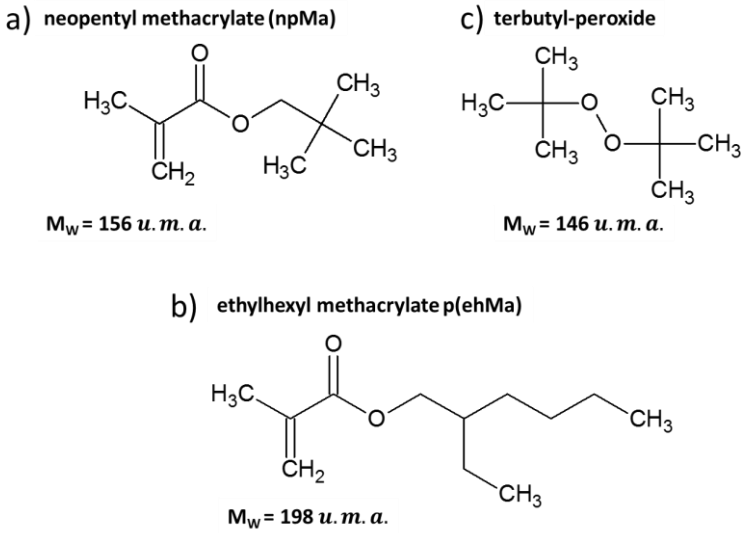

Figure 3.2: Chemical formula of the different molecules studied a) npMa chemical formula $C_9H_{16}O_2$, b) the initiator terbutyl-peroxide $C_8H_{18}O_2$ and c) ehMa chemical formula $C_{12}H_{22}O_2$. The radical reaction is initiated via the thermal breaking of the peroxide group $-O-O-$.The polymerisation occurs with the activation of the $=CH_2$ double bond.

The deposition equipment is a prototype developed and fabricated by Tokyo Electron (TEL).

The possibility to obtain copolymers through the co-deposition of monomers described previously was explored. The copolymers were synthetised by co-injecting both monomers and initiator to perform a p(npMa-co-ehMa) copolymer. At present, the presence of a deposited material on the surface of an organic soft material (oligomer or polymer) has been observed by Atomic Force Microscopy (AFM), ellipsometry and FTIR but the molecular properties such as polymerization degree of the deposited films are still difficult to access.

It has been shown that films with a varying molecular weight can be deposited by adjusting process parameters [157] and a sample set with a varying molecular weight (M_w), was analysed in spectra mode. Actually, the observed data trend is potentially fruitful for the interpretation of the fragmentation mechanisms occurring under SIMS primary ion bombardment as a function of the polymerisation degree.

3.2 DEPTH PROFILING OF MONO AND MULTILAYER MATERIALS

In this section, the discrimination between two polymers with a very similar chemistry is investigated through SIMS data analysis. The materials chosen for this study are i-CVD deposited layer of p(npMa) and a double layer p(ehMa)/p(npMa). The choice of analysis condition able to preserve the chemical information is a major step in this work.

3.2.1 SELECTION OF SPECTRAL ANALYTICAL CONDITIONS

Before proceeding to the in-depth characterisation of p(npMa) and the double-layer p(npMa)/p(ehMa), the ideal setting concerning analysis gun has to be evaluated to obtain high mass resolution and low sample damaging. To do so, a 70 nm p(npMa) was taken as experimental sample and two bismuth analysis settings Bi_1^+ or Bi_3^+ at 15 keV were explored acquiring spectra with the identical ion dose ($7 * 10^{13}\ ions/cm^2$) for each setting.

In Figure 3.3 the two corresponding spectra are plotted in a mass range between 105-110 amu. It must be stated that these results are fully representative of the general behaviour of the entire mass spectra. The Bi_3^+ setting has lower current and a lower impact energy per atom on target relating to Bi_1^+ and ten times longer analysis are needed for Bi_3^+ to achieve the same dose as Bi_1^+. However, monoatomic bismuth primary ions penetrate more into the sample depth, decreasing the number of secondary ions ejected and increasing the subsequent bound breaks [13]. As a consequence, Bi_3^+ ions result to be the best compromise between high mass resolution and low sample damaging. Bi_3^+ setting will be used for the further in-depth profile study.

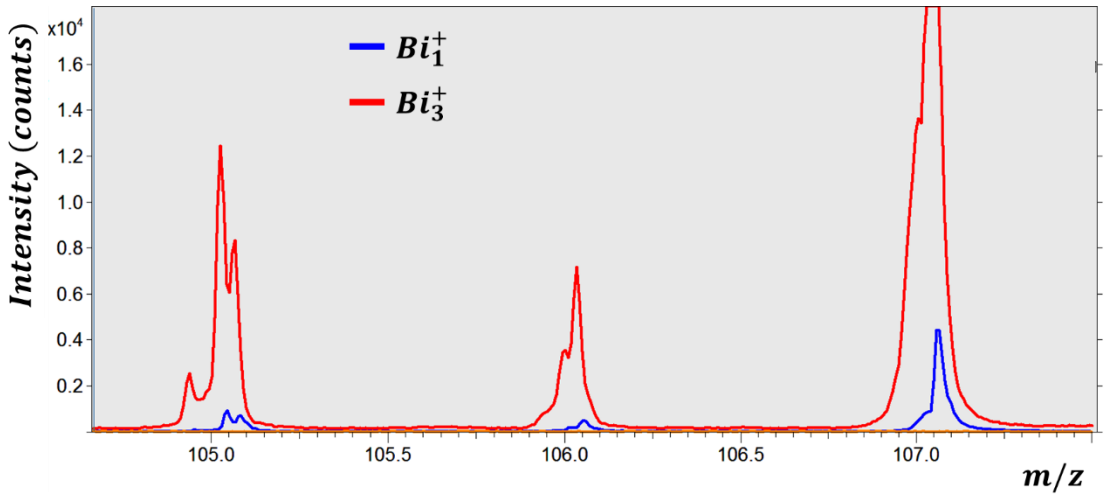

Figure 3.3: Overlap of 70 nm p(npMa) spectra obtained at 15 keV bismuth primary ion bombardments. The red curve corresponds to the Bi_3^+: high-resolution mass can be observed and high intensities are registered. Blue curve corresponded to Bi_1 setting: in this case the mass resolution is still high but lower intensities are recorded.

The application of GCIB as analysis primary source was also explored. The analysis setting was obtained adapting an existing sputtering one. The choice of a high energy setting was made because the possibility to ionise the sputtered secondary species is higher. Also, the selection of reduced cluster size is made in order to increase the energy per atom (Ar_{1000} 20 keV). In Figure 3.4 argon and bismuth spectra are compared. Argon intensities are lower compared to bismuth, this behaviour is observed on each peak in the entire spectra. The expected advantage to obtain high fragment ions using GCIB as analysis source is weakened by the low intense signal and most of all by the low mass resolution as shown in Figure 3.4.

The main reason for the low mass resolution comes from the fact that it is not possible to obtain a bunched primary flux with this source. It is important to remind that GCIB source produces a distribution of clusters around a given size. As a consequence, while impacting on the sample for secondary ion generation, generated ions will have a broad distribution of kinetic energies (corrected by the "reflectron") and a larger emission time. With bismuth instead, the possibility of bunching the ion flux reduces the pulse length leading to a better mass resolution. Useful chemical information is then masked using argon as analysis source. The fact of being a low damaging source makes it still an ideal source for sputtering.

The common settings then used for the depth profiling of i-CVD methacrylate layers are:

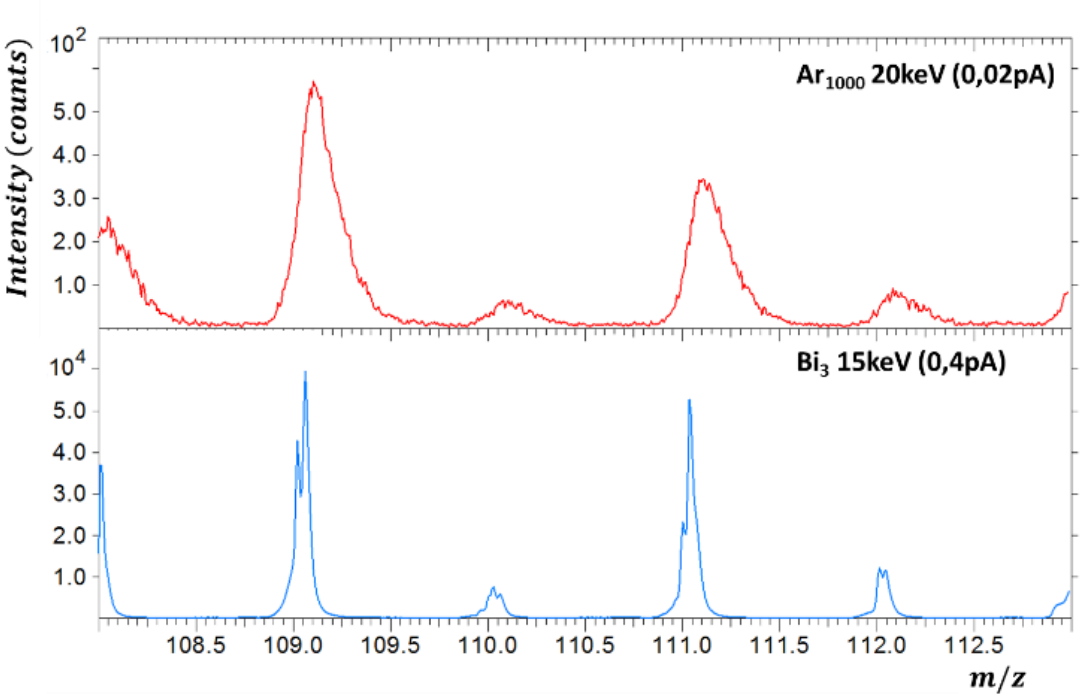

Figure 3.4: Mass spectra comparison between Ar_{1000} 20keV (0.02pA) (red spectrum) and Bi_3 15enV (0.4pA) (blue spectrum) of p(npMa) sample deposited by i-CVD. Low mass resolution in argon analysis does not permit the distinction between nearby peaks and peaks intensities are 10^2 lower compared to bismuth.

- Analysis gun: Bi_3^+ - 15 keV at 0.40 pA raster 500x500 µm^2
- Sputter gun: Ar_{2500}^+ - 5 keV at 0.40 nA raster 700x700 µm^2
- Cycle time: 205 µs with a corresponding mass detection range (0-4000 amu) in negative polarity.
- No flood gun for charge compensation.

Analysis raster was set at 500x500 µm^2 in order to reduce the probability that multiple bismuth shots hit the same zone. The main effect is to reduce the sample damaging produced by energetic primary ions. Regarding the cycle time, the value of 205 µs is not exceeded because generated fragments up to 4000 amu would not be intense enough to be representative.

During spectra analysis, the acquisition time is set to 300 s as it is a good compromise in terms of ion counting and reasonable acquisition time. Considering the current of bismuth gun, the ion dose density is kept at $3.5x10^{11}$ $ions/cm^2$, value under the static threshold ($1x10^{12}$ $ions/cm^2$) for inorganic and organic materials.

3.2.2 DEPTH PROFILING OF POLY(NEOPENTYL METHACRYLATE)

CHOICE OF THE CHARACTERISTIC PEAKS

Fragmentation of poly(neopentyl methacrylate) under primary analysis ion beam produces a huge quantity of peaks. Considering spectra mass region between 0 and 250 mass atomic units (Figure 3.5) obtained on a sample 70 nm thick, a selection of the most intense was made proceeding then to the recognition.

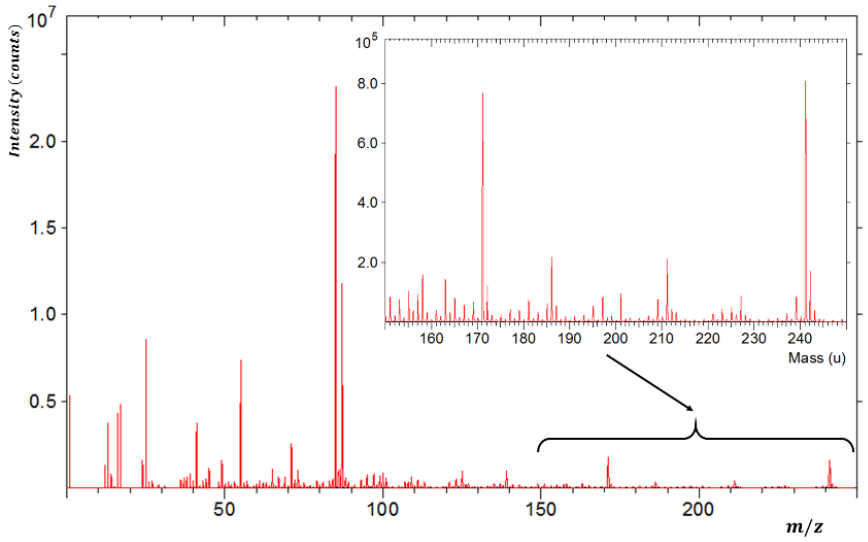

Figure 3.5: Mass spectra Bi_3 15keV (0.4pA) of the i-CVD 70 nm p(npMa) sample.

The first two zones of fragmentation theorised in the works of Benninghoven *et al.* [20] for organic materials can be clearly distinguished (section 1.1.2.2): the "impact region" providing a damaged low mass chemical information connected to basic chemical structure of the organic materials (between 0-100 amu); the "finger-print region", characterised by fragments generated by the post-recombination between two or more repeating units (up to 100 amu). Zooming between 150 and 250 amu, regular groups of peaks are observed indicating the beginning of the "oligomer mass region", zone containing information about the polymerisation degree. In this case, the goal is to look for the characteristic signature of the analysed polymer. The attention is then focussed on the most intense peaks placed in the so called "impact region and finger-print zone", peaks are listed in Table 3.1 and illustrated in Figure 3.6.

The first two fragments are characteristic of the neopentyl group linked with an oxygen atom acquired during fragmentation of the methacrylate. The entire repeating unit of npMa can be detected as a product of the fragmentation of the polymeric chain. In other cases, during fragmentation, the repeating unit can be bonded with another methyl group

Table 3.1: List of the most intense peaks in p(npMa) spectrum. Formula are proposed for each peak.

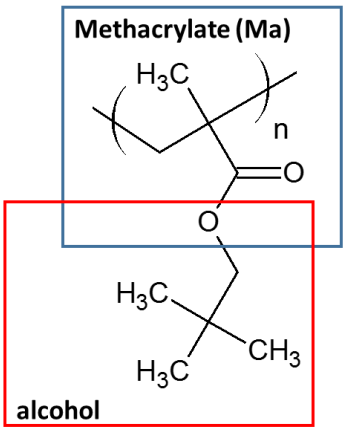

Peaks (u.m.a.)	Formula	Molecule fragment
85	$C_5H_9O^-$	Alcohol groups
87	$C_5H_{11}O^-$	
156	$C_9H_{16}O_2^-$	npMa
171	$C_{10}H_{19}O_2^-$	npMa+methyl
241	$C_{13}H_{21}O_4^-$	npMa+Ma

Figure 3.6: Poly(neopentyl methacrylate) p(npMa) chemical structure. Blue and red square represent typical fragments of the original molecule.

deriving from the one next to it. The 241 amu peak is the combination of a repeating unit with another one that has lost its neopentyl group ($C_5\ H_{11}O^-$). To consider these peaks characteristic of the studied polymer, they should be particularly intense in a depth profile. Their stability in depth is also an important marker as it describes if in-depth chemical composition of samples is constant. This information is extremely important as it confirms that the deposition process is able to produce bulk samples with a constant chemical composition in-depth.

DEPTH PROFILING

Figure 3.7 represent the in-depth intensities of previously selected peaks of the p(npMa) 70 nm thick sample. All the characteristic peaks of the polymer fragmentation in Table 3.1 have a flat in-depth trend. In conclusion, the film appears homogeneous in depth and during analysis there is not the presence of damage accumulation due to the high energetic analysis beam. The interface presence is underlined by the silicon ion.

3.2.3 DEPTH PROFILING OF DOUBLE LAYER POLY(ETHYLHEXYL METHACRYLATE)/ POLY(NEOPENTYL METHACRYLATE)

In this section, a double layer p(ehMa)/p(npMa) is examined in depth with the objective to discriminate the two polymers. Depth profiling of organic layers has already been performed on organic-LED structures [77] or reference samples such as Irganox [98]. In these examples, the chemical composition differed considerably for each layer of

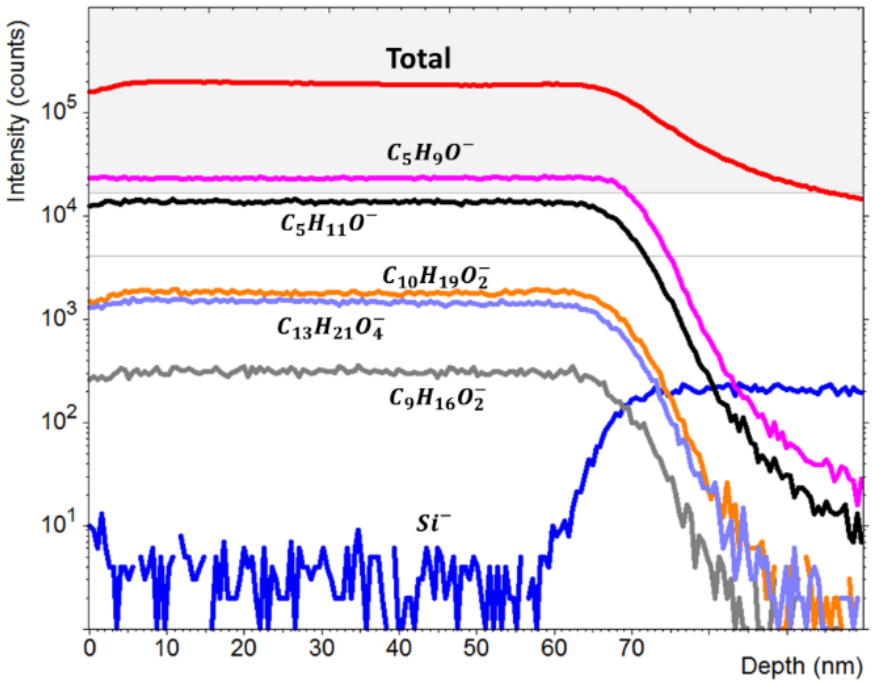

Figure 3.7: poly(neopentyl methacrylate) p(npMa) 70 nm in-depth profile representing the most intense peaks coming from the fragmentation under Bi_3^+ 15 keV (0.4 pA) flux. Sputtering source Ar_{2500}^+ (0.4 nA).

the stack. As a consequence, the choice of characteristic peaks was of limited interest. In the subject developed here, greater importance is given to the selection of characteristic peaks discriminating each layer. This is why before proceeding to the in-depth study of the double layer, a spectral analysis is performed on the poly(ethylhexyl methacrylate) film.

CHOICE OF POLY(ETHYLHEXYL METHACRYLATE) CHARACTERISTIC PEAKS

The most intense peaks are selected from the spectra (Figure 3.8) and a fragment recognition is applied to compare the p(ehMa) fingerprint with the one of p(npMa).

In Table 3.2 the first two fragments (127 and 129 amu) are characteristic of the ethylhexyl group linked with an oxygen atom acquired during fragmentation of the methacrylate group. The entire repeating unit of ehMa can be detected as product of the fragmentation of the polymeric chain (199 amu). In other cases, during fragmentation, the repeating unit can be bonded to another methyl group coming from the one next to it, while peak at 381 amu is the combination of two repeating units (not presented in Figure 3.8).

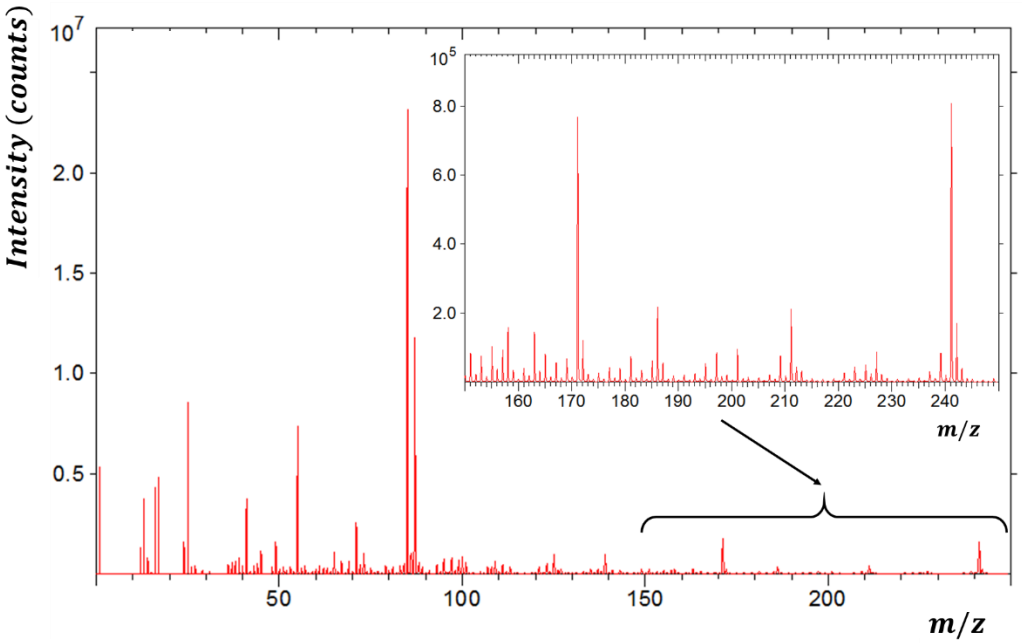

Figure 3.8: Mass spectra Bi_3^+ 15 keV (0.4pA) of the i-CVD deposited p(ehMa) sample.

According to the study performed on the poly(neopentyl methacrylate) revealing the alcohol group as the characteristic peak (87 *amu*), in the case of poly(ethylhexyl methacrylate), 129 *amu* peak is identified to be the characteristic one.

This discrimination has been possible thanks to the low damaging analysis conditions applied. This result fits well with previous works by Houssiau *et al.* where the characteristic peak of methacrylates corresponded to the alcohol fragment [58].

Table 3.2: List of the most intense peaks in p(ehMa) spectrum. Formula are proposed for each peak and the parallel with the molecular fragment is made.

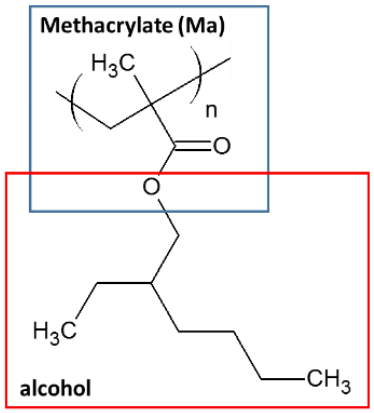

Peaks (u.m.a.)	Formula	Molecule fragment
127	$C_8H_{15}O^-$	Alcohol groups
129	$C_8H_{17}O^-$	
199	$C_{12}H_{23}O_2^-$	ehMa
213	$C_{13}H_{25}O_2^-$	ehMa+methyl
239	$C_{15}H_{27}O_2^-$	ehMa+methyl(x2)
381	$C_{23}H_{41}O_4^-$	ehMa(x2)

Figure 3.9: Poly(ethylhexyl methacrylate) p(ehMa) chemical structure. Blue and red square represent typical fragments of the original molecule.

DEPTH PROFILING

The results linked to the identification steps of characteristic peaks of similar polymers are now applied to a double stack sample. A 30 nm of p(npMa) sample was first grown on a native oxide silicon substrate to assure the adhesion of the 200 nm p(ehMa) film.

In Figure 3.10-a, the depth profile of this double layer is plotted. The two layers can be clearly distinguished and the presence of the silicon interface is determined by the appearance of SiO_2^- signal. However, when observing the trend of the characteristic peaks, it can be noticed that they are not as unique as they were thought to be. In particular the alcohol radical ion $C_5H_{11}O^-$ (87 amu) associated to p(npMa), is found to be also a product of the fragmentation of p(ehMa).

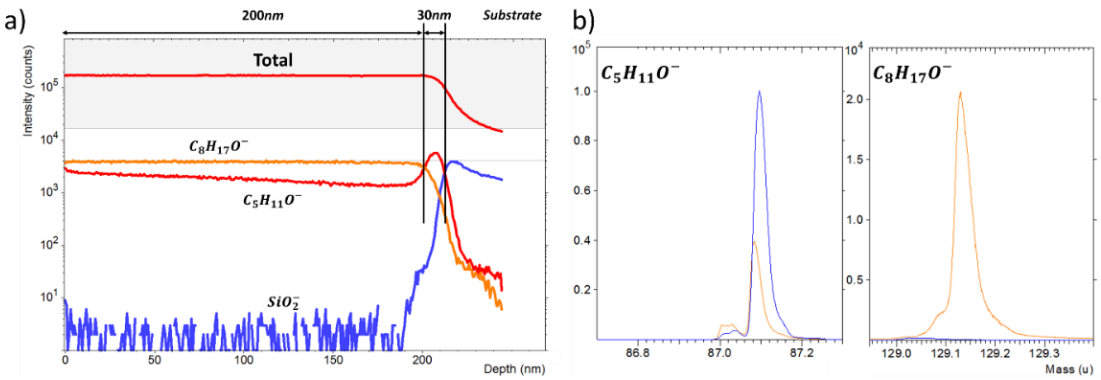

Figure 3.10 : a) In-depth profile of p(npMa)/p(ehMa) double layer representing the most intense peaks coming from the fragmentation under 15keV Bi_3 (0.4 pA). Sputtering source Ar_{2500} (0.4 nA). b) $C_5H_{11}O^-$ characteristic peak of the p(npMa) (blue curve) is also a product of the fragmentation of p(ehMa) (orange curve). $C_8H_{17}O^-$ appears only in p(ehMa) spectrum and it is absent in p(npMa).

Apparently, as the ethylhexyl methacrylate has a similar but bigger chemical structure, an isomer equal in mass to a neopentyl methacrylate fragment is generated during fragmentation but with a different chemical configuration. It is true that the opposite situation has a lower possibility to take place. Indeed, in the p(npMa) layer the signal characteristic of p(ehMa) decreases rapidly. The discrimination between the two layers is still possible but for future characterisations this aspect has to be kept in mind. This phenomenon is particularly important if the objectives are related to the development of a quantification method. In Figure 3.10-b, it can be clearly seen the presence of the peak $C_5H_{11}O^-$ in both polymers. Contrariwise, $C_8H_{17}O^-$ peak does not appear in p(npMa) spectrum confirming the theory stated before. To confirm these observations, other intense peaks associated to ehMa (not shown in this work) have been plotted in depth to

check if the in-depth study performed is appropriate. The characteristic peaks described in the previous tables express the same trend with an average intensity twenty times lower.

In conclusion, the possibility to discriminate polymers with very analogous chemical structures by reducing damaging analysis conditions has been demonstrated.

3.3 CHARACTERISATION OF I-CVD DEPOSITED METHACRYLATE COPOLYMERS

The possibility to deposit multiple monomers at the same time by i-CVD has been investigated. In this paragraph, p(npMa)/p(ehMa) co-polymer composition is characterised.

Classical techniques like X-ray Photoelectron Spectroscopy (XPS) commonly used for copolymer quantification are not useful in this case due to the similarities in the chemistry of the repeating units and the co-polymer ratio is unknown. For this reason, a ToF-SIMS quantification method using the characteristic peaks detected in previous sections is investigated (section 3.2.3). The idea is to compare intensities of $C_5H_{11}O^+$ and $C_8H_{17}O^+$ peaks characteristic of p(npMa) and p(ehMa) respectively. By this method, it is assumed that between a reference polymer and a co-polymer, the absence or a very limited presence of matrix effects take place due to the similarities of the two repeating units.

3.3.1 EXPERIMENTAL CONDITIONS

The characterised sample set is composed of two i-CVD copolymer thin films ($\sim 20\ nm$) deposited on a silicon substrate with a native silicon oxide layer called "Co-po1" and "Co-po2". These films were the result of a simultaneous co-deposition of the two monomers and the initiator. The reference samples correspond to the ones used for the characteristic peak selection in section 3.2. A pre-sputtering of 15 seconds using a GCIB Ar_{2500} 5keV (0.4 nA) to clean the sample surface from any polluting species was performed (see next section about how this pre-sputtering conditions were chosen). The pre-sputtering was followed by surface spectra acquisition in static mode using a bunched Bi_3^+ ion flux accelerated at 15 keV (0.4 pA) for 300 s with a cycle time of 205 μs. After a careful mass calibration, p(npMa) and p(ehMa) peak areas were tabulated. Total intensity of the spectra, representing the sum of all peak intensities, was also taken into account for normalisation purposes.

3.3.2 ToF-SIMS CO-POLYMER QUANTIFICATION

The idea is to compare intensities of $C_5H_{11}O^+$ (87 amu) and $C_8H_{17}O^+$ (129 amu) peaks characteristic of p(npMa) and p(ehMa) respectively as shown in section 3.2.3 to establish a quantification method. In Table 3.3 the starting values used for the quantification protocol are reported.

Supposing Y as the percentage of p(ehMa) in the co-polymer, $1-Y$ will be the p(npMa) one. At first, all peak intensities are normalised by the total intensity in the spectra. The quantity of p(ehMa) Y is then calculated dividing the normalised intensity of p(ehMa) of each sample by the value in the p(ehMa) reference.

A complementary method for quantification has been developed using FT-IR analysis performed on the same samples. The results are shown in Appendix 2: FT-IR. The results obtained by both techniques are in good agreement and a major presence of p(npMa) as illustrated in Table 3.4.

Table 3.3: $C_5H_{11}O^-$ and $C_8H_{17}O^-$ peak areas of ToF-SIMS analysed copolymer samples. Total label correspond to the total not saturating ions hitting the detector.

	$p(ehMa)$	$p(npMa)$	$\boldsymbol{Co-po1}$	$\boldsymbol{Co-po2}$
$C_5H_{11}O^-$	$1{,}21x10^{06} \pm 5\%$	$3{,}46x10^{06} \pm 5\%$	$3{,}90x10^{06} \pm 5\%$	$4{,}36x10^{06} \pm 5\%$
$C_8H_{17}O^-$	$1{,}41x10^{06} \pm 5\%$	$6{,}92x10^{03} \pm 6\%$	$1{,}52x10^{05} \pm 5\%$	$1{,}80x10^{05} \pm 5\%$
$Total$	$6{,}20x10^{07} \pm 5\%$	$5{,}09x10^{07} \pm 5\%$	$5{,}73x10^{07} \pm 5\%$	$6{,}38x10^{07} \pm 5\%$
$C_8H_{17}O^-$ $normalised$	$0{,}0227 \pm 10\%$	$0{,}0001 \pm 11\%$	$0{,}0027 \pm 10\%$	$0{,}0028 \pm 10\%$
Y	1	0	$0{,}11 \pm 0.02$	$0{,}12 \pm 0.02$
$\boldsymbol{1-Y}$	**0**	**1**	$\mathbf{0.89} \pm 0.02$	$\mathbf{0.88} \pm 0.02$

This study shows that it is possible to quantify by ToF-SIMS blends of copolymers with a very similar chemical structure. In the future, to further confirm the validity of this protocol, anew sample sets with a larger range of p(npMa)/p(ehMa) ratios should be characterised.

Table 3.4: Comparison between FT-IR and ToF-SIMS quantification results.

	p(ehMa)	p(npMa)	$\boldsymbol{Co-po1}$	$\boldsymbol{Co-po2}$
$\boldsymbol{FTIR}$	0	1	0.90	0.87
$\boldsymbol{ToF-SIMS}$	0	1	0.89	0.88

3.4 CHARACTERISATION OF M_w VARYING SAMPLES BY SPUTTER RATE AND SPECTRA STUDY

The achieved knowledge in the discrimination between similar polymers in the previous section is now brought to a more challenging level. In this case, discrimination between identical i-CVD polymers with varying molecular weight is investigated.

The molecular weight of the samples was measured by size exclusion chromatography (SEC) and are reported in Table 3.5.

Table 3.5: Complete sample set of p(npMa) thin films deposited by i-CVD with a varying M_w and the relative thickness.

M_w (g/mol)	$Thickness$ (nm)
1500	15
2000	30
15000	70
17000	210
18000	350
22000	1500

In order to investigate the M_w variation by SIMS, a spectral analysis is performed on samples. The same analysis conditions used in the previous section characterised by a reduced sample damaging and the intense signal at high masses up to 3000 amu are used for this kind of purpose.

For this investigation, the attention was focussed on the chemical information produced at high masses in the so called "oligomer region". In this zone, the fragmented chemistry is expected to better describe the sample polymerisation degree. However, in order to consider representative spectral information, surface contamination of samples has also to be considered. Indeed, the airborne contamination of surfaces is a well-known phenomenon capable to influence the secondary ion mass information collected [161]. This contribution has to be eliminated by sputtering to a chosen depth before spectra acquisition in order to perform an accurate and representative bulk spectra characterisation.

3.4.1 SPUTTER RATE VARIATION WITH MOLECULAR WEIGHT

Molecular weight has an impact on the sputter rate for organic materials as described in section 1.2.2. Therefore, the pre-sputtering conditions are not unique for the whole sample set.

In Figure 3.11 sputter rates of a part of sample set are plotted as a function of their molecular weight. It can be noticed that a fast decrease of rates for low polymerisation degrees is followed by a stabilisation around 0.3 nm/s for molecular weights higher than 2500 g/mol. This low sputter rate indicates that the depth profiling of thicker samples would be really time consuming. For high M_w, the sputter rate of non-analysed samples (18 and 22 kg/mol) are then predicted by fitting.

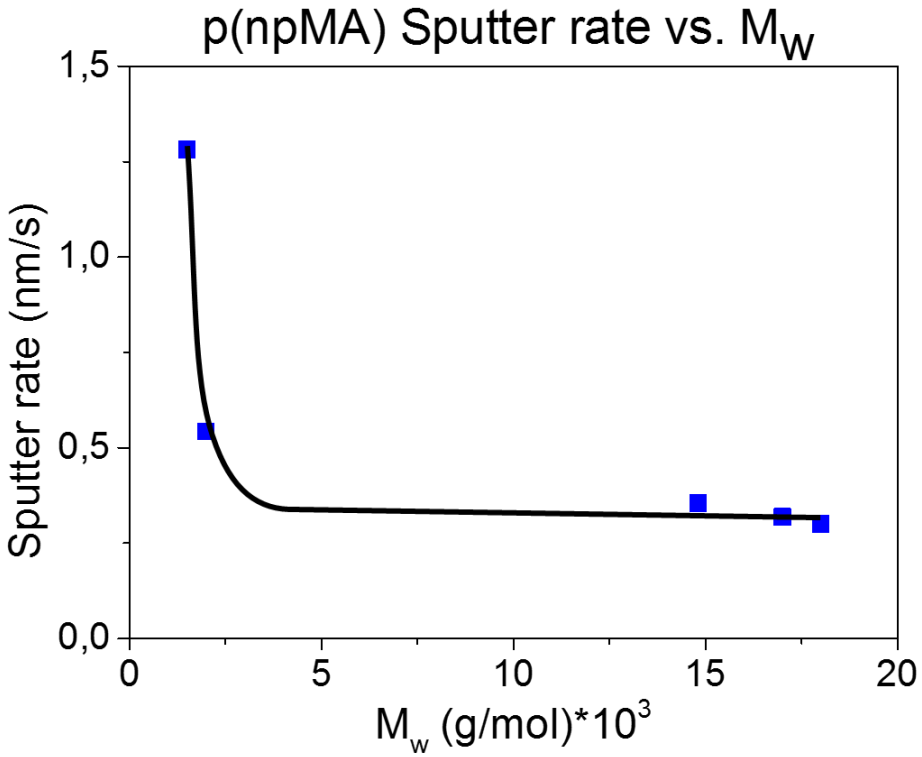

Figure 3.11: Sputter rates vs. molecular weight measured for p(npMa) samples by in-depth profiles ToF-SIMS cluster argon sputtering. Sputtering setting: Ar^+_{2500} at 5 ke, 0.4 nA

This preliminary study shows the importance of the M_w on the sputter rate of methacrylates films. Ideally, for future characterisations, once the sputtering speed at a given M_w is known, it will be possible to skip all the pre-sputtering study gaining much time. In this case, it should be interesting to develop a database of materials with the corresponding sputter curve as in Figure 3.11. At present only the work of Cristaudo *et*

al. has underlined experimentally this aspect on polystyrene and poly(methyl methacrylate) polymers [100].

As explained in section 1.2.2, this phenomenon is directly related to the volume concentration of chain terminations. For ionisation mechanisms as well, the molecular weight variation is thought to play a crucial role in the fragmentation and ionisation mechanisms as investigated in the next sections.

3.4.2 IDENTIFICATION OF THE DEPTH OF INTEREST

In order to resolve the problem of the polymer surface contamination, a designed pre-sputtering process is applied to the sample surface before spectra acquisition. Pre-sputtering is done using the same GCIB setting used for previous depth profiling.

To evaluate surface contamination responsible for distorted chemical spectrum, the in-depth characteristic peak $C_5H_{11}O^-$ intensity of the p(npMa) is considered. On the other hand, cluster bismuth implantation during bombardment involves an important in-depth damaged zone. If the pre-sputtering is too aggressive, a part of the sputtered ions can come from the interface. As the intention is to avoid this phenomenon, an "appropriate zone" has to be defined for future spectra acquisitions. The optimisation of pre-sputtering settings is performed on the thinner 15 nm sample being the most exposed to noisy surface and interface chemical information.

In Figure 3.12 the measured intensities of Si^- and $C_5H_{11}O^-$ ions vs. pre-sputtering scans are plotted. One GCIB scan corresponds to a defined time that is fixed by the ToF-SIMS manufacturer of 1.4628 seconds to raster an entire area independently from the raster size. It is observed that in the left zone of the diagram, a reduced polymer signal intensity ($C_5H_{11}O^-$) is observed, consistent to the presence of polluting impurities in surface incorporated during sample storing in ambient conditions. In the right part of the figure, polymer signals lightly decrease and silicon signal arises. The limit is at 36 GCIB scans where the whole polymer film was sputtered and silicon signal reaches its maximum. The "appropriate zone" finds its place in between these two regions. In this zone, the polymer signal is representative of the sample bulk and it is ideal for a spectra analysis coupled with multivariate analysis.

The values of sputter rate plotted in Figure 3.11 are used to calculate the ideal pre-sputtering protocol for the entire sample set. As the safe zone on the 15 nm sample is set between 4-6 manometers ($sputtered_{depth}$), the ideal number of scan has to be included between this range as shown in Eq.3.1.

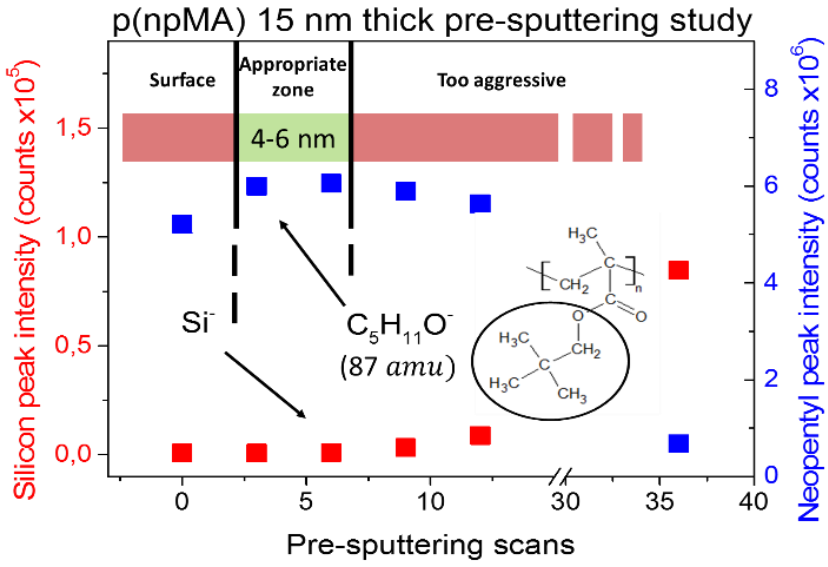

Figure 3.12: Intensities of silicon (red dots) and p(npMa) characteristic peak $C_5H_{11}O^-$ (87 amu) vs. argon sputtering scans for a 15nm sample.

$$n_{scans} = sputtered_{depth}/(sputter_{rate} * 1.4628) \qquad Eq.3.1$$

By this equation, the number of argon sputtering scans is included between 3 scans for the sample with the lowest M_w up to 16 for the most polymerised one.

After applying the defined pre-sputtering protocols to the sample set, the attention is focussed to validate if the ToF-SIMS analysis can reveal M_w variations.

3.4.3 Spectra and principal component analysis: results and discussion

Just after pre-sputtering, four spectra of 300 s each were acquired for each sample in order to have an acceptable statistical data set needed for principal component analysis.

A selection of 1760 peaks was performed followed by a pre-treatment process. As the choice of data pre-treatment conditions is an important part of the whole multivariate analysis process, normalisation to selected peaks and square root coupled to mean centring are applied. This operation is performed in order to minimise the data variations due to user bias and undesired variations of primary ion currents during analysis. The data matrix ready for the statistical analysis is then treated and plotted in MATLAB (The MathWorks, Natick, MA, USA) by using the code developed by D. Graham: nb-toolbox NESAC/BIO.

At this point, Scores and Loadings of the Principal Component 1 ($PC1$) are plotted in Figure 3.13. A clear discrimination between low and high molecular weights is observed. In particular samples with a M_w respectively of 1500 and 2000 g/mol occupy the negative part of Score plot, while the rest of the samples (higher molecular weights) is placed in the neutral and positive zone. Each group of samples is well discriminated one from the others.

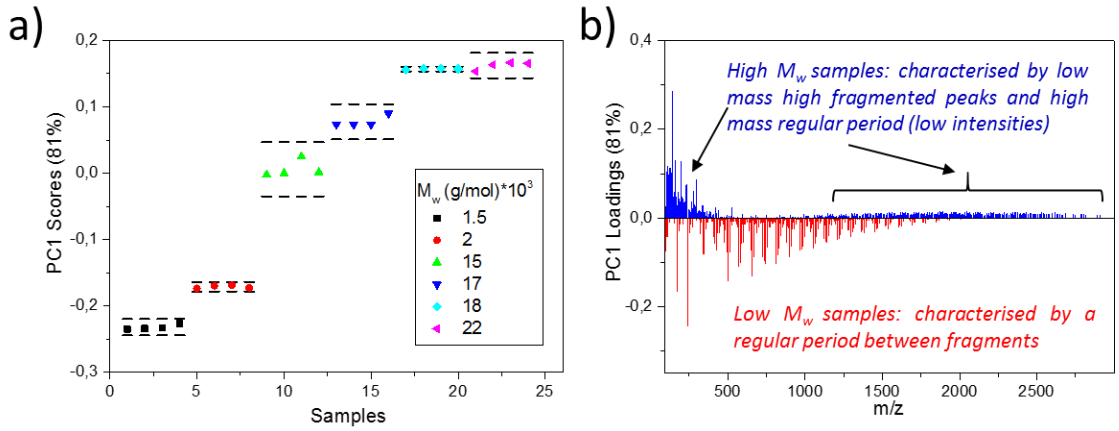

Figure 3.13: First Principal Component a) Scores and b) Loadings plot of ToF-SIMS mass spectra acquired for the sample set, after adapted pre-sputtering. The corresponding negative loadings are characterised by the regular period between fragments. Positive scores describe highly polymerised films. In this case, positive loadings are marked by low mass fragments peaks and low intensity very high mass fragment.

Moreover, additional information can be obtained observing the PC1 loadings in Figure 3.13-b. Negative loadings refer to low M_w samples; these samples are characterised by a high number of polymer chains per volume unit. The resulting spectra are the sum of Bi_3^+ shots coming from a wide number of macromolecules. This make the detected spectrum less fragmented and more similar to the real chemistry of the sample. In fact, negative characteristic peaks have a range comparable to the M_w of the samples it describes (1,5 and 2 kg/mol). These samples are the only ones where their M_w is lower than the detection limit imposed by the cycle time (205 μs). As a consequence, the detected chemical information of the other samples (high M_w) will be much more fragmented. Positive loadings confirm this trend. In this case the number of polymer chains per volume unity is lower due to their higher length. Multiple Bi_3^+ shots are accumulated on the same molecules repeatedly increasing damage. The resulting spectra is further fragmented explaining the presence of characteristic low mass peaks in positive loadings. In negative loadings, it has been observed the presence of characteristic

fragments describing a regular pattern. This pattern describe a regular period between fragments corresponding to entire multiples of the repeating unit with or without the alcoxyl group ($C_5H_{11}O^-$).

$$\left(monomer_{weight}\right)_n \pm \left(C_5H_{11}O^-{}_{weight}\right)_m$$

$$(158\ amu)_n \pm (87amu)_m$$

In conclusion during the analysis bombardment, high mass regular fragments are analysed for low M_w samples while in the opposite case low mass fragments are more intense. This behaviour is observed for positive loadings too but the intensities of the periodic fragments are not strong enough to be useful for sample discrimination. However, their presence confirms the low fragmenting properties of the sputtering protocol used.

In Figure 3.14 the link between $PC1$ scores and molecular weight is established. Each point corresponds to the arithmetic mean of the scores values owing to each group of samples. The data trends are described by an increasing trend indicating a significant relationship between M_w and $PC1$ scores.

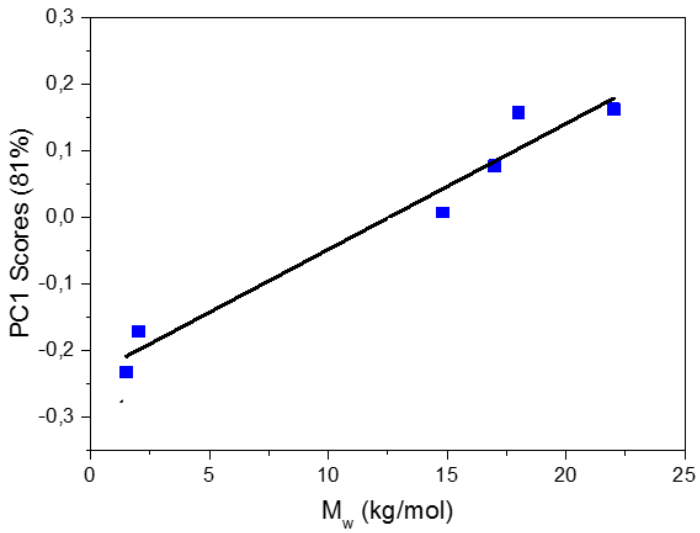

Figure 3.14: PC1 Arithmetic mean vs. molecular weight of studied samples (correlation coefficient R^2=0.95).

This result is an important marker of the relationship between matter fragmentation and polymer molecular mass. Here it is shown that a semi-quantitative technique such as ToF-SIMS can be successfully applied for the discrimination of identical polymers with a varying molecular weight. It has been demonstrated that the molecular weight has an

impact on the generated secondary ion information and not only on physical aspects such as the sputtering yield. Different analysis conditions should be investigated to study the reproducibility of this protocol on a wider selection of molecular weights.

3.5 CONCLUSION AND PERSPECTIVES

In this chapter, the ability of new generation primary ion sources to reduce the sample damaging during analysis and obtain a rich secondary ion information were explored for the characterisation of thin methacrylate films deposited by an innovative CVD technique.

The capability to depth profiling organic samples using large argon clusters allowed to profile stack samples composed of thin layers with a quasi-identical chemistry. This goal was achieved by the recognition of fragments characteristic of each polymer thanks to the reduced sample damaging. This work served also to develop a quantification method for co-polymers based on the relative change of intensities between the identified characteristic peaks and results are consistent with FT-IR measurements. To complete this study a large range of copolymers have to be deposited and analysed to validate the proposed approach.

In addition, ToF-SIMS was also applied for the characterisation of samples of different molecular weights but with the same chemical composition. It was shown that after applying appropriate analysis conditions it was possible to discriminate samples chemistry and rely it to the M_w variations by coupling acquired spectra to multivariate analysis methods. A linear relationship was established between principal component scores and M_w. The obtained result is promising because it allows the characterisation of extremely thin organic layers relying the fragmented detected information to properties such as polymerisation degrees.

The results obtained for i-CVD deposited methacrylate polymers regarding M_w discrimination can be an important starting point for the successful M_w discrimination of a wider selection of linear polymers.

4 CHARACTERISATION AND LOCALISATION OF CHEMICAL MODIFICATIONS ON INDUSTRIAL LOW-K MATERIALS

This chapter is dedicated to the analysis of dielectric materials integrated into industrial microelectronic devices. The intent is to depth profile these materials at different integration steps, in order to be able to access the surface chemical information in the case of different integration treatments affecting the dielectric constant.

4.1 MOTIVATION

4.1.1 LOW-K MATERIALS FOR INTEGRATED CIRCUITS

Integrated circuits are devices composed of transistors acting as switches depending if a current passes or not between the source and the drain as a function of the tension applied to the gate (Figure 4.1-a). Coupling four transistors, it is then possible to create the so-called logical ports to perform logical operations (AND, OR, NAND, etc…). Increasing the number of logic ports, more complex operations can be performed. To achieve this goal, multiple interconnections on several levels are designed. Nowadays, a standard computer chip, as typically found in a computer, can contain one billion of transistors. The Figure 4.1-b, acquired by scanning electron microscopy, shows an integrated circuit type 28 nm (channel distance between source and drain "L"). In this figure three zones can be identified: at first the transistors fabricated directly on a semi-conductor doped (n and p) substrate; this zone is called "front-end of the line" (FEOL). Then, copper interconnections insulated by low-k materials compose the "back-end of the

line" (BEOL). Finally the top coat in aluminium is found assuring the connection to the exterior of the device.

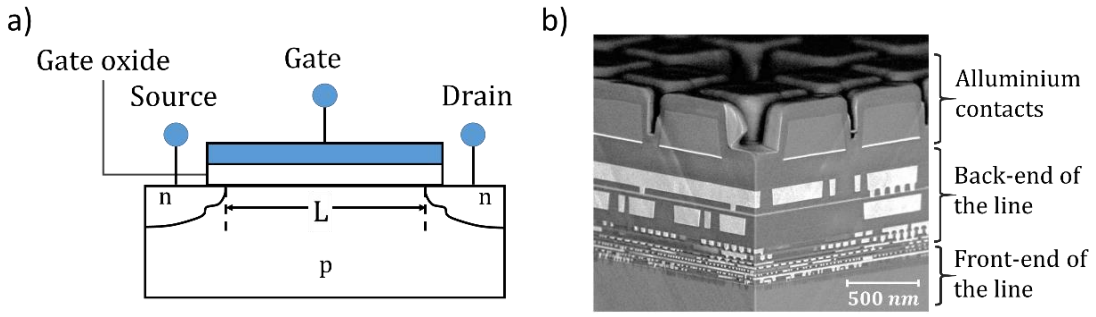

Figure 4.1: a) transistor working principle and b) SEM cross-section image of a 28 nm chip (STMicroelectronics source).

To increase further the number of transistors and as a goal the device performances, miniaturisation is the awarding strategy. Unfortunately, new problems arise, mainly linked to a delay slowing signal propagation: this delay time is due to commutation time of the transistors (switch ON/OFF) and the migration of electrons through the interconnections. Considering the insulating intermetallic materials, at first, silicon dioxide was used (k=4.2) but soon its dielectric properties were not good enough for miniaturisation needs. Replacing SiO_2 was not an easy process and major effort in materials design and engineering was carried out. In principle, any material with a dielectric constant k lower than 4.2 (k of SiO_2) was source of interest, introducing a new generation of insulators, the so called low-k dielectrics.

Among the possible ways of reducing dielectric constant, decreasing dipole strength or the number of dipoles are the most explored ways. This means using materials with chemical bonds of lower polarizability than $Si-O$ or lower density materials. The two methods can be combined to achieve even lower k values. The IC industry has already moved to low-k materials, where some silica $Si-O$ bonds have been replaced with less polar $Si-F$ or $Si-C$ bonds. A more fundamental reduction can be achieved by using virtually all non-polar bonds, such as $C-C$ or $C-H$, for example, in materials like organic polymers (for more details see [162]).

The density of a material can be reduced by increasing the free volume through rearranging the material structure, i.e. introducing porosity. Porosity can involve selective removal of part of the material, achieved via the addition of a thermally degradable substance called "porogen". The porogen is then removed by an anneal to leave behind pores.

Considering low-*k* materials, they are classified into groups:

- non-Si based materials are mostly organic polymers. Their main advantage is low polarizability, which results in reduced *k* value.
- silica-based materials, the most widely studied and used in modern technologies.

Silica has a tetrahedral elementary unit (Figure 4.2 a-b) and to reduce its *k* value, some oxygen atoms are replaced with CH_3 in organosilicate glass (OSG). The addition of CH_3 not only introduces less polar bonds, but also creates additional free volume.

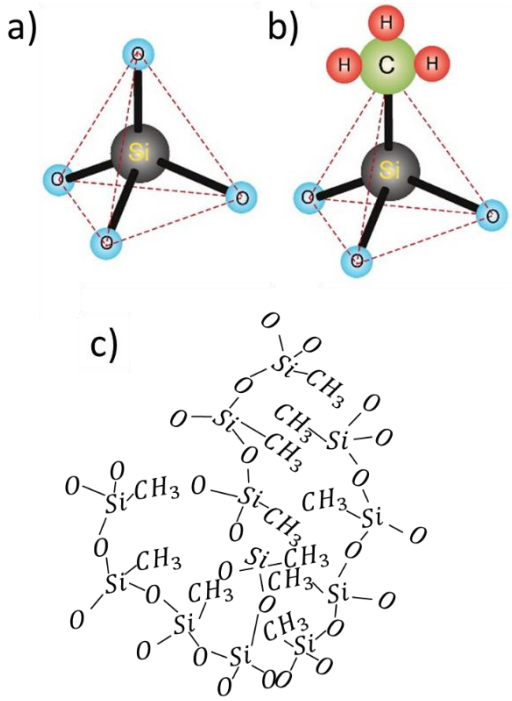

Figure 4.2: Schematic representation of a) a tetrahedral silica unit and b) the same unit of SiOCH material. c) Representation or a carbon silica doped SiOCH material cross-linked after CVD deposition [163].

They are also called hybrid materials as they contain both organic ($-CH_3$) and inorganic ($Si-O$) constituents. The dielectric constant (*k*) value of silica based dielectrics ranges from 2.7 to 3. Low-*k* materials are used as thin films ~100 nm thick. Therefore, there are two main methods of deposition: spin coating and chemical vapour deposition (CVD). By using CVD, the resulting chemical structure is a cross-linked $SiOCH$ low-*k* material as shown in Figure 4.2-c. $SiOCH$ materials were introduced for 90 nm technology (*k*=3.0) and 65 nm (*k*=2.7) [164]. To go further, such organosilicates ($SiOCH$) are made porous after a porogen thermal annealing [165]. At present porous $SiOCH$ materials are actively used for 45 and 28 nm technologies (*k*=2.5) [107]. The

addition of pores induces a decrease in density, as a consequence, materials with better dielectric properties are obtained but this is also detrimental to their mechanical properties. This aspect increases the potential for the material to be damaged during the fabrication process following the low-*k* deposition such as plasma etching and cleaning. Integration processes and material damaging are described in the next sections.

4.1.2 Low-k degradation during fabrication

The low-*k* damage can notably occur when these materials are processed during their integration in microelectronic application, i.e. during plasma reactive ion etching and wet chemical cleaning involved in the integrated circuits patterning.

Such damaging is brought for example by fluorinated plasma or oxygen plasma stripping used during sputtering (trench etching) of low-*k* material. These plasmas break $Si-H$, $Si-C$, and $Si-CH_3$ bonds on surface while replacing them with $Si-O$ groups (Figure 4.3). This increases the *k* value by introducing bonds of higher polarity ($Si-OH$) and reduces hydrophobicity, which makes the material prone to water adsorption (*k*=80) and degrades the insulating properties (section 1.5.3) [166].

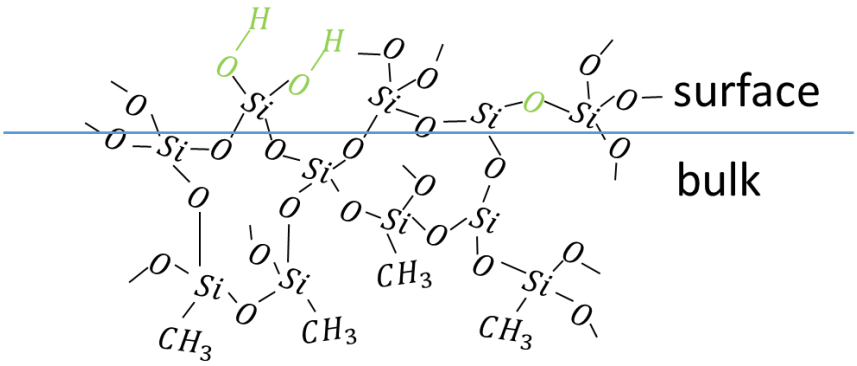

Figure 4.3: Representation or a carbon-silica doped SiOCH material cross-linked after oxygen plasma stripping with the presence of $Si-O$ bounds in the zone interacting with plasma [164].

In a standard clean room atmosphere, enough moisture exists to react with the pore surface and slowly produce a moisture layer. Therefore, it is imperative that the impact of the plasma reactive ion etching on the low-*k* material is analysed at an atomic scale since the properties of the material could dramatically change as a consequence of this etching process. Unlike "optimization" studies, that try to limit the hydrophilization phenomenon by changing the composition of the plasma etching [108], the approach chosen for this study is a post-etch "Restoration" treatment.

Restoration process consists of repairing and capping low-*k* films by a series of silanes rich in methyl groups (Figure 4.4) that will substitute with hydrophilic groups created during the etching process.

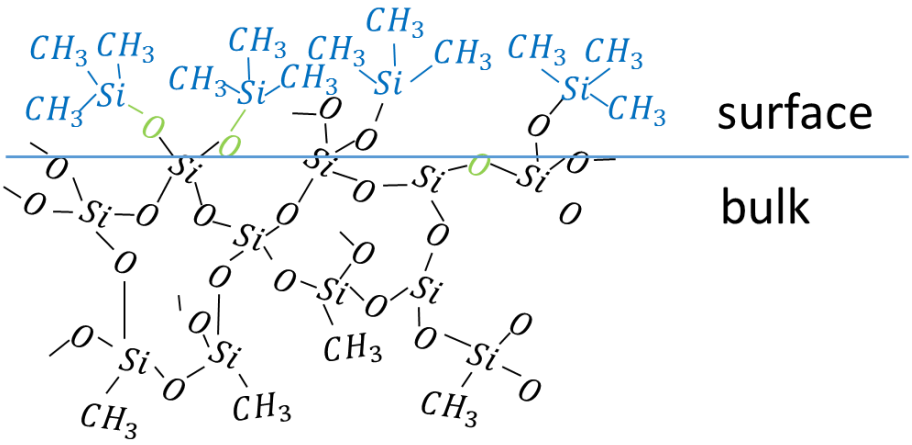

Figure 4.4: A schematic representation (not to scale) of a carbon-silica doped SiOCH material cross-linked after silylation [107].

These processes rely on PECVD deposition of organosilane precursors, coupled with thermal desorption (multiple steps in the $100 - 400\ °C$ range) of airborne molecular contamination and water under vacuum. "Restoration" of such plasma-damaged organosilicates has been already studied in the past [167] with limited success; nowadays this solution is regaining interest, as the distance between lines is decreasing (about $50\ nm$ for the $28\ nm$ technological node), and the damaged vs. pristine material ratio significantly impacts the insulating properties.

Chemical characterisation by ToF-SIMS of low-*k* materials was already performed in the past, especially on spin-on polymethyl silsesquioxanes by depth profiling [78]. The aim of this work is to extend the previous studies to state of art organosilicate $SiOCH$ deposited via Plasma Enhanced Chemical Vapour Deposition (PE-CVD) and fluorine-based etching plasmas with constant overall porosity and relate the chemical modifications induced by integration processes with the dielectric constant modification. To do so, the advanced properties of ToF-SIMS in terms of depth resolution and chemical sensitivity will be explored and adapted to $SiOCH$ cross-linked materials.

4.1.3 Strategies

In order to appreciate the chemical modifications induced by integrating processes on dielectric materials, the identification by ToF-SIMS of their effects in-depth is needed. However, the identification of an adapted SIMS analysis protocol must be made. This

operation goes through different steps such as the selection of an appropriate sputtering source between the ones offered by the used instrument. Argon cluster source and caesium source are selected to be the most appropriate candidates for this work. Contrary to chapter 3 (i-CVD) where a low fragmented chemical information is obtained and applied for M_w discrimination thanks to argon cluster sputtering source, in this chapter the chemistry obtained and characterised is a high fragmented one. As reviewed by Mahoney C. M. [55] (section 1.1.2.2), in the case of organic materials cross-linking under primary cluster ion bombardment, the high mass chemical information is lost but the depth profiling is still possible. In parallel, in chapter 3 a decrease in sputtering yield proportional to the rise of the polymer molecular weight has been shown. Knowing that a cross linked material is defined to have an infinite molecular weight due to the continuity of covalent bounds composing the overall structure, the conclusion is that $SiOCH$ low-*k* depth profiling is possible but with some limitations. These limitations are caused by the cross-linked matrix that implies considerably slow depth profiling compared to organic profiling and a secondary chemical information mainly composed by low mass fragments. Keeping in mind the Seah M. P. diagram representing sputtering yields vs. primary ion energy per atom (E/n) (section 1.2.2), high sputter yields for inorganic materials are reached for E/n higher than $\sim 10\ eV/atom$, GCIB sputter parameters will be set around this value (Ar_{1000}^{+} at $20\ keV$). With these high E/n ratios, an increase in surface roughness with negative effects on the depth resolution is expected as shown by Ichiki K. [168]. In this case, the application of a monoatomic reactive source (caesium) would be a valid alternative because as it was shown by Houssiau L. *et al.* [58] (section 1.2.2) in terms of high depth resolution and secondary ion intensity enhancement especially at low sputtering energies (200/500 eV).

Once defined the most advantageous sputtering source for these materials, the second step is to identify the ideal analysis gun setting depending on the user needs. Contrary to the characterisation needs expressed in chapter 3 where the generation of high mass fragments is favoured, in this case, only an elemental chemical information can be expected. The reason is found in the cross-linked network that need to be much more fragmented to produce secondary ions. As a consequence, the application of monoatomic bismuth (Bi^{+}) analysis source is taken into account and compared with bismuth clusters (Bi_n^{+}). Once achieved a solid knowledge on how to analyse low-*k* porous samples, the study is extended to samples exposed to industrial integrating processes for the production of insulating on-chip layers to achieve information about the chemical modifications

induced by implementation treatments on both extreme surface and depth of low-*k* samples.

However, despite these analytical efforts, all samples presented similar depth integrated mass spectra but slight changes in peak relative intensities and areas are expected from the different studied samples. Therefore, the application of multivariate analysis and in particular principal component analysis on the collected chemical information will be explored and results interpreted and correlated to the variation of the dielectric constant.

4.2 EXPERIMENTAL

The samples studied were all thin films of porous low-*k*, $SiOCH$ type material ($BD2X$™, Applied Materials), deposited on native oxidized silicon fully representative of industrial materials. The deposition was made by plasma-enhanced chemical vapour deposition (PE-CVD) of two precursors: a methyldiethoxysilane ($MDEOS$) organosilicate (Figure 4.5-a), together with an organic porosity generator (or "porogen") bi-cyclopentadiene ($BCHD$) (Figure 4.5-b). Deposition and integration steps were performed by ST Microelectronics (Crolles France) for the comprehension of mechanisms causing the variation of the integration treatments on the dielectric constant (*k*) and the advantageous impact of "Restoration" at the end of the integrating cycle [107].

The porogen was removed by UV-assisted thermal annealing at 350 °C to obtain a porous layer. The aim of this treatment is two-fold: to break and desorb sacrificial porogen molecules, and further cross-link the matrix to achieve suitable mechanical properties as well as porosity. The obtained films were porous organosilicate layers (~17% porosity, as measured by ellipsoporosimetry). Samples were further exposed to standard fluorinated plasma etching (composition $C_xF_y/N_2/Ar/O_2$) process used for lines and via patterning [169].

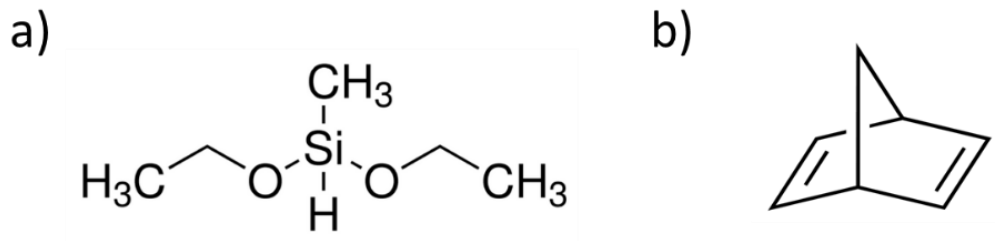

Figure 4.5: Precursor molecules for (a) matrix, MDEOS, and (b) porogen, BCHD, used for PECVD deposition of the low-k films.

4.2.1 SAMPLE FOR SPUTTERING SOURCE COMPARISON

A particular sample named "stack low-*k*" sample originally deposited for further compositional studies [170], was selected in order to compare argon cluster and monoatomic caesium as sputtering sources. A 100 nm film deposited on oxidised silicon is exposed for 30 s at 350 °C to standard fluorinated plasma etching process. This resulted in a remaining thickness of 40 nm, and a second layer is directly deposited on top of the first one and etched in the very same way. This operation was repeated 6 times to obtain a 240 nm stack, in order to maximize the modified SiOCH material proportion (Figure 4.6). Repeated chemical modifications are expected to be detected by ToF-SIMS depth profiling useful for depth resolution purposes.

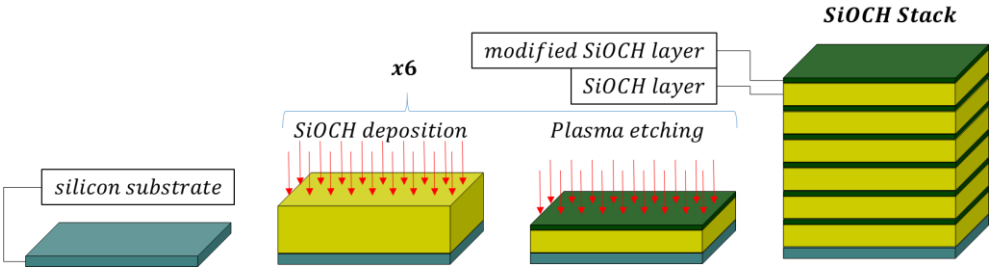

Figure 4.6: Scheme of the stack low-k sample production steps: 100 nm deposition of SiOCH by PECVD etched reducing the thickness to 40 nm after plasma etching. These operations are repeated six times. Plasma etching produces a modified SiOCH layer on the top of the deposited material.

4.2.2 SAMPLES FOR INDUSTRIAL INTEGRATION PROCESS DISCRIMINATION

This sample set was composed of seven samples. A reference of 80 nm of PECVD $SiOCH$ material was deposited on seven 200 mm silicon wafers with native oxide on surface. Three wafers were then exposed to standard fluorinated plasma etching (composition $C_xF_y/N_2/Ar/O_2$) process as described previously reducing the thickness to ~20 nm (samples 2 to 4). Samples 5 to 7 were then exposed to post-etch aqueous wet cleaning ($dHF\ clean$) chemistry containing diluted fluorhydric acid (HF/H_2O 0.2 $\%_w$). Two so-called "restore processes" (named $Res1$ and $Res2$) were applied after plasma degradation in order to evaluate their efficiency in restoring dielectric properties and surface hydrophobicity. Chemistries employed in these processes are often protected by patents and are not revealed. The difference between the two processes consists in UV

light activation for "restoration1". UV light is supposed to promote the water desorption and mutual $Si-OH$ condensation [171]. The restoration1 is the most successful one in recovering the dielectric constant to its original value as shown by Corona Oxyde Characterisation of Semiconductor (COCOS) results [172]. In order to describe the chemical modifications of the low-k material step by step, these restoration processes are applied in the two situations:

- Immediately after $plasma\ etch$ (samples 3&4)
- After $plasma\ etch\ +\ dHF\ clean$ (samples 6&7)

The whole sample set, with detailed sample features, is summarised in Table 4.1.

Table 4.1: Treatment features, dielectric constants, and thicknesses of the various Ultra-low-k samples studied.

Sample	*Process* 1	*Process* 2	*Process* 3	*k value**	Thickness
1				2.6	~80 nm
2	C_xF_y *plasma etch*			5.9	
3	C_xF_y *plasma etch*	*Restoration1*		3.0	~20 nm
4	C_xF_y *plasma etch*	*Restoration2*		5.2	
5	C_xF_y *plasma etch*	*dHF clean*		6.2	
6	C_xF_y *plasma etch*	*dHF clean*	*Restoration1*	3.1	~20 nm
7	C_xF_y *plasma etch*	*dHF clean*	*Restoration2*	4.2	

** determined by Corona Oxide Characterisation of Semiconductor method (COCOS)[172]*

4.2.3 Instrumental sputtering settings

In Table 4.2 sputtering settings used in this study are listed. All the characterisation are performed using charge compensation because of the insulating properties of the samples on a rastered area of 300x300 μm^2. "Non-interlaced" mode (section 1.1.1.2) is applied during caesium sputtering because a longer pause time between sputtering and analysis is needed to properly compensate charges.

Table 4.2: Sputtering settings used for the "stack" sample depth profiling.

Source	***Energy***	***Current* (*nA*)**
Ar^+_{1000}	20 *keV*	1.12
Cs^+	2 *keV*	162
Cs^+	1 *keV*	82
Cs^+	500 *eV*	47

The applied “non-interlaced mode” consists of two seconds of sputtering followed by two seconds of pause for each bismuth analysis pulse. Charge compensation by electron flood gun was not used during GCIB sputtering. The caesium sputtering energies are chosen among the existing setting normally installed on industrial systems by the equipment manufacturer. Starting from the highest energy and decreasing it, sputter rates decrease and analysis times dilate: effects on the detected chemistry and depth resolution were studied.

4.3 IDENTIFICATION OF THE BEST APPROPRIATE SPUTTERING AND ANALYSIS CONDITIONS

As stated before, a comparison between sputtering sources is carried out on the so-called “stack sample” for the evaluation of the in-depth quality of detected chemistry. Argon cluster and low energy caesium guns, both excellent sources for polymer depth profiling, are then compared.

4.3.1 ARGON SPUTTERING

In Figure 4.7 the depth profiling of the stack sample sputtered with the argon cluster source is given. The six different low-*k* layers can easily be distinguished, separated one from the other by interfacial layers marked by maximum signals for the chemical species CN^-, C_2H^- and OHF^-. These ions are characteristic of the plasma modified layers because it contains elements brought during fluorine and nitrogen based plasma etching. These interfacial layers are attributed to specific plasma damaged areas of the low-k material. Nitrogen and fluorine-enriched layers are grown during the repeated etching processes creating complex structures and decreasing the intensity of elemental or bulk species such as O^-, F^- and SiO_2^-. This observation is consistent with the already reported formation of fluorinated layers by the interaction of similar kinds of plasmas with $SiOCH$ materials [173]. In the presented depth profile the first modified layer in extreme surface is not visible. No clear explanations for this phenomenon can be given. Higher sputtering yields can take place on surface impeding the right profiling of the first nanometres.

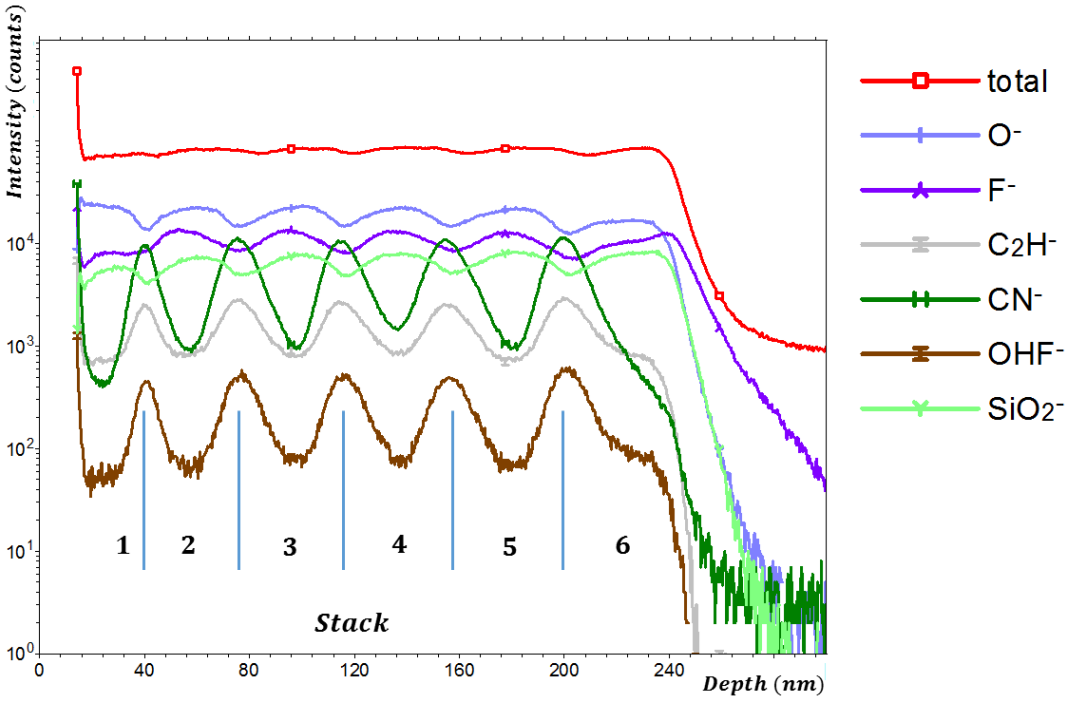

Figure 4.7: Ar^+_{1000} depth profile of the "stack sample". Depth calibration is set at 40 nm in-between first and second stack and at 200 nm in-between the fifth and sixth stack.

Ar^+_{1000} depth profile is characterised by a reduced sputtering rate ($\sim 0.2\ nm/s$) leading to a long analysis time to reach the interface (around 20 $minutes$). This sputter rate is not conventional for a polymer exposed to these sputtering conditions: i.e. in the case of a PMMA with a similar thickness, sputtering would take around 2 $minutes$ to reach the interface with an associated sputtering rate of $\sim 2\ nm/s$, ten times faster. The reason is the cross-linked structure of $SiOCH$. The density of covalent bonds is higher compared to a "linear" polymer sample and the cross-linked network is highly correlated. Argon cluster bombardment is thought to sputter polymer chains by transferring the kinetic energy of the argon atoms. In the case of cross-linked materials, the concept of polymer chain is lost as a cross-linked material is considered to have an infinite molecular weight. The prevalent sputtering mode is then characterised by matter fragmentation and not by the ejection of entire molecules chains such as in linear polymers. This is why high energetic (20 keV) little argon clusters (1000 $atoms$) is the only efficient sputtering setting for this type of materials.

It is then logical to think that cross-linked materials find their place in the Seah diagram (re-proposed in Figure 4.8) in an intermediate position between the organic material and inorganic depending on their cross-linking degree. The difficult part is to place this kind of materials as pore content and cross-link degree can vary its position considerably

regarding the yield per atom axis. In Figure 4.8, the experimental value extrapolated while profiling the studied "stack" sample is located. No other points are proposed because of the limited interest in this study regarding the time-consuming analysis and most of all for the reduced depth resolution that will be shown to be better using low energy caesium as sputtering source.

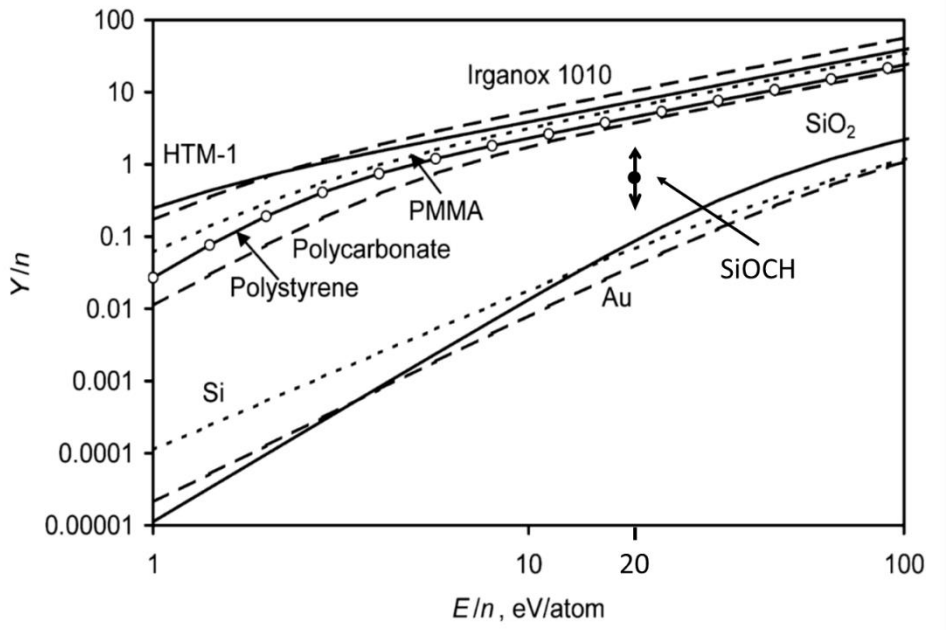

Figure 4.8: Argon GCIB sputtering yields per argon atom as a function of the energy per atom for organic and inorganic material obtained by Seah. The sputtering yield has been calculated for a SiOCH material as well but the porous nature of these materials and the density of reticulation do not permit the calculation of the atomic number density increasing data scattering (ref. [34])..

4.3.2 Stack sample depth profiling by caesium sputtering

It is important to remind that the advantage of caesium can be mainly summarised in two points:

- This monoatomic source can sputter organic, inorganic and hybrid materials as well by cascade collision mode (section 1.1.2.1)
- Being a reactive source (section 1.1.2.2), detected intensities are brighter and more intense compared to argon cluster sputtering; in Figure 4.9 the intensities of examined peaks are ten times more intense when caesium is used as sputtering source.

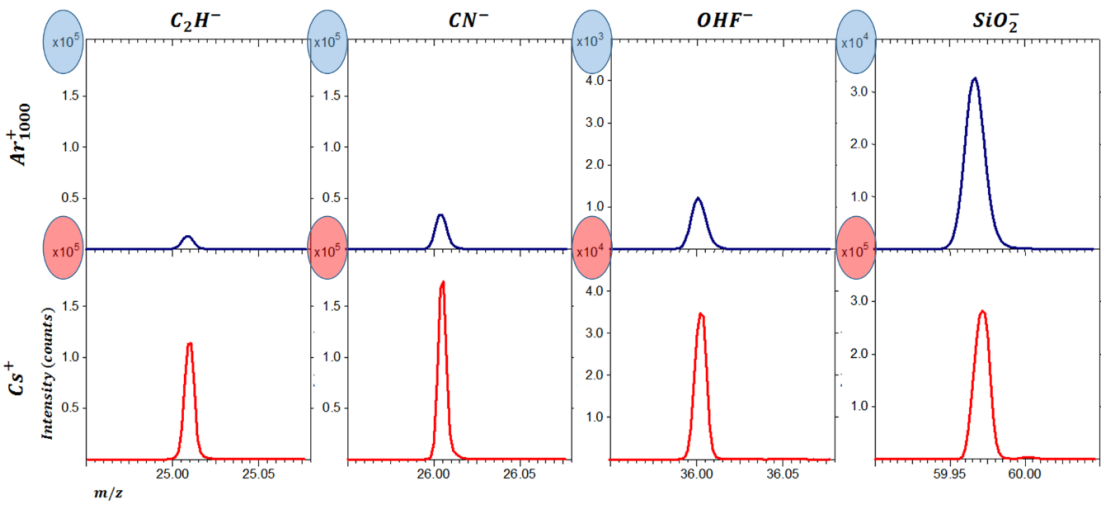

Figure 4.9: Comparison between intensities of examinated peaks obtained by Ar_{1000}^+ 20 keV and Cs^+ 1 keV sputtering. Intensity scale has been adapted to provide for proper visualisation of peaks shapes. Ar_{1000}^+ peak intensities are normally ten times less intense compared to Cs^+ intensities.

For these reasons the "stack sample" has been analysed in depth profiling mode by using three Cs^+ sputtering energies and depth profiles are studied in detail in the next sections.

STACK DEPTH PROFILING USING 2 keV NON-INTERLACED CAESIUM GUN

In Figure 4.10-a the depth profile is shown. In the zones in-between two $SiOCH$ stacks, oscillations on the "total" signal representing the number of ions passing through the detector (also saturated signals) are observed. These oscillations are caused by the higher concentration of electronegative species reacting with caesium and generating a higher ionisation.

The obtained depth profile is more irregular compared to the one obtained by argon sputtering and the intensity gap between deposited and plasma modified layer enhanced. In parallel, the apparent thickness of the modified layers increases from the first to the last. The reason can be the combination of damage accumulation due to bombardment and the diffusion of the plasma modified species through the $SiOCH$ layer.

STACK DEPTH PROFILING USING 1 keV NON-INTERLACED CAESIUM GUN

The 1 keV depth profile is given in Figure 4.10-a and it presents similar features compared to 2 keV sputtering. The transient at the beginning of the depth profile is reduced, as a consequence the extreme surface chemical information is becoming

accessible. Si_2^- and SiO_2^- signals present a decay around the modified layer consistent with the observations made during argon cluster sputtering. However, in this case, interfaces are sharper indicating that a real top $SiOCH$ layer is present compared to previous sputtering modes characterised by less sharper interfaces. Si_2^- and SiO_2^- oscillations disappear while sputtering the third layer It is thought that in this sputtering mode the bottom crater roughness generated during analysis is still important. This hypothesis is confirmed by the decrease of depth resolution quality decreasing through the sample depth. Particularly characteristic is the strange peak of fluorine between the two first low-k layers since between other layers it decays in the plasma etching damaged zone. It is possible that the deposited fluorine after the last plasma etching has diffused through the last stack blocked by the damaged zone that acts like a barrier to the diffusion. The CN^- signal detection is saturated in plasma damaged layers at this sputtering energy, this phenomenon being explained by the higher caesium coverage on the sample surface as a function of the lower sputtering energy (section 1.1.3.1).

This result shows that this protocol is in good agreement with the attempt to increase depth resolution by decreasing sputtering energy.

STACK DEPTH PROFILING USING 500 eV NON-INTERLACED CAESIUM GUN

Decreasing further the sputtering energy, Figure 4.10-c represents the depth profile of the "stack sample" sputtered with a caesium ion flux at 500 eV in non-interlaced mode.

It presents similarities with previous depth profiles but with a better depth resolution. This aspect can be appreciated by following Si_2^- and SiO_2^- profiles presenting a depletion in the plasma etched modified layers for all the six stacks (in 1 keV caesium sputtering this sensitivity is lost after the third low-k later). In this sputtering mode the extreme surface modified layer is also revealed. This result opens the possibility to finely characterise the entire sample depth with good sensitivity thanks to the reactivity of the sputtering source and the optimal depth resolution.

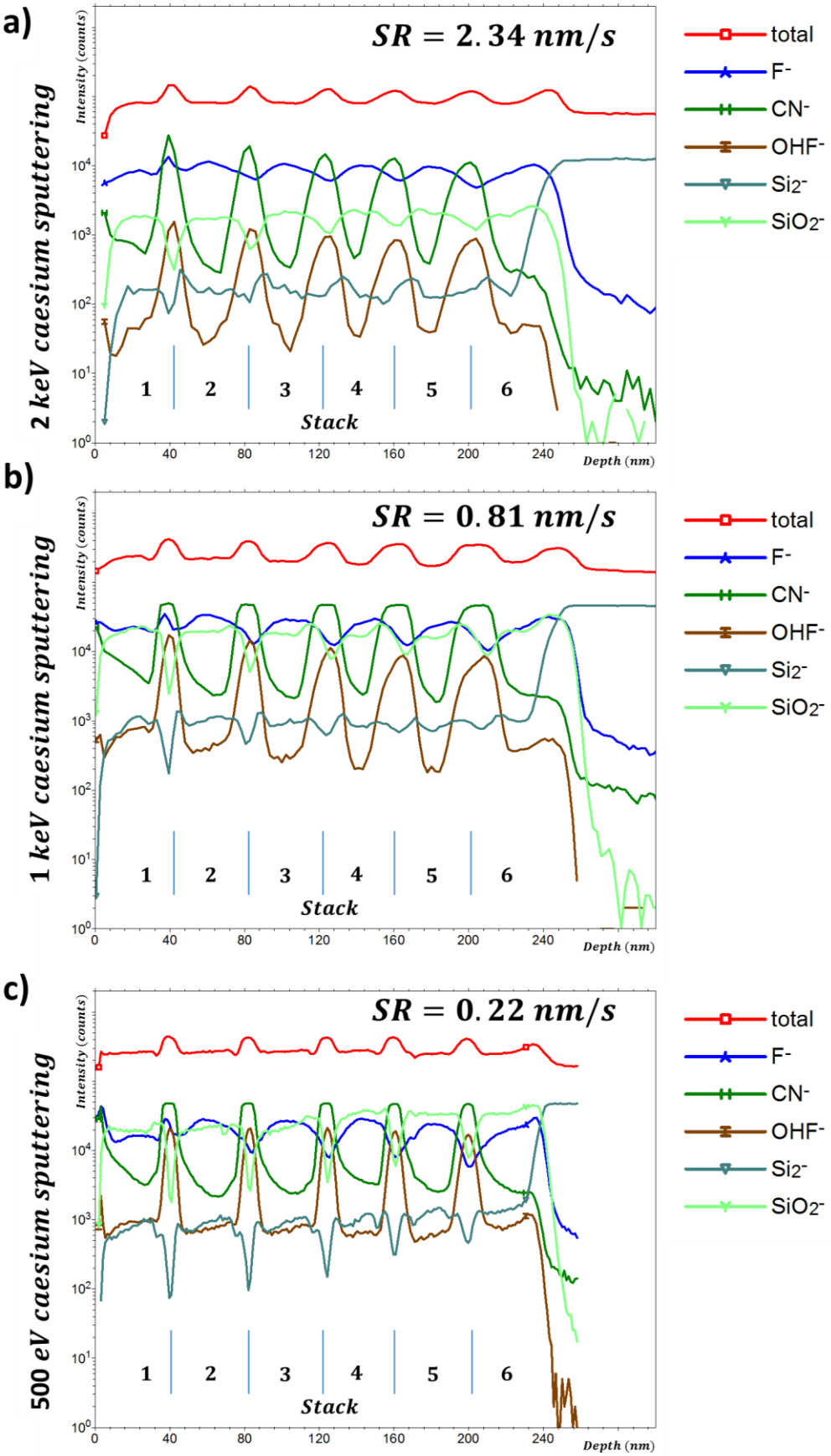

Figure 4.10: In-depth profiling of the SiOCH "stack sample" by a) 2 keV b) 1 keV and c) 500 eV caesium sputtering with the corresponding values of sputter rate (SR).

Depth profiling at 500 eV as well as in 1 keV caesium sputtering indicates the same strange presence of fluorine between the first two layers. In Figure 4.11 a zoom of the zone of interest shows that the presence of fluorine is extended on extreme surface too. As stated before the hypothesis is that the modified layer plays a barrier role impeding the fluorine diffusion through the stack. For the top surface, the high fluorine content is identified to be a combination of the modified layer fluorine content and fluorine deposition due to airborne pollution.

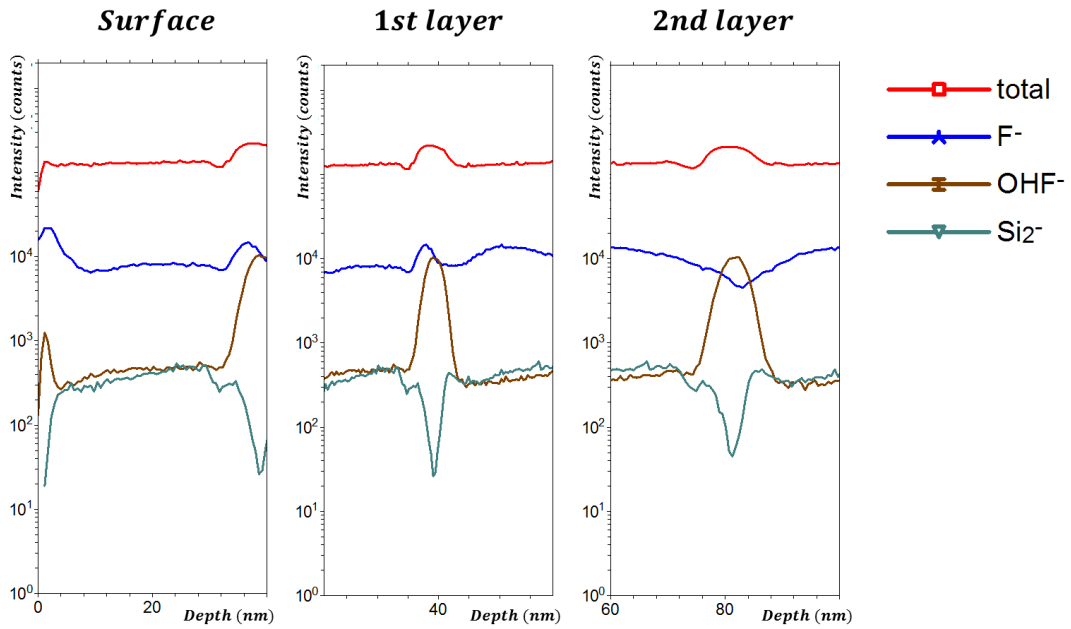

Figure 4.11: In-depth comparison of "stack sample" plasma damaged layers and the anomalous behaviour of fluorine signal between surface, first and second layer sputtered at 1 keV.

The use of caesium and the reduction of the sputtering energy is shown to be advantageous for in-depth resolution opening the possibility to study the chemical modifications induced on top surface samples by industrial integration treatments with reasonable analysis times. As a consequence, a further reduction of sputtering energy down to 250 eV (not performed on the "stack" sample) still will maintain positive effects on depth resolution and secondary chemical information.

4.3.3 Depth resolution

The depth resolution of each stack for every sputtering mode have been measured on the decreasing signal of OHF^- on each plasma modified layer (Table 4.3). The ion OHF^- is chosen because it was well adapted for the identification of the modified layers.

Table 4.3: The table represents the depth resolution (nm) of each identified stack as a function of the used sputtering setting. The depth resolution is defined as the depth downward interval in which a profile decays from 84% to 16% of full intensity.

Layer n.	Ar^+_{1000} $20keV$	Cs^+ $2keV$	Cs^+ $1keV$	Cs^+ $500eV$
1	Not observed	Not observed	Not observed	1.2
2	4.2	4.6	4.1	2.3
3	6.5	6.2	4.1	2.9
4	8.5	6.2	4.1	2.9
5	9.8	6.2	5	3.4
6	10	6.2	5.1	5

As observed in-depth profiles, the depth resolution quality increases while decreasing sputtering energy. The cross-linked matrix reduces argon cluster sources sputtering efficiency and an increase in the roughness is thought to be at the origin of the low depth resolution (not verified by AFM). The obtained resolution at 500 eV caesium sputtering suggests this protocol to be the most adapted for a depth resolved sample characterisation. This result is consistent with results in bibliography that shows caesium as a good candidate for polymer depth profiling. It is observed that in each sputtering mode the depth resolution decreases while approaching to the interface with silicon. This is a well-known phenomenon due to the increasing roughness of the bottom crater during analysis. In conclusion, caesium 500 eV sputtering energy is the most appropriate sputtering source capable to reach good depth resolutions around 1 nm in the first sputtering steps (first 40 nm).

4.3.4 Selection of analysis primary ion: Bi_1^+ vs. Bi_3^+

4.3.4.1 In-depth comparison on "stack sample"

During analysis, a comparison between analysis sources is also performed to show the importance of selecting appropriately the cluster size of bismuth ions on the secondary chemical information.

The intention is to inspect the quality of the chemical information obtained and evaluate the most interesting analysis setting for this work. It is important to remind that the collected chemistry is composed of low mass fragments due to the cross-linked matrix not permitting to have a high mass fragment information. The selected analysis source study is the bismuth source already used in the chapter concerning i-CVD deposited polymeric samples. The Bi_1^+ and Bi_3^+ settings are generally used for mass resolved chemical characterisations. The selected energy is 15 keV for both settings.

Figure 4.12 shows the depth profile of the first two stacks characterised with the two analysis settings Bi_1^+ and Bi_3^+ while sputtering with caesium at 1 keV. The "total" signal detected results to be more intense in Bi_3^+, this is explained by the difference interaction of bismuth clusters with the target. In Bi_3^+ analysis mode, the total energy is divided by the number of primary ions. The localisation of the impact zone is then more in surface favouring the ejection of a higher number of secondary species. Signals such as SiO_2^- result saturated impeding the right interpretation of depth profiles. Another advantage of Bi_1^+ as analysis source is that apparently transient phenomena (signals irregularities during the first scans) is minimised. The reduced transient phenomenon is fundamental if the zone of interest for the analysis is placed at extreme surface.

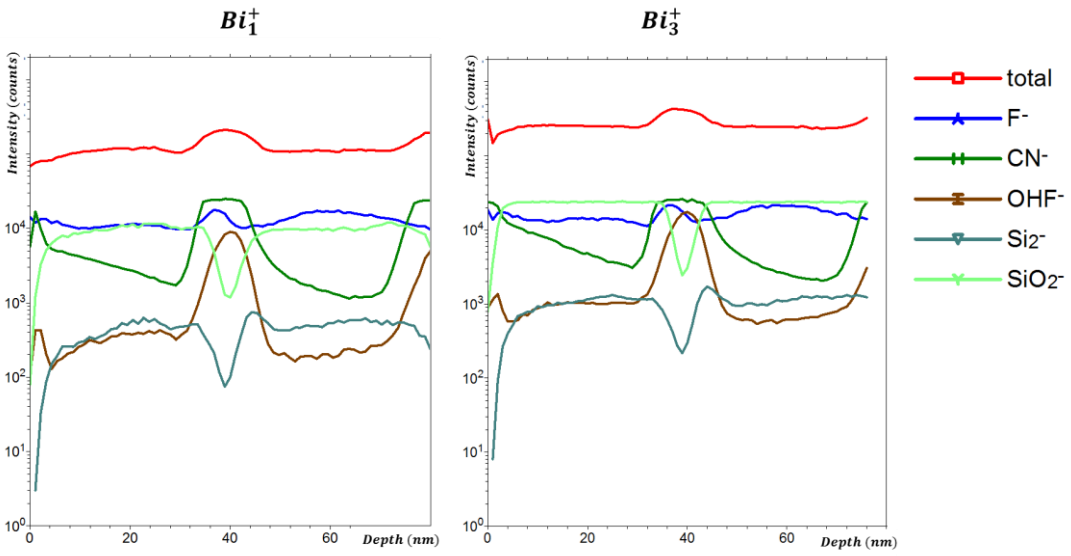

Figure 4.12: Bi_1^+ vs Bi_3^+ during 1 keV Cs^+ sputtering.

A similar comparison between analysis sources is performed on the industrially processed sample set composed by a PE-CVD $SiOCH$ dielectric material etched, cleaned and restored.

4.3.4.2 COMPARISON OF ANALYSIS SETTINGS ON INDUSTRIALLY PROCESSED LOW-K SAMPLES AND INFLUENCE ON PRINCIPAL COMPONENT ANALYSIS

In this case, chemical differences between the two analysis mode are compared by applying principal component analysis to the sum of spectra collected while sputtering the first 5 nm of each sample by a 250 eV caesium sputtering source. In this case the bismuth source used has an acceleration potential of 25 keV due to instrumental limitations (another model of bismuth gun was available for this study). The difference in the primary ion acceleration energy between 15 and 25 eV is considered marginal in comparison with the variation on cluster size.

Figure 4.13 shows the PCA scores and loadings applied to the mass spectra of the seven samples sputtered with the 250 eV Cs^+ beam and, analysed either with Bi_1^+ or Bi_3^+ ion beam. After applying a common peak list a normalisation by the area of the selected peak was performed. It is observed a clear discrimination depending on bismuth cluster size: positive values correspond to high mass fragments generated by cluster bismuth while negative values are characteristic of low mass fragment mainly ejected during monatomic bismuth bombardment.

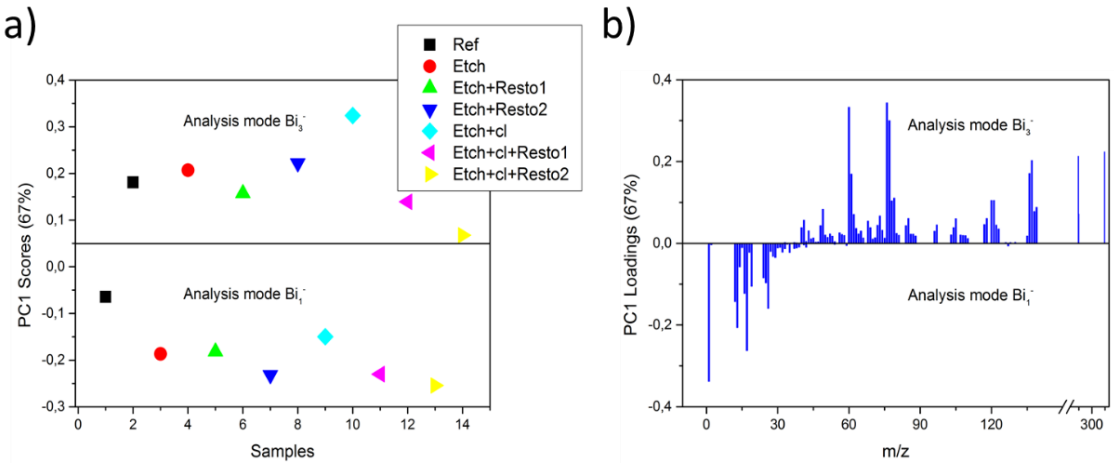

Figure 4.13: PC1 scores (a) and loadings (b) plot of low-k films data analysed with two kinds of primary ions. The PC1 Scores (67%) in the left plot show a clear separation between monoatomic Bismuth (negative scores) and Bi_3^+ (positive scores). The PC1 loadings in right plot show the main peaks responsible for the separation observed on scores plot.

The score plot shows a clear distinction between the two analysis modes. In Table 4.4 are listed the fragments mainly responsible for the differences produced by analysis mode.

Table 4.4: Significant loadings from PCA of negative ions spectra analysed in Bi_3^+ and Bi_1 mode 25 keV. Positive loading have higher mass ions because Bi_3^+ source has a lower fragmentation effect on organic matter contrary to what is obtained by monoatomic bismuth.

$PC1$ (67%)	Peaks (amu)
Positively loaded peaks (Bi_3^+)	49:CH_2OF^-; 60:SiO_2^-; 61:SiO_2H^-; 76:SiO_3^-; 77:$Si_2O_3H^-$; 137:$Si_2C_4HO_2^-$; 209:$Si_6C_2OH^-$
Negatively loaded peaks (Bi_1^+)	12:C^-; 13:CH^-; 16:O^-; 17:OH^-; 19:F^-; 24:C_2^-; 25:$C_2\ H^-$; 26:CN^-

High mass ions, characteristic of cluster bismuth bombardment, are in opposition to low mass fragments produced during monoatomic bismuth analysis. Low mass fragment generation is not a surprising result as fragmentation is known to be higher during Bi_1^+ bombardment. The main goal remains the effect of integration treatments on thin low-*k* films. We concluded that even if complex chemical information is analysable in Bi_3^+ and less damaging for the analysed sample, excessive information is already collected with single bismuth. In addition, high mass fragments describe mainly the branched 3D low-*k* structure ($Si_xO_yC_aH_b$), while an integration treatments modification are expected to apply their main effects at low masses (i.e. fluorine, nitrogen or methyl groups). Finally, to increase the signal/noise ratio for these compounds, Bi_1^+ is found to be a better candidate because it offers a higher secondary ion fluence.

4.4 INDUSTRIALLY PROCESSED LOW-K SAMPLES DISCRIMINATION BY TOF-SIMS ANALYSIS COUPLED WITH PRINCIPAL COMPONENT ANALYSIS

4.4.1 TOF-SIMS PROTOCOL

Next to information learned about how depth profiling low-*k* materials, the objective here is to study industrially processed low-k samples and assign the resulting chemical modifications. The application of a reactive monoatomic sputtering source has shown its advantages in profiling these materials. Furthermore, the decrease of accelerating energy opens the access to the characterisation of the extreme layers with a good in-depth resolution and an enhanced secondary ion information. In this particular study, an even lower sputtering energy is applied (caesium 250 eV at 7.5 nA current) and monoatomic 25 keV bismuth as analysis source with a measured current of 1.3 pA. Charge compensation is also performed in "non-interlaced" mode applying two seconds of sputtering followed by two seconds of pause for each bismuth analysis pulse. As shown in previous depth profiles, the impact of integrating treatments is limited to the layer surface around $\sim 5\ nm$. This protocol is then coupled with principal component analysis to reveal the fine chemical differences generated by implementation treatments that normally are difficult to be appreciated by simply observing spectra or depth profiles. Therefore, to increase the detected secondary ion information, 5 spectra are acquired for each in-depth scan.

4.4.2 CHEMICAL MODIFICATIONS INDUCED BY INTEGRATION PROCESSES ON LOW-k MATERIALS

Five negative depth profiles at high mass resolution are acquired for each of the seven samples described in Table 4.1. Peaks are selected from a representative spectrum for each sample. Automatic selection is used for the creation of a list of 102 peaks for the negative ion spectra. PCA is then performed considering the counts of a common peak list applied to all samples spectra.

Preliminary data analysis, not presented in this work, have shown that treatments made on the samples produced only small changes in the data collected by ToF-SIMS. A first PCA was then performed to assess the real existence of chemical differences between the samples. For this purpose the sum of spectra acquired during in-depth profiling of the first

$\sim 5\ nm$ of integrated dielectric samples is analysed statistically by PCA and for chemical differences evidenced on the samples are plotted in Figure 4.14.

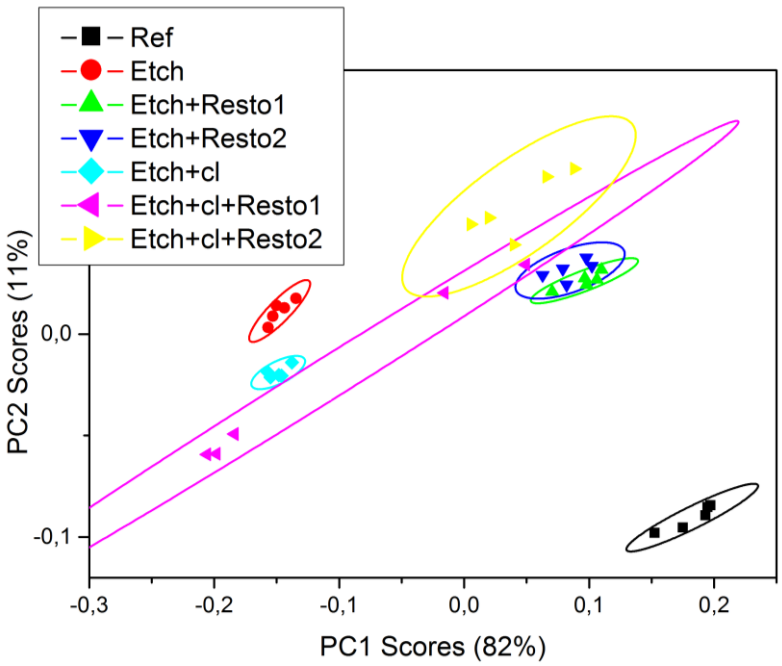

Figure 4.14: Score plots of 1st and 2nd PC's applied to depth profile mass spectra of low-k films analysed by ToF-SIMS. PC1 separates reference and restored samples from etched samples while PC2 separate restored samples from the reference. After restoration processes, the low-k seems to be re-established, both PC2 detect differences. Etch+cl+Rerto1 sample has an ambivalent behaviour.

This plot shows the scores of the principal components (PCs) 1 and 2 of the organosilicates samples spectra, capturing 82% and 11% of the variance in the data set respectively. The ellipses represent the confidence mark for each group indicating the data dispersion in a range of 95%. Loading plots for each principal component make the interpretation of the key variables characteristic of a given sample and helps to distinguish it from others. In Figure 4.14, all samples are distinguished one from the other indicating that PCA can resolve sample individually.

Starting from the position occupied by the reference, in PC1 is mainly described the chemical transition related to '$etch$' processes. The separation between etched and cleaned samples appears to be revealed by the second principal component. Considering restoration processes, their associated chemical modifications seem to be described by both principal components. Therefore, both components must be considered in the examination of the chemical modifications deriving from the integration treatments. The deposition of fluorine and fluorocarbon species during plasma etching is expected to occur only in surface [108]. What is new is that, after restoration, the silanisation of the

surface brings an apparently reference-like chemical composition considering the PC1 but contradictory according to the PC2. As low-*k* properties are re-established for both "$etch + clean$" and restored samples (Table 4.1), the conclusion is that their surface composition is different compared to the reference. It is also worth noting that the data dispersion in the score plots is more important for "$etch + clean + restored$" samples, especially for sample 6, probably related to an inconstant chemical effect over the whole sample surface.

Considering only the PC1 scores (Figure 4.15-a), there is a clear distinction between the group of restored sampled together with the reference (positive values), in opposition to samples processed by plasma etching, followed or not by diluted HF cleaning ("$Etch + cl$" label). PC1 loading plots (Figure 4.15-b) show that the peaks belonging to the plasma treated samples (negative loadings) have an increased contents in nitrogen and fluorine, that is consistent with previous works (section 1.2.3). The PC1 loadings in right plot show the main peaks responsible for the separation seen on scores plot. As seen from the loadings the main peaks responsible for the sample differences are the molecular ion deposited during fluorine etching (negative loadings) and carbon based ions incorporated during restoration or already present in reference (positive loadings). PC2 score (11%) plot helps to mostly discriminate reference sample from restored samples. In PC2 loading score, negative data are a mixture of reference and etched chemistry, this aspect is appreciated comparing loadings information with sample peak areas. Saturated peaks such as OH^- are not taken into account. In exchange, OH^- isotope is selected ($^{18}OH^-$ separated from F^- peak) but the lower intensity hides its contribution on the discrimination of sample groups by PCA. Unfortunately, this aspect is an important limitation because the presence of $Si - OH$ groups is considered to be one of the principal causes of water uptake in dielectric materials [78].

In the other hand, positive loadings belonging to restored and reference samples are mainly carbon (C_2^-, $C_2\ H^-$, C_3^-) or organosilicates fragments (SiH_4O^-, $SiC_2H_4O^-$). The peak index is not unequivocal and their identification is hard. Positives PC1 loading can be easily confused with fluoroether fragments. C_3^- (36.0005 amu) fragment mass differs by $1x10^{-3}\ amu$ compared to OHF^- fragment (36.0017 amu), but the existence in spectra of $C_3H_x^-$ fragments confirms that the carbonated fragment is predominant. These results are consistent with the restoration treatment as its expected effect is the substitution of $-Si - OH$ groups, formed by etching, by $-Si - CH_3$ groups [174].

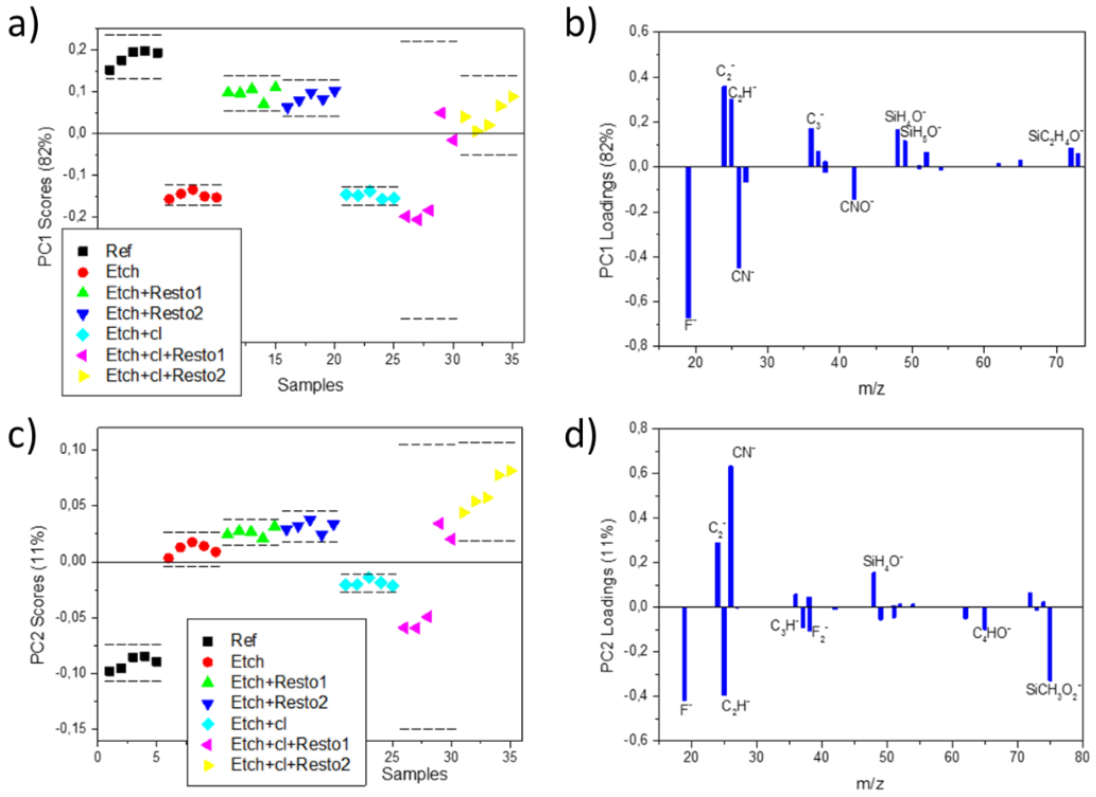

Figure 4.15: PC scores (a-c) and loadings (b-d) plot from Ultra-low-k films mass spectra data. Horizontal lines show the upper and lower confidence limits for each sample group.

Considering the second principal component PC2 (Figure 4.15-c), the score plot separates reference (negative scores) from restored samples (positive scores), with the etched samples among them. Loading plot in Figure 4.15-d gives clues for the interpretation of these differences: $SiCH_3O_2^-$ is considered to be a fragment that well describes the $SiOCH$ low-k structure. Its absence on restored samples confirms that a different deposited chemistry is obtained as a mix of functionalized pore surface and organosilane deposited fragments. Fluorine and CN^- species are also present in loadings for PC2: as stated before regarding PC1 they are clearly characteristic of both etched and cleaned samples However, in PC2, these species are not associated with the same samples: CN^- appears related to all samples but not to the reference. At this point, it appears a still complex chemical situation, not completely resolved from spectra data analysis coupled to PCA.

4.4.3 DEPTH DISCRIMINATION OF CHEMICAL MODIFICATIONS SUPPORTED BY LOW-K MATERIALS DURING INTEGRATION PROCESSES

In order to bring supplementary information to PCA results for the identification of discriminating variables that govern this complex system of chemical changes, information in depth has been then considered.

Among the amounts of detected peaks, a limited set of characteristic peaks was selected considering the results of the PCA for sample chemical discrimination. Four peaks were particularly envisaged for this study. Fluorine (F^-) was meant to describe effects produced on etched samples, while carbonaceous fragment (C_2H^-) was considered representative of restored samples, for the reasons stated in the previous section. Two organosilicate fragments have been considered to describe reference and restored samples $SiCH_3O_2^-$ characteristic of the reference sample and (SiH_4O^-) typical for restoration. The in-depth profiles of these selected species are shown in Figure 4.16, describing the evolution of the 5 top nanometres of the samples. Considering that the sputter rate may not be constant along the depth profiles (densified layer induced by implementation treatments), the Cs fluence has been preferred to a depth scale for the x-axis of the graphs.

From these figures, it can be observed that the fluorine peak is indeed the highest in etched and "$etch + clean$" sample with a contribution spread deeper in the network of the low-*k*, reference presenting the lowest concentration (Figure 4.16-a). This F^- specie is then thought to be critical regarding the dielectric properties of the low-*k* material. Regarding C_2H^- (Figure 4.16-b), the highest contributions are associated with restored samples. However, the two restoration processes act differently according to the existence or not of a cleaning step. For the $SiCH_3O_2^-$ organosilicate (Figure 4.16-c), its position as characteristic of the original low-*k* network is clearly established as being highly predominant in its top surface chemistry. The $SiCH_3O_2^-$ intensity rapidly decrease in-depth to values comparable to the ones of the other samples. The other organosilicate fragment SiH_4O^- (Figure 4.16-d) can effectively be identified as representative of the modifications induced by restorations processes on the low-*k* network, with contribution spread over several in-depth nanometres.

Independently to this very helpful information on the chemical and in-depth action of these different processes undergone by industrial low-*k* materials, a straightforward correlation between *k* value and chemical composition is still tough to establish. Indeed,

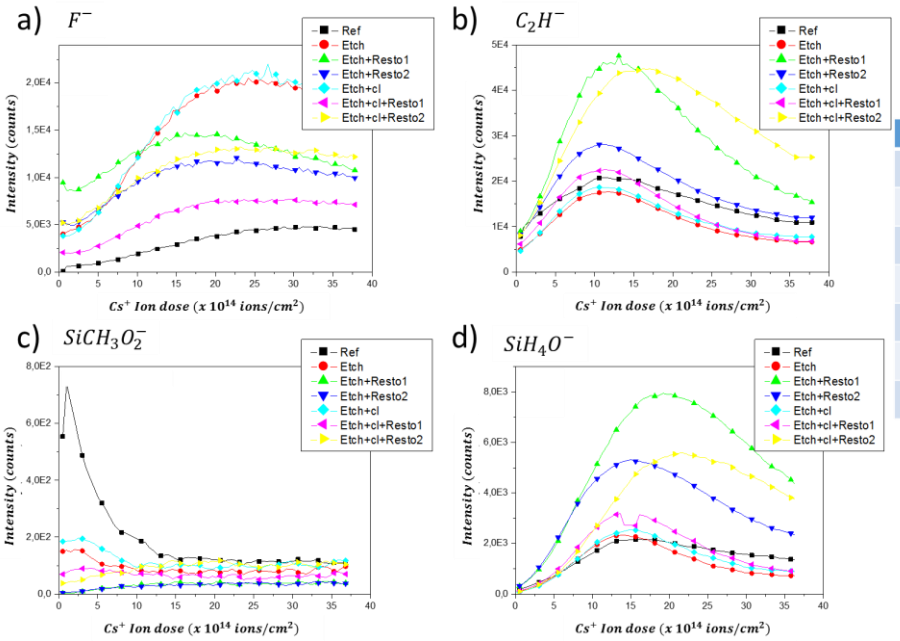

Sample	*k* value
Ref	2.6
Etch	5.9
Etch+Resto1	3.0
Etch+Resto2	5.2
Etch+cl	6.2
Etch+cl+Resto1	3.1
Etch+cl+Resto2	4.2

Figure 4.16: In-depth plot of fluorine (a), C_2H^- (b), $SiCH_3O_2^-$ (c) and SiH_4O^- (d). The transient is thought to be extinguished after a few scans far from the surface corresponding to a fluence of caesium of ~2 or 3 10^{14} ions/cm^2.

while considering the C_2H^- peak, it could expect that high concentration would refer to low dielectric constant: it is not the case for the "$etch + resto2$" with a dielectric constant of 5.2. A similar argument can be brought considering fluorine content, assumed to be deeply related to high dielectric values: the "$etch + resto1$" sample owns the most similar dielectric constant to the reference material but at the same time it possesses one of the highest F^- content. The link between ToF-SIMS detected chemistry and dielectric constant is not directly achieved probably because of the absence of $-OH$ chemical information discriminating samples. The detection of $-OH$ groups introduced during integration processes could better clarify the link between the material chemical composition and the dielectric constant modifications.

4.5 Conclusion and perspectives

Argon cluster polyatomic sources and monoatomic reactive ion sources were applied for cross-kinked material depth profiling and results were compared. It was demonstrated that the cross-linked matrix of $SiOCH$ dielectric materials can be sputtered with cluster argon sources but sputter rates and depth resolution are reduced due to the higher density of primary chemical bonds compares to linear polymers. Better depth resolution and enhanced ionisation awarded low energy caesium as the best sputtering source. The most

significant results were obtained at energies lower than 500 eV such as 250 eV in terms of ionisation and depth resolution .

Regarding analysis settings, monoatomic bismuth setting is favoured as it was shown to produce a limited “transient” effect in depth profiling ideal if the zone of interest for the analysis is located in extreme surface.

In addition, the multivariate analysis (PCA) method has shown to be able to amplify differences between samples significantly. This enables to observe relevant chemical variations at the top surface of such films otherwise difficult to evidence. This approach allowed combining the variation of physical properties (dielectric constant) with the chemicals ones, in order to optimise the processes of integration by knowing their effects on the chemical composition of the used materials. The formation of a superficial layer enriched in fluorine on $SiOCH$ samples after etching and HF cleaning was observed. Restoration treatment effects on etched samples were also studied, and the main chemical features are associated with surface material enrichment with alkyl and organosilicate like film deposition. However, a direct relation between final sample dielectric constant and chemical characteristics could not be established. This aspect was probably limited by the inability to detect surface $Si-OH$ groups induced by plasma etching considered to be one of the principal causes of water uptake in dielectric materials. Another line of approach could be the extension of the chemical range of secondary ions detected; intentionally limited to low mass fragments by selecting monoatomic Bi^+ as analysis beam. By this approach, a more complex molecular information could be much more instructive.

GENERAL CONCLUSION AND PERSPECTIVES

The initial objective of this work was to verify and validate the ToF-SIMS as a reliable technique for the chemical characterisation of a material family as "fragile" and assess the consistency of this chemical information

A first category of materials, porous silicon (p-Si), was studied. A set of mesoporous samples with a varying overall porosity was characterised–using different sputtering conditions.

Various but significant impacts have been evidenced. Morphological changes and sputter rates variation depending on the overall porosity and analysis setting used revealed the threshold behaviour at around 50% of porosity separating two distinct morphological modifications on surface:

(i) under 50% a pore sealing and surface densification and

(ii) above 50% a pore coalescence and preferential sputtering of thin solid membranes in between columnar pores in the sense of the sputtering ion flux.

More specific behaviours were observed concerning the generated secondary ion information that were shown to be significantly dependent on the applied sputtering energy for reactive sources. Concerning noble gas sputtering sources, the impact of sputtering energy on the secondary ion information was limited and data variations were mainly function of the sample porosity.

The second category of materials studied were composed of nanometric thick polymer films. The ability of new generation primary ion sources to reduce the sample damaging during analysis and obtain a rich secondary ion information was explored for the

characterisation of thin methacrylate films deposited by an innovative CVD technique (i-CVD).

The capability to depth profile such polymeric samples using large argon clusters allowed to profile stack samples composed of thin layers with quasi-identical chemistries, opening the access also to the development of a co-polymer quantification method. In addition, ToF-SIMS was also applied for the characterisation of samples of different molecular weights but same chemical composition. The possibility to discriminate sample chemistries and rely them to the M_w variations by coupling acquired spectra to multivariate analysis methods was shown to be very efficient. A reliable linear correlation was established between principal component scores and M_w.

The path through the chemical information reliability acquired by SIMS was accomplished by analysing low dielectric constant insulators (low-*k*).

Argon cluster polyatomic sources and monoatomic reactive ion sources were applied for cross-linked material depth profiling and results were compared. It was demonstrated that cross-linked materials can be sputtered with cluster sources but sputter rates and depth resolution were reduced due to the higher density of primary chemical bonds compares to linear polymers. A better depth resolution was achieved while depth profiling dielectric materials by low energy caesium gun.

In addition, spectra analysis coupled to principal component analysis approach partially allowed to combine the variation of physical properties (dielectric constant) with the chemicals ones, in order to optimise the processes of integration by knowing their effects on the chemical composition of the used materials.

It was shown than ToF-SIMS technique can be successfully applied for the characterisation of “fragile” materials producing a reliable and useful chemical information and the acquired secondary information is seriously impacted by analysis settings.

Considering perspectives for future works, an interesting effort could be made for adapted sputtering and thermodynamic simulations in order to understand and interpret further the ion/matter interaction in “fragile” materials,. Furthermore, in this work, the nature of samples has been intentionally restrained, but an interesting perspective would be the enlargement of the sample sets to similar structures such as nano or macro-porous inorganic samples and a wider range of polymers and molecular weights.

REFERENCES

1. Föll, H., M. Christophersen, J. Carstensen, and G. Hasse, *Formation and application of porous silicon.* Materials Science and Engineering: R: Reports, 2002. **39**(4): p. 93-141.
2. Paszti, F. and G. Battistig, *Ion Beam Characterisation and Modification of Porous Silicon.* physica status solidi (a), 2000. **182**(1): p. 271-278.
3. Fastow, R., Y. Maron, and J. Mayer, *Pulsed ion-beam melting of silicon.* Phys Rev B Condens Matter, 1985. **31**(2): p. 893-898.
4. Yang, L., M.P. Seah, I.S. Gilmore, R.J.H. Morris, M.G. Dowsett, L. Boarino, K. Sparnacci, and M. Laus, *Depth Profiling and Melting of Nanoparticles in Secondary Ion Mass Spectrometry (SIMS).* The Journal of Physical Chemistry C, 2013. **117**(31): p. 16042-16052.
5. Terlier, T., *Analyse par ToF-SIMS de matériaux organiques pour les applications en électronique organique*. 2014, Université Lyon 1.
6. Yagüe, J.L., A.M. Coclite, C. Petruczok, and K.K. Gleason, *Chemical Vapor Deposition for Solvent-Free Polymerization at Surfaces.* Macromolecular Chemistry and Physics, 2013. **214**(3): p. 302-312.
7. Bletsos, I.V., D.M. Hercules, J.H. Magill, D. VanLeyen, E. Niehuis, and A. Benninghoven, *Time-of-flight secondary ion mass spectrometry: detection of fragments from thick polymer films in the range m/z .ltoreq. 4500.* Analytical Chemistry, 1988. **60**(9): p. 938-944.
8. Bletsos, I.V., D.M. Hercules, D. VanLeyen, and A. Benninghoven, *Time-of-flight secondary ion mass spectrometry of polymers in the mass range 500-10000.* Macromolecules, 1987. **20**(2): p. 407-413.
9. Honig, R.E., *The Growth of Secondary Ion Mass Spectrometry (SIMS): A Personal View of Its Development*, in *Secondary Ion Mass Spectrometry SIMS V*, A. Benninghoven, et al., Editors. 1986, Springer Berlin Heidelberg. p. 2-15.
10. Vickerman, J.C. and D. Briggs, *ToF-SIMS: Material analysis by mass spectrometry 2nd edition*. 2013: impublications.
11. Storms, H.A., K.F. Brown, and J.D. Stein, *Evaluation of a cesium positive ion source for secondary ion mass spectrometry.* Analytical Chemistry, 1977. **49**(13): p. 2023-2030.
12. Lake, L.R. and K. Mauersberger, *Investigation of atomic oxygen in mass spectrometer ion sources.* International Journal of Mass Spectrometry and Ion Physics, 1974. **13**(4): p. 425-436.

13. Nagy, G. and A.V. Walker, *Enhanced secondary ion emission with a bismuth cluster ion source.* International Journal of Mass Spectrometry, 2007. **262**(1–2): p. 144-153.
14. Benguerba, M., A. Brunelle, S. Della-Negra, J. Depauw, H. Joret, Y. Le Beyec, M.G. Blain, E.A. Schweikert, G.B. Assayag, and P. Sudraud, *Impact of slow gold clusters on various solids: nonlinear effects in secondary ion emission.* Nuclear Instruments and Methods in Physics Research Section B: Beam Interactions with Materials and Atoms, 1991. **62**(1): p. 8-22.
15. Weibel, D., S. Wong, N. Lockyer, P. Blenkinsopp, R. Hill, and J.C. Vickerman, *A C60 primary ion beam system for time of flight secondary ion mass spectrometry: its development and secondary ion yield characteristics.* Analytical Chemistry, 2003. **75**(7): p. 1754-1764.
16. Yamada, I., J. Matsuo, N. Toyoda, and A. Kirkpatrick, *Materials processing by gas cluster ion beams.* Materials Science and Engineering: R: Reports, 2001. **34**(6): p. 231-295.
17. Razo, I.B., S. Sheraz, A. Henderson, N.P. Lockyer, and J.C. Vickerman, *Mass spectrometric imaging of brain tissue by time-of-flight secondary ion mass spectrometry--How do polyatomic primary beams C_{60}^+, Ar_{2000}^+, water-doped Ar_{2000}^+ and $H_2O_{2000}^+$ compare?* Rapid Commun Mass Spectrom, 2015. **29**(20): p. 1851-62.
18. Muramoto, S., J. Brison, and D.G. Castner, *Exploring the surface sensitivity of TOF-secondary ion mass spectrometry by measuring the implantation and sampling depths of Bi(n) and C60 ions in organic films.* Anal Chem, 2012. **84**(1): p. 365-72.
19. Vickerman, J.C. and D. Briggs, *ToF-SIMS: Materials Analysis by Mass Spectrometry*.
20. Benninghoven, A., F.G. Rüdenauer, and H.W. Werner, *Secondary Ion Mass Spectrometry: Basic Concepts, Instrumental Aspects, Applications, and Trends*. 1987: Wiley.
21. Davies, N., D.E. Weibel, P. Blenkinsopp, N. Lockyer, R. Hill, and J.C. Vickerman, *Development and experimental application of a gold liquid metal ion source.* Applied Surface Science, 2003. **203**: p. 223-227.
22. Lee, J.L., S. Ninomiya, J. Matsuo, I.S. Gilmore, M.P. Seah, and A.G. Shard, *Organic depth profiling of a nanostructured delta layer reference material using large argon cluster ions.* Anal Chem, 2010. **82**(1): p. 98-105.
23. Hofer, W.O., *Angular, energy, and mass distribution of sputtered particles*, in *Sputtering by Particle Bombardment III*, K. Eds.: R. Behrisch and Wittmaack), Editors. 1991. p. 15-90.
24. Delcorte, A., C. Leblanc, C. Poleunis, and K. Hamraoui, *Computer Simulations of the Sputtering of Metallic, Organic, and Metal–Organic Surfaces with Binand C60Projectiles.* The Journal of Physical Chemistry C, 2013. **117**(6): p. 2740-2752.
25. Seah, M.P., C.A. Clifford, F.M. Green, and I.S. Gilmore, *An accurate semi-empirical equation for sputtering yields I: for argon ions.* Surface and Interface Analysis, 2005. **37**(5): p. 444-458.
26. Sigmund, P., *Theory of Sputtering. I. Sputtering Yield of Amorphous and Polycrystalline Targets.* Physical Review, 1969. **184**(2): p. 383-416.
27. Seah, M.P., *An accurate semi-empirical equation for sputtering yields, II: for neon, argon and xenon ions.* Nuclear Instruments and Methods in Physics Research Section B: Beam Interactions with Materials and Atoms, 2005. **229**(3-4): p. 348-358.

28. Matsunami, N., Y. Yamamura, Y. Itikawa, N. Itoh, Y. Kazumata, S. Miyagawa, K. Morita, R. Shimizu, and H. Tawara, *Energy-Dependence of the Ion-Induced Sputtering Yields of Monatomic Solids.* Atomic Data and Nuclear Data Tables, 1984. **31**(1): p. 1-80.
29. Nagy, G., L.D. Gelb, and A.V. Walker, *An investigation of enhanced secondary ion emission under Au_n^+ (n = 1-7) bombardment.* J Am Soc Mass Spectrom, 2005. **16**(5): p. 733-42.
30. Medvedeva, M., I. Wojciechowski, and B.J. Garrison, *Effect of mass and incidence angle of keV energy polyatomic projectiles in silicon sputtering.* Surface Science, 2002. **505**: p. 349-357.
31. Samartsev, A.V., A. Duvenbeck, and A. Wucher, *Sputtering of indium using Au_m projectiles: Transition from linear cascade to spike regime.* Physical Review B, 2005. **72**(11): p. 115417.
32. Kersting, R., B. Hagenhoff, F. Kollmer, R. Möllers, and E. Niehuis, *Influence of primary ion bombardment conditions on the emission of molecular secondary ions.* Applied Surface Science, 2004. **231–232**: p. 261-264.
33. Bouneau, S., A. Brunelle, S. Della-Negra, J. Depauw, D. Jacquet, Y. Le Beyec, M. Pautrat, M. Fallavier, J.C. Poizat, and H.H. Andersen, *Very large gold and silver sputtering yields induced by keV to MeV energy Au_n clusters (n=1-13).* Physical Review B, 2002. **65**(14): p. 144106.
34. Seah, M.P., *Universal Equation for Argon Gas Cluster Sputtering Yields.* The Journal of Physical Chemistry C, 2013. **117**(24): p. 12622-12632.
35. Sjövall, P., D. Rading, S. Ray, L. Yang, and A.G. Shard, *Sample Cooling or Rotation Improves C_{60} Organic Depth Profiles of Multilayered Reference Samples: Results from a VAMAS Interlaboratory Study.* The Journal of Physical Chemistry B, 2010. **114**(2): p. 769-774.
36. Mahoney, C.M., A.J. Fahey, and G. Gillen, *Temperature-Controlled Depth Profiling of Poly(methyl methacrylate) Using Cluster Secondary Ion Mass Spectrometry. 1. Investigation of Depth Profile Characteristics.* Analytical Chemistry, 2007. **79**(3): p. 828-836.
37. Möllers, R., N. Tuccitto, V. Torrisi, E. Niehuis, and A. Licciardello, *Chemical effects in C60 irradiation of polymers.* Applied Surface Science, 2006. **252**(19): p. 6509-6512.
38. Garrison, B.J. and Z. Postawa, *Computational view of surface based organic mass spectrometry.* Mass Spectrom Rev, 2008. **27**(4): p. 289-315.
39. Delcorte, A., *Organic surfaces excited by low-energy ions: atomic collisions, molecular desorption and buckminsterfullerenes.* Phys Chem Chem Phys, 2005. **7**(19): p. 3395-406.
40. Delcorte, A., V. Cristaudo, V. Lebec, and B. Czerwinski, *Sputtering of polymers by keV clusters: Microscopic views of the molecular dynamics.* International Journal of Mass Spectrometry, 2014. **370**: p. 29-38.
41. Delcorte, A., B.G. Segda, B.J. Garrison, and P. Bertrand, *Inferring ejection distances and a surface energy profile in keV particle bombardment experiments.* Nuclear Instruments & Methods in Physics Research Section B-Beam Interactions with Materials and Atoms, 2000. **171**(3): p. 277-290.
42. Kersting, R., B. Hagenhoff, F. Kollmer, R. Mollers, and E. Niehuis, *Influence of primary ion bombardment conditions on the emission of molecular secondary ions.* Applied Surface Science, 2004. **231**: p. 261-264.
43. Robinson, M.A., *Chemical Analysis of Cells and Tissues with Time-of-Flight Secondary Ion Mass Spectrometry*, in *Department of Chemical Engineering*. 2013, University of Washington.

44. Lianos, L., C. Quet, and T.M. Duc, *Surface structural studies of polyethylene, polypropylene and their copolymers with ToF SIMS.* Surface and Interface Analysis, 1994. **21**(1): p. 14-22.
45. Graham, D.J. and D.G. Castner, *Multivariate analysis of ToF-SIMS data from multicomponent systems: the why, when, and how*. Biointerphases, 2012. **7**(1-4): p. 49.
46. Leggett, G.J., B.D. Ratner, and J.C. Vickerman, *Characterization of plasma-deposited styrene films by XPS and static SIMS.* Surface and Interface Analysis, 1995. **23**(1): p. 22-28.
47. Leggett, G.J., J.C. Vickerman, and D. Briggs, *Applications of tandem quadrupole mass spectrometry in SIMS.* Surface and Interface Analysis, 1990. **16**(1-12): p. 3-8.
48. Benninghoven, A., *Chemical-Analysis of Inorganic and Organic-Surfaces and Thin-Films by Static Time-of-Flight Secondary-Ion Mass-Spectrometry (Tof-Sims).* Angewandte Chemie-International Edition in English, 1994. **33**(10): p. 1023-1043.
49. Bletsos, I.V., D.M. Hercules, D. Vanleyen, B. Hagenhoff, E. Niehuis, and A. Benninghoven, *Molecular-Weight Distributions of Polymers Using Time-of-Flight Secondary-Ion Mass-Spectrometry.* Analytical Chemistry, 1991. **63**(18): p. 1953-1960.
50. Delcorte, A. and P. Bertrand, *Sputtering of parent-like ions from large organic adsorbates on metals under keV ion bombardment.* Surface Science, 1998. **412-413**: p. 97-124.
51. Delcorte, A., P. Bertrand, and B.J. Garrison, *Collision cascade and sputtering process in a polymer.* Journal of Physical Chemistry B, 2001. **105**(39): p. 9474-9486.
52. Paruch, R.J., B.J. Garrison, and Z. Postawa, *Partnering Analytic Models and Dynamic Secondary Ion Mass Spectrometry Simulations to Interpret Depth Profiles Due to Kiloelectronvolt Cluster Bombardment.* Analytical Chemistry, 2012. **84**(6): p. 3010-3016.
53. Postawa, Z., *Sputtering simulations of organic overlayers on metal substrates by monoatomic and clusters projectiles.* Applied Surface Science, 2004. **231–232**: p. 22-28.
54. Mahoney, C.M., A.J. Fahey, G. Gillen, C. Xu, and J.D. Batteas, *Temperature-controlled depth profiling in polymeric materials using cluster secondary ion mass spectrometry (SIMS).* Applied Surface Science, 2006. **252**(19): p. 6502-6505.
55. Mahoney, C.M., *Cluster secondary ion mass spectrometry of polymers and related materials.* Mass Spectrom Rev, 2010. **29**(2): p. 247-93.
56. Ninomiya, S., T. Aoki, T. Seki, and J. Matsuo, *Secondary ion measurements for oxygen cluster ion SIMS.* Applied Surface Science, 2006. **252**(19): p. 7290-7292.
57. Sheraz, S., A. Barber, I. Berrueta Razo, J.S. Fletcher, N.P. Lockyer, and J.C. Vickerman, *Prospect of increasing secondary ion yields in ToF-SIMS using water cluster primary ion beams.* Surface and Interface Analysis, 2014. **46**(S1): p. 51-53.
58. Houssiau, L. and N. Mine, *Molecular depth profiling of polymers with very low energy reactive ions.* Surface and Interface Analysis, 2010. **42**(8): p. 1402-1408.
59. Detter, L.D., O.W. Hand, R.G. Cooks, and R.A. Walton, *Interfacial Chemical-Reactions Accompanying Desorption Ionization Mass-Spectrometry.* Mass Spectrometry Reviews, 1988. **7**(5): p. 465-502.

60. Wittmaack, K., *Unravelling the secrets of Cs controlled secondary ion formation: Evidence of the dominance of site specific surface chemistry, alloying and ionic bonding.* Surface Science Reports, 2013. **68**(1): p. 108-230.
61. Wittmaack, K., *Artifacts in low-energy depth profiling using oxygen primary ion beams: Dependence on impact angle and oxygen flooding conditions.* Journal of Vacuum Science & Technology B: Microelectronics and Nanometer Structures, 1998. **16**(5): p. 2776.
62. Vandervorst, W., T. Janssens, C. Huyghebaert, and B. Berghmans, *The fate of the (reactive) primary ion: Sputtering and desorption.* Applied Surface Science, 2008. **255**(4): p. 1206-1214.
63. Berghmans, B., B. Van Daele, L. Geenen, T. Conard, A. Franquet, and W. Vandervorst, *Cesium near-surface concentration in low energy, negative mode dynamic SIMS.* Applied Surface Science, 2008. **255**(4): p. 1316-1319.
64. Vickerman, J.C., *Secondary ion mass spectrometry-basic concepts, instrumental aspects, applications and trends. A. BENNINGHOVEN, F. G. RUDENAUER and H. W. WERNER, Wiley, New York, 1987, 1277 pages.* Surface and Interface Analysis, 1987. **10**(8): p. 435-435.
65. Wittmaack, K., *Mechanism of MCs+ formation in Cs based secondary ion mass spectrometry.* Surface Science, 2012. **606**(3-4): p. L18-L21.
66. Williams, P., *The sputtering process and sputtered ion emission.* Surface Science, 1979. **90**(2): p. 588-634.
67. Berghmans, B. and W. Vandervorst, *The effect of oxygen during irradiation of silicon with low energy Cs[sup +] ions.* Journal of Applied Physics, 2009. **106**(3): p. 033509.
68. Verhoef, R.W. and M. Asscher, *The work function of adsorbed alkalis on metals revisited: a coverage-dependent polarizability approach.* Surface Science, 1997. **391**(1-3): p. 11-18.
69. Brison, J., N. Mine, S. Poisseroux, B. Douhard, R.G. Vitchev, and L. Houssiau, *Measurement and modeling of work function changes during low energy cesium sputtering.* Surface Science, 2007. **601**(6): p. 1467-1472.
70. Wittmaack, K., *Mechanisms responsible for inducing and balancing the presence of Cs adatoms in dynamic Cs based SIMS.* International Journal of Mass Spectrometry, 2012. **313**: p. 68-72.
71. Giordani, A., J. Tuggle, C. Winkler, and J. Hunter, *On the evolution of Cs droplets in SIMS craters.* Surface and Interface Analysis, 2014. **46**(S1): p. 43-45.
72. Ngo, K.Q., P. Philipp, J. Kieffer, and T. Wirtz, *Cs oxide aggregation in SIMS craters in organic samples for optoelectronic application.* Surface Science, 2012. **606**(15-16): p. 1244-1251.
73. Douglas, M.A. and P.J. Chen, *Quantitative trace metal analysis of silicon surfaces by ToF-SIMS.* Surface and Interface Analysis, 1998. **26**(13): p. 984-994.
74. Liu, K.S.S., C.W. Yong, B.J. Garrison, and J.C. Vickerman, *Molecular Dynamics Simulations of Particle Bombardment Induced Desorption Processes: Alkanethiolates on Au(111).* The Journal of Physical Chemistry B, 1999. **103**(16): p. 3195-3205.
75. Feld, H., A. Leute, R. Zurmuehlen, and A. Benninghoven, *Comparative and complementary plasma desorption mass spectrometry/secondary ion mass spectrometry investigations of polymer materials.* Analytical Chemistry, 1991. **63**(9): p. 903-910.
76. Shard, A.G., S.J. Spencer, S.A. Smith, R. Havelund, and I.S. Gilmore, *The matrix effect in organic secondary ion mass spectrometry.* International Journal of Mass Spectrometry, 2015. **377**: p. 599-609.

77. Seah, M.P., R. Havelund, A.G. Shard, and I.S. Gilmore, *Sputtering Yields for Mixtures of Organic Materials Using Argon Gas Cluster Ions.* J Phys Chem B, 2015. **119**(42): p. 13433-9.
78. Baklanov, M.R., J.-F. de Marneffe, D. Shamiryan, A.M. Urbanowicz, H. Shi, T.V. Rakhimova, H. Huang, and P.S. Ho, *Plasma processing of low-k dielectrics.* Journal of Applied Physics, 2013. **113**(4): p. 041101.
79. Uhlir, A., *Electrolytic Shaping of Germanium and Silicon.* Bell System Technical Journal, 1956. **35**(2): p. 333-347.
80. Calliari, L., M. Anderle, M. Ceschini, L. Pavesi, G. Mariotto, and O. Bisi, *Electron-Bombardment Effects on Light-Emitting Porous Silicon.* Journal of Luminescence, 1993. **57**(1-6): p. 83-87.
81. Borini, S., G. Amato, M. Rocchia, L. Boarino, and A.M. Rossi, *Electron-beam irradiation of porous silicon: Application to micromachining.* Journal of Applied Physics, 2003. **93**(8): p. 4439-4441.
82. Bisi, O., S. Ossicini, and L. Pavesi, *Porous silicon: a quantum sponge structure for silicon based optoelectronics.* Surface Science Reports, 2000. **38**(1-3): p. 1-126.
83. Dittrich, T., I. Sieber, W. Henrion, S. Rauscher, N. Wanderka, and J. Rappich, *Selective laser induced melting of ultrathin nanoporous silicon layers.* Applied Physics a-Materials Science & Processing, 1996. **63**(5): p. 467-470.
84. Timoshenko, V.Y., T. Dittrich, I. Sieber, J. Rappich, B.V. Kamenev, and P.K. Kashkarov, *Laser-Induced Melting of Porous Silicon.* physica status solidi (a), 2000. **182**(1): p. 325-330.
85. Northen, T.R., H.K. Woo, M.T. Northen, A. Nordstrom, W. Uritboonthail, K.L. Turner, and G. Siuzdak, *High surface area of porous silicon drives desorption of intact molecules.* J Am Soc Mass Spectrom, 2007. **18**(11): p. 1945-9.
86. Hua, X.F., C. Stolz, G.S. Oehrlein, P. Lazzeri, N. Coghe, M. Anderle, C.K. Inoki, T.S. Kuan, and P. Jiang, *Plasma-surface interactions of nanoporous silica during plasma-based pattern transfer using C_4F_8 and C_4F_8/Ar gas mixtures.* Journal of Vacuum Science & Technology A, 2005. **23**(1): p. 151-164.
87. Farrell, H.H., *Surface bonding effects in compound semiconductor nanoparticles: II.* Journal of Vacuum Science & Technology B, 2008. **26**(4): p. 1534-1541.
88. Farrell, H.H. and C.D. Van Siclen, *Binding energy, vapor pressure, and melting point of semiconductor nanoparticles.* Journal of Vacuum Science & Technology B, 2007. **25**(4): p. 1441-1447.
89. Yang, L., M.P. Seah, E.H. Anstis, I.S. Gilmore, and J.L.S. Lee, *Sputtering Yields of Gold Nanoparticles by C60Ions.* The Journal of Physical Chemistry C, 2012. **116**(16): p. 9311-9318.
90. Lau, K.K.S. and K.K. Gleason, *Initiated Chemical Vapor Deposition (iCVD) of Poly(alkyl acrylates): An Experimental Study.* Macromolecules, 2006. **39**(10): p. 3688-3694.
91. Lau, K.K.S. and K.K. Gleason, *Initiated Chemical Vapor Deposition (iCVD) of Poly(alkyl acrylates): A Kinetic Model.* Macromolecules, 2006. **39**(10): p. 3695-3703.
92. Gillen, G., M. Walker, P. Thompson, and J. Bennett, *Use of an SF5+ polyatomic primary ion beam for ultrashallow depth profiling on an ion microscope secondary ion mass spectroscopy instrument.* Journal of Vacuum Science & Technology B, 2000. **18**(1): p. 503-508.
93. Wagner, M.S., *Impact Energy Dependence of SF5+-Induced Damage in Poly(methyl methacrylate) Studied Using Time-of-Flight Secondary Ion Mass Spectrometry.* Analytical Chemistry, 2004. **76**(5): p. 1264-1272.

94. Cheng, J. and N. Winograd, *Depth profiling of peptide films with TOF-SIMS and a C60 probe.* Anal Chem, 2005. **77**(11): p. 3651-9.
95. Havelund, R., A. Licciardello, J. Bailey, N. Tuccitto, D. Sapuppo, I.S. Gilmore, J.S. Sharp, J.L. Lee, T. Mouhib, and A. Delcorte, *Improving secondary ion mass spectrometry C60(n+) sputter depth profiling of challenging polymers with nitric oxide gas dosing.* Anal Chem, 2013. **85**(10): p. 5064-70.
96. Nakagiri, M., N. Toyoda, I. Yamada, J. Matsuo, M. Kase, T. Aoki, and T. Seki, *X-ray photoelectron spectroscopy analysis of organic materials irradiated with gas cluster ion beam.* AIP Conference Proceedings, 2011. **1321**(1): p. 321-324.
97. Matsuo, J., S. Ninomiya, Y. Nakata, Y. Honda, K. Ichiki, T. Seki, and T. Aoki, *What size of cluster is most appropriate for SIMS?* Applied Surface Science, 2008. **255**(4): p. 1235-1238.
98. Shard, A.G., R. Havelund, M.P. Seah, S.J. Spencer, I.S. Gilmore, N. Winograd, D. Mao, T. Miyayama, E. Niehuis, D. Rading, and R. Moellers, *Argon cluster ion beams for organic depth profiling: results from a VAMAS interlaboratory study.* Anal Chem, 2012. **84**(18): p. 7865-73.
99. Yamamoto, Y., K. Ichiki, T. Seki, T. Aoki, and J. Matsuo, *Ion-induced damage evaluation with Ar cluster ion beams.* Surface and Interface Analysis, 2013. **45**(1): p. 167-170.
100. Cristaudo, V., C. Poleunis, B. Czerwinski, and A. Delcorte, *Ar cluster sputtering of polymers: effects of cluster size and molecular weights.* Surface and Interface Analysis, 2014. **46**(S1): p. 79-82.
101. Seah, M.P., *Argon cluster size-dependence of sputtering yields of polymers: molecular weights and the universal equation.* Surface and Interface Analysis, 2015. **47**(1): p. 169-172.
102. Houssiau, L., B. Douhard, and N. Mine, *Molecular depth profiling of polymers with very low energy ions.* Applied Surface Science, 2008. **255**(4): p. 970-972.
103. Houssiau, L. and N. Mine, *Molecular depth profiling with reactive ions, or why chemistry matters in sputtering.* Surface and Interface Analysis, 2011. **43**(1-2): p. 146-150.
104. Fleischmann, C., T. Conard, R. Havelund, A. Franquet, C. Poleunis, E. Voroshazi, A. Delcorte, and W. Vandervorst, *Fundamental aspects of Arn+SIMS profiling of common organic semiconductors.* Surface and Interface Analysis, 2014. **46**(S1): p. 54-57.
105. Yoshiyuki, K., W. Akira, K. Takuya, S. Miku, N. Toshihisa, and S. Seiji, *Non-porous ultra-low- k SiOCH (k = 2.3) for damage-free integration and Cu diffusion barrier.* Journal of Physics D: Applied Physics, 2013. **46**(39): p. 395203.
106. Grunenwald, A., *Synthesis and characterisation of dielectric thin films with structured porosity obtained by sol gel and plasma route*. 2011, Ecole Nationale Supérieure de Chimie de Montpellier.
107. Lépinay, M., J., *Impact of plasma treatments and cleaning chemistries on a porous low-k dielectric used for interconnects*. 2014, Université Montpellier 2.
108. Shamiryan, D., M.R. Baklanov, S. Vanhaelemeersch, and K. Maex, *Comparative study of SiOCH low-k films with varied porosity interacting with etching and cleaning plasma.* Journal of Vacuum Science & Technology B: Microelectronics and Nanometer Structures, 2002. **20**(5): p. 1923.
109. Lazzeri, P., X. Hua, G.S. Oehrlein, M. Barozzi, E. Iacob, and M. Anderle, *Porosity-induced effects during C_4F_8/90% Ar plasma etching of silica-based ultralow-k dielectrics.* Journal of Vacuum Science & Technology B: Microelectronics and Nanometer Structures, 2005. **23**(4): p. 1491.

110. Li, Y., I. Ciofi, L. Carbonell, N. Heylen, J. Van Aelst, M.l.R. Baklanov, G. Groeseneken, K. Maex, and Z. Tőkei, *Influence of absorbed water components on SiOCH low-k reliability.* Journal of Applied Physics, 2008. **104**(3): p. 034113.
111. Xie, B. and A.J. Muscat, *The restoration of porous methylsilsesquioxane (p-MSQ) films using trimethylhalosilanes dissolved in supercritical carbon dioxide.* Microelectronic Engineering, 2005. **82**(3-4): p. 434-440.
112. Fischer, T., N. Ahner, S. Zimmermann, M. Schaller, and S.E. Schulz, *Influence of thermal cycles on the silylation process for recovering k-value and chemical structure of plasma damaged ultra-low-k materials.* Microelectronic Engineering, 2012. **92**(0): p. 53-58.
113. Tang, X., R. Beavis, W. Ens, F. Lafortune, B. Schueler, and K.G. Standing, *A secondary ion time-of-flight mass spectrometer with an ion mirror.* International Journal of Mass Spectrometry and Ion Processes, 1988. **85**(1): p. 43-67.
114. Niehuis, E., *Design and performance of a reflectron based time-of-flight secondary ion mass spectrometer with electrodynamic primary ion mass separation.* Journal of Vacuum Science & Technology A: Vacuum, Surfaces, and Films, 1987. **5**(4): p. 1243.
115. Wagner, M.S., D.J. Graham, B.D. Ratner, and D.G. Castner, *Maximizing information obtained from secondary ion mass spectra of organic thin films using multivariate analysis.* Surface Science, 2004. **570**(1-2): p. 78-97.
116. Graham, D.J., M.S. Wagner, and D.G. Castner, *Information from complexity: Challenges of TOF-SIMS data interpretation.* Applied Surface Science, 2006. **252**(19): p. 6860-6868.
117. Geladi, P., M. Manley, and T. Lestander, *Scatter plotting in multivariate data analysis.* Journal of Chemometrics, 2003. **17**(8-9): p. 503-511.
118. Coullerez, G., D. Léonard, S. Lundmark, and H.J. Mathieu, *XPS and ToF-SIMS study of freeze-dried and thermally cured melamine–formaldehyde resins of different molar ratios.* Surface and Interface Analysis, 2000. **29**(7): p. 431-443.
119. Gupta, P., A.C. Dillon, A.S. Bracker, and S.M. George, *FTIR studies of H2O and D2O decomposition on porous silicon surfaces.* Surface Science, 1991. **245**(3): p. 360-372.
120. Dillon, A.C., *Diethylsilane Decomposition on Silicon Surfaces Studied Using Transmission FTIR Spectroscopy.* Journal of The Electrochemical Society, 1992. **139**(2): p. 537.
121. Erson, R.C., R.S. Muller, and C.W. Tobias, *Investigations of porous silicon for vapor sensing.* Sensors and Actuators A: Physical, 1990. **23**(1-3): p. 835-839.
122. Canham, L.T., *Bioactive silicon structure fabrication through nanoetching techniques.* Advanced Materials, 1995. **7**(12): p. 1033-&.
123. Peng, K.-Q., X. Wang, and S.-T. Lee, *Gas sensing properties of single crystalline porous silicon nanowires.* Applied Physics Letters, 2009. **95**(24): p. 243112.
124. Baratto, C., G. Faglia, E. Comini, G. Sberveglieri, A. Taroni, V. La Ferrara, L. Quercia, and G. Di Francia, *A novel porous silicon sensor for detection of sub-ppm NO2 concentrations.* Sensors and Actuators B-Chemical, 2001. **77**(1-2): p. 62-66.
125. Sujatha, L., V.S. Kale, and E. Bhattacharya, *Critical study of high-sensitivity pressure sensors with silicon/porous silicon composite membranes.* Journal of Micro-Nanolithography Mems and Moems, 2009. **8**(3): p. 033070-033070-8.
126. Abrashova, E.V., I.E. Kononova, V.A. Moshnikov, and S.S. Nalimova, *Sol-gel synthesis of Pb-free thin-film nanomaterials for electrocaloric devices.* 16th Russian Youth Conference on Physics and Astronomy (Physica.Spb/2013), 2014. **572**.

127. Moshnikov, V.A., I. Gracheva, A.S. Lenshin, Y.M. Spivak, M.G. Anchkov, V.V. Kuznetsov, and J.M. Olchowik, *Porous silicon with embedded metal oxides for gas sensing applications.* Journal of Non-Crystalline Solids, 2012. **358**(3): p. 590-595.
128. Desplobain, S., G. Gautier, J. Semai, L. Ventura, and M. Roy, *Investigations on porous silicon as electrode material in electrochemical capacitors.* physica status solidi (c), 2007. **4**(6): p. 2180-2184.
129. Muller, P., *IUPAC Manual of Symbols and Technology*. 1973.
130. Canham, L.T., A.G. Cullis, C. Pickering, O.D. Dosser, T.I. Cox, and T.P. Lynch, *Luminescent anodized silicon aerocrystal networks prepared by supercritical drying.* Nature, 1994. **368**(6467): p. 133-135.
131. Xifré Pérez, E., *DESIGN, FABRICATION AND CHARACTERIZATION OF POROUS SILICON MULTILAYER OPTICAL DEVICES*. 2007, Universitat Rovira i Virgili.
132. Boarino, L., C. Baratto, F. Geobaldo, G. Amato, E. Comini, A.M. Rossi, G. Faglia, G. Lerondel, and G. Sberveglieri, *NO2 monitoring at room temperature by a porous silicon gas sensor.* Materials Science and Engineering B-Solid State Materials for Advanced Technology, 2000. **69**(0): p. 210-214.
133. Oakes, L., A. Westover, J.W. Mares, S. Chatterjee, W.R. Erwin, R. Bardhan, S.M. Weiss, and C.L. Pint, *Surface engineered porous silicon for stable, high performance electrochemical supercapacitors.* Sci Rep, 2013. **3**: p. 3020.
134. Gautier, G. and P. Leduc, *Porous silicon for electrical isolation in radio frequency devices: A review.* Applied Physics Reviews, 2014. **1**(1): p. 011101.
135. Gautier, G., T. Defforge, S. Desplobain, J. Billoue, M. Capelle, P. Poveda, K. Vanga, B. Lu, B. Bardet, J. Lascaud, C. Seck, A. Fevre, S. Menard, and L. Ventura, *Porous Silicon in Microelectronics: From Academic Studies to Industry.* ECS Transactions, 2015. **69**(2): p. 123-134.
136. Whitehead, M.A., D. Fan, P. Mukherjee, G.R. Akkaraju, L.T. Canham, and J.L. Coffer, *High-porosity poly(epsilon-caprolactone)/mesoporous silicon scaffolds: calcium phosphate deposition and biological response to bone precursor cells.* Tissue Eng Part A, 2008. **14**(1): p. 195-206.
137. Jarvis, K.L., T.J. Barnes, and C.A. Prestidge, *Surface chemistry of porous silicon and implications for drug encapsulation and delivery applications.* Adv Colloid Interface Sci, 2012. **175**(0): p. 25-38.
138. Mula, G., L. Loddo, E. Pinna, M. Tiddia, M. Mascia, S. Palmas, R. Ruffilli, and A. Falqui, *Controlling the Er content of porous silicon using the doping current intensity.* Nanoscale Research Letters, 2014. **9**(1): p. 332.
139. Vitanov, R., E. Goranova, V. Stavrov, P. Ivanov, and P.K. Singh, *Fabrication of buried contact silicon solar cells using porous silicon.* Solar Energy Materials and Solar Cells, 2009. **93**(3): p. 297-300.
140. Henstock, J.R., L.T. Canham, and S.I. Anderson, *Silicon: the evolution of its use in biomaterials.* Acta Biomater, 2015. **11**(0): p. 17-26.
141. Jeske, M., J.W. Schultze, and H. Munder, *Porous Silicon - Base Material for Nanotechnologies.* Electrochimica Acta, 1995. **40**(10): p. 1435-1438.
142. Kumar, P., *Effect of Silicon Crystal Size on Photoluminescence Appearance in Porous Silicon.* ISRN Nanotechnology, 2011. **2011**: p. 1-6.
143. Nalwa, H.S., Silicon Based Materials and Devices, 2001. **Vol. 2: Properties and Devices**: p. Academic Press, San Diego.
144. Hadj Zoubir, N., M. Vergnat, T. Delatour, A. Burneau, and P. de Donato, *Interpretation of the luminescence quenching in chemically etched porous silicon by the desorption of SiH3 species.* Applied Physics Letters, 1994. **65**(1): p. 82.

145. Borghesi, A., A. Sassella, B. Pivac, and L. Pavesi, *Characterization of Porous Silicon Inhomogeneities by High-Spatial-Resolution Infrared-Spectroscopy.* Solid State Communications, 1993. **87**(1): p. 1-4.
146. Loni, A., A.J. Simons, L.T. Canham, H.J. Phillips, and L.G. Earwaker, *Compositional variations of porous silicon layers prior to and during ion-beam analyses.* Journal of Applied Physics, 1994. **76**(5): p. 2825.
147. Printemps, T., G. Mula, D. Sette, P. Bleuet, V. Delaye, N. Bernier, A. Grenier, G. Audoit, N. Gambacorti, and L. Hervé, *Self-adapting denoising, alignment and reconstruction in electron tomography in materials science.* Ultramicroscopy, 2016. **160**: p. 23-34.
148. Bendler, B., P. Philipp, and T. Wirtz, *Neutral cesium deposition prior to SIMS depth profiling - preliminary results on organic samples.* Surface and Interface Analysis, 2013. **45**(1): p. 57-60.
149. Baboux, N., J.C. Dupuy, G. Prudon, P. Holliger, F. Laugier, A.M. Papon, and J.M. Hartmann, *Ultra-low energy SIMS analysis of boron deltas in silicon.* Journal of Crystal Growth, 2002. **245**(1-2): p. 1-8.
150. Ziegler, J.F., M.D. Ziegler, and J.P. Biersack, *SRIM – The stopping and range of ions in matter (2010).* Nuclear Instruments and Methods in Physics Research Section B: Beam Interactions with Materials and Atoms, 2010. **268**(11-12): p. 1818-1823.
151. Yamamura, Y. and H. Tawara, *Energy Dependence of Ion-Induced Sputtering Yields from Monatomic Solids at Normal Incidence.* Atomic Data and Nuclear Data Tables, 1996. **62**(2): p. 149-253.
152. Huynh, W.U., J.J. Dittmer, and A.P. Alivisatos, *Hybrid Nanorod-Polymer Solar Cells.* Science, 2002. **295**(5564): p. 2425-2427.
153. Steele, B.C.H. and A. Heinzel, *Materials for fuel-cell technologies.* Nature, 2001. **414**(6861): p. 345-352.
154. Tenhaeff, W.E. and K.K. Gleason, *Initiated and Oxidative Chemical Vapor Deposition of Polymeric Thin Films: iCVD and oCVD.* Advanced Functional Materials, 2008. **18**(7): p. 979-992.
155. Martin, T.P., K. Chan, and K.K. Gleason, *Combinatorial initiated chemical vapor deposition (iCVD) for polymer thin film discovery.* Thin Solid Films, 2008. **516**(5): p. 681-683.
156. Karaman, M. and N. Çabuk, *Initiated chemical vapor deposition of pH responsive poly(2-diisopropylamino)ethyl methacrylate thin films.* Thin Solid Films, 2012. **520**(21): p. 6484-6488.
157. Bonnet, L., *Couches minces de polymères obtenues par iCVD (initiated Chemical Vapor Deposition) appliquées sur des capteurs de gaz*. Université de Lyon.
158. Tenhaeff, W.E. and K.K. Gleason, *Initiated chemical vapor deposition of perfectly alternating poly(styrene-alt-maleic anhydride).* Surface and Coatings Technology, 2007. **201**(22–23): p. 9417-9421.
159. El Sabahy, J., J. Berthier, L. Bonnet, M. Matheron, T. Bordy, C. Yeromonahos, F. Ricoul, and V. Jousseaume, *Toluene-organic thin films partition coefficients analyzed with Langmuir adsorption theory and finite elements simulations.* Sensors and Actuators B: Chemical, 2014. **202**(0): p. 941-948.
160. Grate, J.W., *Acoustic wave microsensor arrays for vapor sensing.* Chem Rev, 2000. **100**(7): p. 2627-48.
161. Taglauter, E., *Surface cleaning using sputtering.* Applied Physics A: Surfaces And Multilayers, 1990. **51**(3): p. 238.
162. Shamiryan, D., T. Abell, F. Iacopi, and K. Maex, *Low-k dielectric materials.* Materials Today, 2004. **7**(1): p. 34-39.

163. Vasarla, N.S., *Mechanical Characterization of Black Diamond (Low-k) Structures for 3D Integrated Circuit and Packaging Applications, Nanoindentation in Materials Science*, in *Nanoindentation in Materials Science*, D.J. Nemecek, Editor. 2012.
164. Hatton, B.D., K. Landskron, W.J. Hunks, M.R. Bennett, D. Shukaris, D.D. Perovic, and G.A. Ozin, *Materials chemistry for low-k materials.* Materials Today, 2006. **9**(3): p. 22-31.
165. Hamioud, K., V. Arnal, A. Farcy, V. Jousseaume, A. Zenasni, B. Icard, J. Pradelles, S. Manakli, P. Brun, G. Imbert, C. Jayet, M. Assous, S. Maitrejean, D. Galpin, C. Monget, J. Guillan, S. Chhun, E. Richard, D. Barbier, and M. Haond, *32nm node BEOL integration with an extreme low-k porous SiOCH dielectric k=2.3.* Microelectronic Engineering, 2010. **87**(3): p. 316-320.
166. Lépinay, M., N. Djourelov, H. Marinov, L. Broussous, K. Courouble, C. Licitra, F. Bertin, V. Rouessac, and A. Ayral, *Depth-resolved impact of integration process on porosity and solvent diffusion in a SiOCH low-k material.* Journal of Porous Materials, 2014. **21**(4): p. 475-484.
167. Oszinda, T., M. Schaller, D. Fischer, C. Walsh, and S.E. Schulz, *Investigation of physical and chemical property changes of ultra low-κ SiOCH in aspect of cleaning and chemical repair processes.* Microelectronic Engineering, 2010. **87**(3): p. 457-461.
168. Ichiki, K., S. Ninomiya, Y. Nakata, H. Yamada, T. Seki, T. Aoki, and J. Matsuo, *Surface morphology of PMMA surfaces bombarded with size-selected gas cluster ion beams.* Surface and Interface Analysis, 2011. **43**(1-2): p. 120-122.
169. McGahay, V., *Porous Dielectrics in Microelectronic Wiring Applications.* Materials, 2010. **3**(1): p. 536-562.
170. Lépinay, M., D. Lee, R. Scarazzini, M. Bardet, M. Veillerot, L. Broussous, K. Courouble , C. Licitra , V. Jousseaume, F. Bertin , V. Rouessac , and A. Ayral *Impact of plasma reactive ion etching on low dielectric constant porous organosilicate films' microstructure and chemical composition.* Microporous and Mesoporous Materials, 2016.
171. Eslava, S., F. Iacopi, M.R. Baklanov, C.E. Kirschhock, K. Maex, and J.A. Martens, *Ultraviolet-assisted curing of polycrystalline pure-silica zeolites: hydrophobization, functionalization, and cross-linking of grains.* J Am Chem Soc, 2007. **129**(30): p. 9288-9.
172. Schroder, D.K., M.S. Fung, R.L. Verkuil, S. Pandey, W.H. Howland, and M. Kleefstra, *Corona-oxide-semiconductor device characterization.* Solid-State Electronics, 1998. **42**(4): p. 505-512.
173. Lazzeri, P., X. Hua, G. Oehrlein, E. Iacob, M. Barozzi, M. Bersani, and M. Anderle, *ToF-SIMS and AFM studies of low-k dielectric etching in fluorocarbon plasmas.* Applied Surface Science, 2006. **252**(19): p. 7186-7189.
174. Bo, X., K. Chan, D. Cui, R. He, D. Raj, E. Hollar, S. Baluja, J. Rocha, M. Naik, and A. Demos. *Restoration and pore sealing of low-k films by UV-assisted processes*. in *Interconnect Technology Conference / Advanced Metallization Conference (IITC/AMC), 2014 IEEE International*. 2014.

Appendix 1: SIMS theory

Basic equations governing the secondary ion generation for SIMS technology are explored.

The intensity of secondary ions (SI) detected during a SIMS analysis is the result of multiple factors:

$$I_m = I_p \cdot Y_m \cdot \alpha_m^{+/-} \cdot \theta_m \cdot \eta$$

I_m corresponds to the secondary ion current of a given specie m, while I_p is the primary ion density and Y_m is the sputter yield of species m sputtered. $\alpha_m^{+/-}$ is the probability to ionise the specie and θ_m correspond to its concentration in sample surface. η is the transmission rate of instrument plus detector. η value is fix around 90/95% and it is characteristic of the instrument, contrary I_p can be changed depending on analysis conditions. Parameters like Y_m and $\alpha_m^{+/-}$ are often low and can be subjected to important modifications.

The sputtering yield can deeply influence the secondary ion current and it is defined as the number of species N_m sputtered for each impacting ion N_p:

$$Y_m = \frac{N_m}{N_p}$$

Sputtering is a rather damaging process. Consequently, it is harder to measure sputter rates for covalent organic material. If the material is a molecule, every molecule impacted will be effectively destroyed. In this case is then more reasonable to speak in terms of damaged cross-section σ. In this case, the loss of structurally significant species in a ToF-SIMS spectrum is function of the bombardment time considered as a measure of increasing damage. The damage cross-section is related to the SI current of the specie m by this formula:

$$I_m = I_{m0} e^{(-\sigma I_p)}$$

I_{m0} corresponds to the initial SI current of m specie.

Appendix 2: FT-IR measurements

In addition to the quantification by ToF-SIMS of copolymer deposited by i-CVD, a complementary study was conducted using FTIR involving the same sample set.

At first FTIR spectra of poly(neopentyl methacrylate) and poly(ethylhexyl methacrylate) and p(ehMa)/p(npMa) are compared as shown in Appendix FT-IR - 1-a. At a first sight, they appear very similar. In the table, Appendix FT-IR - 2, a recognition of chemical bonds is performed to inspect the presence of peaks able to discriminate the two polymers. Peak at 1380 cm^{-1} is characteristic of the $-CH_3$ asymmetric bending, this peak has a doublet shifted of 20 cm^{-1} when another methyl is bounded to a common carbon atom (1360 cm^{-1} peak).

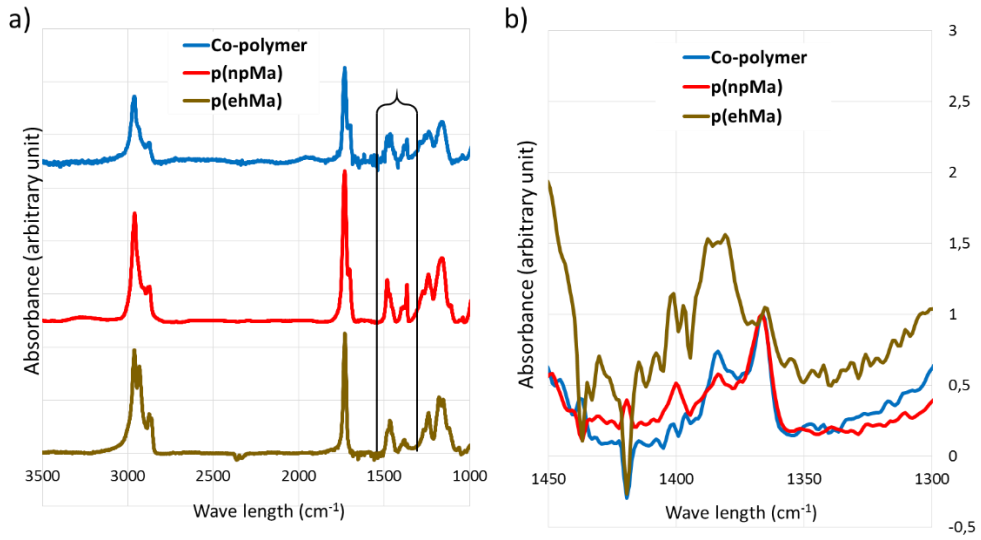

Appendix FT-IR - 1: FTIR spectra. The blue line corresponds to the FITR spectrum of the copolymers. Red and orange curve represent respectively the poly(neopentyl methacrylate) and poly(ethylhexyl methacrylate) curves. a) The zone delimited by solid lines contains peaks that most change between samples. b) Zoom of the area between 1450 and 1300cm^{-1} where a normalisation on the peak at 1360cm^{-1} is performed.

Looking attentively at the three spectra in Appendix FT-IR - 1-b the presence of peaks at 1360 and 1380 cm^{-1} is observed. Normalising by the intensity of the peak at 1360 cm^{-1} the co-polymer spectrum appear to have a behaviour in between the two polymers. Its spectrum is identical to the one of a p(npMa) with an accentuated presence of $-CH_3$ groups characteristic of a p(ehMa) polymer. Assuming that the relation between

co-polymer ratios is linearly proportional to the peak areas, it is then possible to compare the co-polymer peak areas with the ones of pure polymers. Quantitative information can be then obtained defining repeating unit ratios in copolymers by the application of the mixing rule for composite materials.

Appendix FT-IR - 2: Characteristic peaks of poly(neopentyl methacrylate) on the left and peaks of poly(ethylhexyl methacrylate) on the right. Peaks at 1380 and 1360 cm^{-1} correspond to the vibration bending modes of $-CH_3$ group in methyl and dimethyl respectively, the ratio between these two peaks is found to change depending on the co-polymer samples.

Poly(neopentyl methacrylate)		**Poly(ethylhexyl methacrylate)**	
Wavelength (cm^{-1})	*Bounds*	*Wavelength* (cm^{-1})	*Bounds*
2958/2877	$-CH_3$ stretch	2958/2877	$-CH_3$ stretch
2930/2858	$-CH_2$ stretch	2930/2858	$-CH_2$ stretch
1730	$-C=O$ carbonyl	1730	$-C=O$ carbonyl
1464	$-CH_2$ bending	1464	$-CH_2$ bending
1360	$(-CH_3)_2$ bending	1380	$-CH_3$ bending
1300-1100	$-CO-O$ ester	1300-1100	$-CO-O$ ester

Characteristic peak areas of each sample are normalised by the film thickness and listed in Appendix FT-IR - 3. X is assumed as the quantity of p(npMa) in the copolymer and $1-X$ the p(ehMa). If X is equal to zero, the ratio r between $p(ehMa)/p(npMa)$ is equal to 3.636. In the case of $x=1$, r correspond to 0.515.

The proportion is established between the sample 100% p(npMa) and the analysed copolymer by the following equation. Knowing the copolymer ratio ($r_{co-polymer}$) it is then possible to calculate the quantity of p(npMa) in the co-polymer.

$$\frac{(X)_{100\%\,p(npMa)}}{(r_{p(npMa)}-r_{p(ehMa)})}=\frac{(X)_{co-polymer}}{(r_{co-polymer}-r_{p(ehMa)})}$$

$$(X)_{co-polymer}=\frac{(r_{co-polymer}-r_{p(ehMa)})}{(r_{p(npMa)}-r_{p(ehMa)})}=\frac{(r_{co-polymer}-3.636)}{(0.515-3.636)}$$

The obtained results in Appendix FT-IR - 3 show a significant presence of poly(neopentyl methacrylate).

Appendix FT-IR - 3: Areas of peaks at 1380 and 1360 cm^{-1} for 100% p(ehMa) and p(npMa) and for the deposited co-polymers. The ratio value is obtained dividing the area at 1380 by the area at 1360.X values are obtained by using the equation containing

	p(ehMa)	***p(npMa)***	***Co-po1***	***Co-po2***
$\mathbf{1380}cm^{-1}$	0.040	0.035	0.045	0.044
$\mathbf{1360}cm^{-1}$	0.011	0.068	0.055	0.047
$Ratio\ (r)$	3.636	0.515	0.818	0.936
x	0	1	0.90	0.87

Abstract

Nowadays, the micro and nanotechnology field integrates a wide range of materials that can be defined as "fragile" because of their shape, dimension or density. In this work, three materials of this kind, at different level of technological and industrial maturity are studied by time of flight secondary ion mass spectrometry (ToF-SIMS). These materials are: mesoporous silicon, thin polymethacrylate films deposited by initiated Chemical Vapour Deposition (i-CVD) and hybrid organosilicate (SiOCH) dielectric materials (low-*k*). The objective is to verify and validate the ToF-SIMS as a reliable characterisation technique for describing the chemical properties of these materials. Indeed, because of this intrinsic "fragility", the consistency of the chemical information is connected to an appropriate interpretation of the specific ion/matter interactions taking place.

For mesoporous silicon, a systematic analysis is carried out considering various sputtering ion sources (Caesium, Xenon and Oxygen); both sputtering and ionisation behaviours are examined relatively to the nonporous silicon, taking into account energy of the sputtering beam and porosity rate of the target material.

Concerning nanometric thick polymer films, low damaging analysis conditions are applied by the use of argon cluster primary ion sources in order to obtain a significant molecular secondary ion information. In these conditions, a discrimination of quasi-identical nanometre thick structures is made possible and a quantification method for copolymers is then proposed. In addition, with the supplement of data principal component analysis (PCA) an innovative and significant correlation is obtained between main Principal Component and sample molecular weights.

Finally, the effect of several industrial integration processes (such as etching or wet cleaning) applied on low-*k* materials are studied in order to understand their detrimental impact on low-*k* insulating properties. To achieve a depth-resolved chemical information, low energy caesium sputtering is shown to be the most adapted and sensitive strategy. In addition, PCA is shown to be almost essential to amplify differences between samples significantly. This approach allowed combining the variation of physical properties (dielectric constant) with the chemical ones.

Keywords: nanotechnology, fragile materials, ToF-SIMS, principal component analysis, porous silicon, iCVD polymers, SiOCH low-k

Résumé:

Aujourd'hui, une grande variété de matériaux dit « fragiles » sont intégrés dans des dispositifs micro ou nanotechnologiques. Ces matériaux sont définissables comme « fragiles » en raison de leur forme, de leur dimension ou encore de leur densité. Dans ce travail, trois catégories de matériaux, de différents niveaux de maturités industrielle et technologique, ont été étudiés par spectrométrie de masse des ions secondaires à temps du vol (ToF-SIMS). Ces matériaux sont: du silicium méso-poreux, des polyméthacrylates déposés en couches très minces par voie chimique en phase vapeur initiée (iCVD) et des matériaux organosilicates (SiOCH) à basse constante diélectrique (low-*k*). L'objectif de ce travail est de vérifier et de valider la méthode ToF-SIMS comme une technique fiable pour répondre aux besoins de caractérisation chimique rencontrés pas ces matériaux. Il s'agit également d'établir la cohérence de l'information chimique produite par l'interprétation de l'interaction ion/matière se déroulant lors de l'analyse. Pour le silicium méso-poreux, les échantillons ont été pulvérisés par différentes sources primaires d'ions (Césium, Xénon, Oxygène) et l'information secondaire générée comme, par exemple, les différences d'ionisation entre la couche poreuse et le matériau dense ont été analysées, notamment vis de l'énergie du faisceau de pulvérisation mais aussi du taux de porosité du matériau cible. Des modifications morphologiques significativement différentes selon la source d'ions ont également été observées et ont été corrélées à différents types de régime de pulvérisation, principalement induites par le taux de porosité de la cible.

Concernant la caractérisation de polymères en couches minces, des conditions d'abrasion très peu agressives, notamment l'usage d'ions d'argon en cluster polyatomiques, ont été appliquées avec l'intention d'obtenir une information chimique secondaire riche en hautes masses moléculaires. La discrimination de films de polyméthacrylate avec une structure chimique quasi-identique a pu être obtenue et un protocole de quantification de copolymères proposé. De plus, par l'utilisation de la méthode d'analyse de données en composantes principales (PCA) appliquée aux spectres, une corrélation claire a été établie entre les composantes principales et la masse moléculaire des films de polymères.

Enfin l'impact de traitements d'intégration tels que de la gravure ou du nettoyage chimique, nécessaires à la mise en œuvre industrielle des matériaux low-*k*, mais défavorables à leurs propriétés diélectriques, a été étudié. Pour obtenir une information chimique résolue en profondeur, l'abrasion par césium à basse énergie a été identifiée comme la stratégie la plus sensible et la plus adaptée. De même, la PCA a permis d'amplifier significativement les différences chimiques entre échantillons, permettant de rapprocher les variations de constante diélectrique aux compositions chimiques.

Mots clés: nanotechnologies, matériaux fragiles, ToF-SIMS, analyse en composantes principales, silicium poreux, polymères iCVD, SiOCH matériaux à basse constante diélectrique